CZECH TECHNICAL UNIVERSITY IN PRAGUE
Faculty of Civil Engineering

Ph.D. Programme: Civil Engineering
Branch of study: Building and Structural Engineering

Ing. Soňa Valentová

Modeling of carbon and basalt plain weave textile composites

Modelování textilních kompozitů s uhlíkovou a čedičovou plátnovou výztuží

DOCTORAL THESIS

Supervisor: prof. Ing. Michal Šejnoha, Ph.D., DSc.

Specialist supervisor: doc. Ing. Jan Vorel, Ph.D.

April, 2022

ACKNOWLEDGMENTS

I express my deep gratitude and thanks to my advisor prof. Ing. Michal Šejnoha, Ph.D., DSc. for his patience, professional advice, and continuous encouragement throughout my research. I thank, also, doc. Ing. Jan Vorel, Ph.D. for his interest and valuable suggestions. In addition, I thank Ing. Tomáš Koudelka, Ph.D. who instructed me in numerical implementation of various parts of the selected constitutive models. I extend my deep appreciation to Ing. Blanka Tomková, Ph.D., Ing Jana Novotná, Ph.D., doc. Ing. Pavel Padevět, Ph.D. and Ing. Radek Sedláček for their assistance with preparation and execution of the experimental part of my research.

Most importantly, I wish to thank my family for their endless encouragement. They have been a constant source of love and support.

Financial support for this thesis was provided by the Czech Technical University in Prague within SGS project registered under the No. SGS21/037/OHK1/1T/11 and by the GAČR grant No. 21-28525S.

TABLE OF CONTENTS

LIST OF FIGURES

LIST OF TABLES

Czech Technical University in Prague

Abstract

Modeling of carbon and basalt plain weave textile composites

Soňa Valentová

Owing to its high strength, stiffness, and thermal or chemical resistance, polymer matrix based composite materials play an important role in many engineering areas. Depending on the type of reinforcements and bonding material their applications range from aircraft and car industry to high-tech sport equipment. Many applications can be found also in civil engineering including wind turbines or pedestrian bridges. In every case, a reliable performance calls for reliable predictive models. Such models should be capable of properly reflecting the influence of geometrical details of reinforcements as well as the time and nonlinear response of individual constituents when loading these materials beyond the elastic limits. The degree of complexity increases when moving from traditional laminate structures made of unidirectional fibrous plies to woven composites, e.g. plain weave reinforced laminates. This inevitably suggests solution strategies based on multiscale or hierarchical modeling. Because of high computational demands, the application of classical micromechanical models in combination with finite element method offers a suitable method of attack. This concept is examined in this work with particular attention devoted to plain weave reinforced composites made either of carbon or basalt fabrics bonded to a polymer matrix. To appreciate a wide range of applications, the behavior of a high performance "aero" epoxy resin L285 Havel is compared to ordinary epoxy matrices.

To this end, a thorough experimental program is performed first on individual polymer matrices to address their rheological behavior. Because of their dependence on the rate of loading, the generalized Leonov model is adopted to describe their behavior numerically. The developed calibration procedure exploiting the rate dependent tensile tests and standard creep experiments is verified by comparing the laboratory measurements with numerical predictions. The results identify the limitations of the selected model to properly capture the response of ordinary epoxy matrices in particular.

A series of numerical tests is then performed, first at the level of a yarn, and next at the

level of a textile ply. The former set of computational analyses aimed at addressing the ability of the Mori-Tanaka (MT) averaging scheme to accurately describe the nonlinear viscoelastic response of unidirectional fibrous composites by a direct comparison with the simulations carried out with the help of finite element method. These simulations are performed in the framework of first-order homogenization employing a periodic hexagonal array (PHA) model as a suitable representative of a random microstructure. The need for reformulation of the original format of the MT method was observed leading to a revision of the constitutive model of the fiber phase which allowed for matching the predictions of the two approaches for specific loading conditions quite well. However, running computational experiments on a large class of representative elements extracted directly from the yarn microstructure opened an issue of a reliability of the PHA model and potentially promoted a proper representation of random microstructure in terms of a statistically equivalent periodic unit cell.

Efficiency of the MT method was then exploited in the formulation of a coupled two scale computational scheme. While at the level of textile ply the finite element computational homogenization is assumed, the MT method is used at the level of yarn to serve as a stress updater in place of another finite element model representing the yarn microstructure as typical of FE^2 based multiscale approach. However, at this stage of research the implementation is neither verified nor validated due to absence of both the results from, e.g., FE^2 computational scheme and experimental measurements.

Depending on the loading rate, a transition between the viscoelastic and brittle response occurs in the polymer matrix, opening the door to damage modeling of brittle or quasi-brittle materials or a combination of damage model with viscoelasticity. This, however, goes beyond the present scope. Therefore, attention is limited to the modeling of damage in plain weave textile composites in the absence of time effects. Unlike the previous approach, the analysis at the level of yarn is assumed independent of the level of textile ply and serves only to obtain the homogenized strengths and fracture energies driving the response of the homogenized yarn. These parameters are derived again using the PHA model. The standard purely strain-based formulation is compared to so called mixed type loading conditions allowing us to load the composite by components of both the mesoscopic uniform strains and stresses thus to properly address the uniaxial state of stress. Although for the PHA model the resulting mesoscopic strengths and fracture energies do not depend much on the type of

loading, the mixed loading conditions are preferred. As this is work in progress, no results derived at the textile ply level are currently available. Nevertheless, a suitable orthotropic damage model has already been implemented into SIFEL finite element code and is being currently tested.

České vysoké učení technické v Praze

Abstrakt

Modelování textilních kompozitů s uhlíkovou a čedičovou plátnovou výztuží

Soňa Valentová

Kompozitní materiály s polymerní matricí dnes hrají důležitou roli v mnoha inženýrských oblastech. To je dáno zejména jejich vysokou pevností, tuhostí, chemickou odolností a odolností vůči vysokým teplotám. V závislosti na typu použité výztuže a pojiva se oblast jejich využití pohybuje od leteckého a automobilového průmyslu, až po technologicky vyspělé sportovní vybavení. Mnoho aplikací se objevuje i ve stavebním inženýrství. Za zmínku zcela jistě stojí větrné turbíny nebo lávky pro pěší. V každém případě efektivní a spolehlivé fungování kompozitních materiálů vyžaduje použití spolehlivých prediktivních modelů, a to bez ohledu na konkrétní typ materiálu a konkrétní oblast použití. V případě materiálů zkoumaných v předložené práci je důležité, aby tyto modely dokázaly postihnout vliv geometrie výztuže a zároveň reflektovat časově závislou nelineární odezvu jednotlivých komponentů během zatěžování při překročení limitu pružné odezvy. Je zřejmé, že stupeň obtížnosti numerických predikcí vzrůstá s přechodem od tradičních laminátových konstrukcí z jednosměrných vláknových kompozitů k systémům vyrobeným z tkaných, vícesměrných textilií. Studium těchto materiálů se pak často neobejde bez víceúrovňového, nebo také hierarchického modelování. Kombinace klasického mikromechanického modelu a metody konečných prvků nabízí v tomto případě efektivní řešení. Tento přístup je předmětem zkoumání předložené disertační práce. Zvláštní pozornost je věnována textilním kompozitům s uhlíkovou a čedičovou plátnovou výztuží vloženou do polymerní matrice. Vzhledem k širokému rozsahu využití je primárně sledováno chování „letecké“ epoxidové pryskyřice L285 Havel, které je porovnáno s chováním běžných epoxidových matric.

Ke zjištění reologického chování jednotlivých polymerních matric je nejdříve provedeno důkladné experimentální měření. Vzhledem k jejich charakteristické závislosti na rychlosti zatěžování je k numerickému popisu odezvy použit zobecněný Leonovův model. Vyvinutý kalibrační přístup využívající tahové zkoušky závislé na rychlosti zatěžování a standardní zkoušky dotvarování, je ověřen porovnáním experimentů s numerickými simulacemi. Při

podrobném popisu odezvy jsou z výsledků patrné limity dané metody, zejména u běžných epoxidových pryskyřic.

Následně je provedena série numerických testů. Nejdříve na úrovni vlákenného svazku, poté na úrovni textilní vrstvy. Úvodní simulace na úrovni vlákenného svazku měly za cíl posoudit schopnost průměrovací metody Mori-Tanaka (MT) popsat nelineární viskoelastickou odezvu kompozitů s vláknovou výztuží dostatečně přesně v porovnání s výsledky získanými metodou konečných prvků (MKP). Simulace MKP jsou provedeny s využitím periodické hexagonální buňky (PHA) reprezentující náhodné uspořádání mikrostruktury. Příslušná formulace vychází z teorie homogenizace prvního řádu. Výsledky prokázaly nedostatky základní varianty metody MT, a tudíž nutnost její reformulace, např. modifikací konstitutivního modelu vláken. To zajistilo velmi dobrou shodu výsledků obou přístupů pro definované podmínky zatížení. Zároveň s tím provedené simulace MKP na relativně velkém počtu různě velkých reprezentativních vzorků extrahovaných přímo z mikrostruktury svazku však otevírají otázku spolehlivosti PHA modelu a s tím spojenou reprezentaci náhodné mikrostruktury pomocí statisticky ekvivalentní periodické buňky.

Výpočetní efektivita metody MT byla poté využita při formulaci sdruženého, dvouúrovňového výpočetního schématu. Zatímco na úrovni textilní vrstvy se předpokládá konečně-prvková homogenizace, aktualizace napětí na úrovni vlákenného svazku je řízena metodou Mori-Tanaka. Na této úrovni tak metoda MT nahrazuje další konečně-prvkový model, jako je tomu např. v případě víceúrovňové FE^2 metody. Absence výsledků, a to jak numerických, např. z FE^2 analýzy, tak i experimentálních, však v současnosti neumožňuje implementaci modelu ověřit.

V závislosti na rychlosti zatížení se u polymerní matrice vyskytuje přechod mezi viskoelastickou a křehkou odezvou, což otevírá téma modelování poškození křehkého, či kvazikřehkého materiálu, případně kombinaci modelu poškození a viskoelasticity. To však již přesahuje rámec předložené práce. Zde je pozornost zaměřena pouze na modelování poškození textilních kompozitů s plátnovou výztuží bez uvažování času. Na rozdíl od předešlého přístupu se předpokládá, že analýza na úrovni vlákenného svazku není ovlivněna chováním na úrovni textilní vrstvy a naopak. Simulace na úrovni vlákenného svazku, reprezentovaného opět PHA modelem, však slouží k určení efektivních pevností a lomových energií, které následně vstupují do konstitutivního modelu homogenního svazku na úrovni textile. Pro

odvození těchto veličin jsou sledovány dva přístupy. Standardní formulace předpokládající předepsání pouze složek deformace je porovnána s tak zvanými smíšenými podmínkami zatížení, které umožňují zatížit kompozit kombinací složek vektoru deformace a napětí, a tím zajistit jdnoosý stav napjatosti. Ačkoliv výsledné pevnosti a lomové energie určené analýzou PHA modelu neprokazují výraznou závislost na typu zatížení, jsou smíšené podmínky zatěžování upřednostněny. Výsledky simulací na úrovni textilní vrstvy však nejsou zatím k dispozici. Nicméně vhodný ortotropní model poškození byl již implementován do konečněprvkového kódu SIFEL a v současné době probíhá jeho testování.

Chapter 1

INTRODUCTION

Contemporary world is focused on materials enabling to fulfill the requirements of the 21st century. Ever increasing special demands on structural components employ researchers in material engineering all over the world in search for material systems with exceptional properties. In particular, their mechanical and physical properties must be continuously improved to compete with the related technological progress. This also includes economical as well as ecological aspects, which does not often go hand in hand so it is difficult to find a suitable compromise.

Textile composites appear as a suitable candidate to meet these requirements in a variety of engineering areas. This is supported by genuine advantages of composites, e.g., prefabrication employing advanced manufacturing processes and technologies to produce material systems with tailored mechanical and physical properties. An appropriate choice of individual components allows for creating products with entirely unique characteristics. Carbon fibers in various forms of reinforcement embedded in a polymer matrix are widely spread out in constructions and products in many different branches such as aviation, shipbuilding, space industry, automotive engineering, sport equipment etc. However, the final product is generally financially demanding, which impels both manufactures and researches to seek for other less expensive solutions.

A good example is a wind turbine blade. The easiest way to improve mechanical properties is to increase the volume fraction of reinforcements. With carbon fibers this approach might be a financially unacceptable solution not mentioning a considerable increase in weight of the turbine. In this regard, the basalt fibers seem to offer a promising alternative in some applications owing to their acceptable mechanical and physical properties, while considerably reducing the price of a particular product. Modifying the mechanical properties of the matrix by adding inorganic fillers from recycled materials (Novotná, 2021) may considerably improve the weight to stiffness ratio eventually leading to economically admissible designs with sufficient bearing capacity. Exploiting green matrices would then allow us to design products which also meet the ecological requirements. On the contrary, this calls for a considerable activity in both experimental and computational research as finding

an optimal material composition is not an easy task (Tomková et al., 2018).

To partially contribute to this task is also the thesis objective. While potential of composite materials is almost endless, we address only a small area of textile reinforcements concentrating on the comparison of mechanical response of carbon and basalt fibers combined with several types of untreated epoxy based polymer matrices. A brief exposition of their potential application given next supports this research venture.

1.1 Textile reinforcement

The role of a reinforcement is to bear the main load and to ensure the strength and stiffness. The type of reinforcement considerably influences the final properties of the product. Currently, various forms of reinforcements are used for composites spreading from chopped fibers randomly dispelled in the matrix, long fibers arranged uniaxially along one particular direction, to fibers regularized to a relatively difficult planar or spatial structure reinforcing the composite in several directions.

Plain weave textile composites, where fibers are located in two perpendicular directions, see Fig. 1.1, guarantee high stiffness, strength and durability (Molnár, 2017) together with relatively simple manipulation when large scale composite products (outboard flaps, wing stubs, spoilers, engine cowls, etc.) are prepared (Long, 2005).

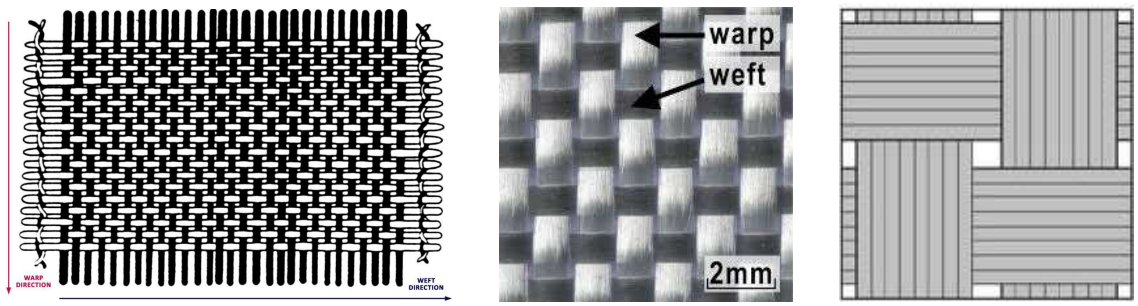

(a) (b) (c)

Figure 1.1: a) Two-dimensional woven fabric (plain weave) (Long, 2005; Cherif, 2016), b) Example of plain weave reinforcement (Strugala et al., 2018), c) Example of balanced plain weave textile unit cell (Kunc, 2013)

A notable group of structural composites are reinforced by various types of a woven fabric. The most common types of woven reinforcements are made from glass and carbon fiber tows (roving fabrics) Fig. 1.1. The principal advantage of carbon fibers is a very high stiffness. On other pole are their high price, fragility, and susceptibility to cause carcinogenic inflammation. Thus their properties are often compared to other materials. In terms of price and production, the basalt fibers appear most favorable which attributes to their increasing application in practice with the attempt to substitute carbon fibers where possible.

Although relatively simple, the final product may suffer from various types of imperfections caused by manufacturing processed. While an attempt is made to include these imperfections into numerical simulations (Vorel et al., 2013, 2015), the computational models often make no distinction between the warp and weft directions leading balanced composites as seen in Fig. 1.1(c). This simplification is also adopted in the course of this thesis.

1.2 Carbon fibers

Carbon fibers are considered as an advanced type of material with superb properties for many applications. As a technical material, they have been known for many years and they have been gradually developed to gain improved specific properties. According to (Grégr, 2004), industrial production of carbon fibers from viscose started in 1950s. Production of fibers made from polyacrylonitrile (PAN) and isotropic pitch-based carbon fibers dates back to 1960s. At present, carbon fibers are typically produced from polyacrylonitrile, a fossil-based polymer, where the polymer is first wet spun into a precursor fiber before being turned into a carbon fiber. Transformation to the carbon fiber is then carry out in a series of steps including thermosetting in an oxidizing environment, carbonization in an inert environment, and finally surface treatment (Das, 2011).

Carbon fibers based on polyacrylonitrile raw material have a diameter (for non-circular fibers equivalent diameter) about 7 μm. New generation of carbon fibers with higher utility parameters have a smaller diameter of 4 - 6 μm. The pitch-based carbon fibers have usually diameter greater than 10 μm and polyacetylene carbon fibers have a diameter of about 25 μm (Grégr, 2004).

According to (Hudec, 2013), carbon fibers can be divided into two basic groups, high strength and high modulus fibers. High strength fibers are manufactured during the tem-

perature between 900 and 1500°C and are very stiff. High modulus fibers are produced at temperatures in the range from 2000 to 2800°C and they are characterized by high modulus of elasticity. Slightly more detailed classification in terms of final mechanical properties offers (Huang, 2009), where carbon fibers are divided into ultra high modulus (>500 GPa), high modulus (>300 GPa), intermediate modulus (>200 GPa), low modulus (<200 GPa), and high strength (>4 GPa) carbon fibers.

However, stiffness and strength are not the only material properties which have been supporting their popularity over decades. Chemical inertness is also worth mentioning (Chand, 2000). Unlike glass or other organic polymer fibers, they do not suffer from stress corrosion or stress rupture failures at room temperatures. Their strength and modulus of elasticity at high temperatures also surpass other materials. Fatigue resistance, vibration attenuation, low specific weight, low coefficient of friction and no plastic deformation under loading, low coefficient of thermal expansion, wide range of coefficient of thermal conductivity, thermal shock resistance, and resistance to extremely high and low temperatures have also been documented. For specific values of a variety of carbon fibers the interested reader is referred to (Peijs et al., 2022; Frank et al., 2014).

On the other hand, compressive strength is lower when compared to inorganic fibers (Minus and Kumar, 2005). Carbon fibers also suffer from brittleness (the elongation after crack is smaller than that of glass fibers, therefore the minimum radius in bending is greater) and low electrical resistance in both longitudinal and transverse direction (Kořínek, 2022).

1.2.1 Application of carbon fibers in practice

As a reinforcement in composites, carbon fibers appear in almost all areas of human activity. Nevertheless, still a relatively high price directs their application towards high-tech products where this handicap does not play such an important role.

Long carbon fibers are mainly used as unidirectional or textile reinforcement in composite materials such as carbon fiber reinforced plastics or carbon-carbon composites. Short type of carbon fibers is used as a diffused reinforcement for example in concrete or cement. Especially they fit for applications, where strength, stiffness, low weight and excellent fatigue characteristics are critical requirements.

The main use of carbon fibers can be divided into two groups. The first group includes

high technology sector such as aircraft, aerospace and nuclear engineering. The second one combines general engineering and transportation sector including automobile bodies and engineering components production, such as bearings, gears, cams, fan blades, etc., taking a particular advantage of outstanding strength and stiffness properties (Chand, 2000). For applications exploiting their thermal and chemical resistance see, e.g., (Dhand et al., 2015). Recently, owing to their biocompatibility, a new area of their applications in biomaterials has emerged (Petersen, 2016; Saito et al., 2011; Chua et al., 2021).

1.3 Basalt fibers

Basalt fibers can be classified as a novel type of silicate fibers. They find many industrial applications. Moscow Research Institute of Glass and Plastic is known for the initiation of research activities leading to the development of basalt fibers in 1953-54 (Morova, 2013).

Properties of basalt fibers are very similar to the glass fibers type S (S-glass) and in general overcome the properties of the glass fibers type E (E-glass) being predominant from the production of glass fibers point of view. In most cases, E-glass fibers can be replaced by basalt fibers, especially in cases where resistance in the extreme conditions is required. Basalt fibers have the strength level close to E-fibers and improved elasticity modulus typical of high-modulus and high-strength magnesium aluminosilicate S-fibers, see (Dalinkevich et al., 2009) for further details. It is suggested in that they are more stable in a strong alkali environment, but less stable in a strong acid environment compared to glass fibers.

Chemical durability of basalt fibers was first examined by Ramachandran et al., see (Ramachandran et al., 1981), where much better resistance to alkaline attack and worse in acidic environment compared to the glass fibers was shown. Similar conclusion was presented in (Deàk and Czigány, 2009). The only glass fiber as good as basalt fiber in alkali medium is AR-glass fiber, but its price is several-times higher. Better mechanical properties of basalt fibers after corrosion treatments in comparison to glass fibers were proposed in (Nasir et al., 2012).

Further advantages of basalt fibers are inflammability, good insulating, thermal, electrical and sound properties, low water absorption, and low coefficient of thermal expansion. They are biologically inactive and from the ecological point of view their production and liquidation is environmentally friendly, see, e.g., (Donnet and Bansal, 1998; Deàk and Czigány,

2009; Sim et al., 2005; Pohánková, 2010). When further compared to glass fibers, basalt fibers are non-combustible and do not split into finely disperse (less than 0.4 μm) microfiber structures with carcinogenic properties under high contact stresses in high-temperature conditions (Artemenko, 2003; Czigány et al., 2005). Basalt is absolutely inert, refractory and explosion resistant. Raw material for basalt fibers is one of the cheapest and requested because of its availability and good properties in general. Thanks to the technological progress, the production costs of basalt fibers are comparable to glass fibers and are significantly lower than those of carbon fibers. Therefore, basalt fibers could be justly considered as optimal with respect to price and quality.

Cross-section of basalt fibers is almost circular and the surface is smooth. According to (Hu and Liu, 2010), the basalt fibers have typically a filament diameter between 9 and 13 μm, which is far above the respiratory limit of 5 μm to make basalt fibers a suitable replacement also for asbestos.

As mentioned, e.g., in (Sim et al., 2005; Fiore et al., 2015), basalt fibers can be used over a wide range of temperature, from -200 to +600-800°C, depending on the chemical composition of the raw material. Higher temperatures cause structural changes of the material. Hao and Yu introduced a thermal gravimetric analysis of glass and basalt fibers. The results presented in (Hao and Yu, 2010) register the mass loss occurring with temperature exceeding about 200°C. Their investigation affirmed good thermal stability of basalt fibers.

Continuous basalt fibers are produced in rovings. With differences in chemical composition of basalt fibers depending on the occurrence of raw basalt, their mechanical and chemical properties may slightly vary. According to (Dalinkevich et al., 2009) it has been sufficiently reliably proved that the effect of chemical composition on the final mechanical properties is negligible in comparison with molding conditions, more specifically drawing temperature, period of melt homogenization, and the fiber diameter. As the diameter of long-length and continuous fibers is bigger (ranges from 7 to 10 μm) than the filament diameter (1-4 μm), the strength has a wide range (lower strength for lower diameter), so the manufacturing procedures influence the final properties. The mechanical strength of basalt fibers is thought to be closely related to the presence of surface heterogeneities, such as surface flaws, structure defects and impurities (Lund and Yue, 2008). Slight disadvantage of basalt fibers is their brittleness, so this material must be carefully handled.

Basalt fibers as reinforcing material of composites with polymer matrices, such as epoxy, polyester and vinyl ester resins, have recently been exploited in the production of composites. Mechanical properties of such a composite are similar to the properties of composites reinforced with S-glass fibers and appear better than those with E-glass fiber reinforcement. Experimental results presented in (Lopresto et al., 2011) showed basalt reinforced epoxy composites as a material with the higher tensile, flexural and compressive Young modulus in comparison to the composite with E-glass fiber reinforcement. The same has been observed also for compressive and bending strength, impact force and energy. Owing to better bonding between basalt fibers and epoxy resin and high interlaminar shear strength they seem to be a good option in many applications (Lopresto et al., 2011; Chairman and Kumaresh Babu, 2013). Therein, a higher stiffness in tension, flexure and compression has also been proposed for laminates. With respect to fatigue behavior, Dorigato and Pegoretti in (Dorigato and Pegoretti, 2012) marked the basalt fiber based laminate as a structural element with a high capability of sustaining progressive damaging. The tensile strength was found again higher than that of the glass fiber based laminate and comparable to that of laminates reinforced with carbon fibers. When discussing the properties of basalt fiber based composites the curing temperature is worth mentioning as this may have a great impact on the composite mechanical response (Černý et al., 2007; Černý et al., 2009).

1.3.1 Application of basalt fibers in practice

The idea of using basalt fibers as a reinforcement of composite materials first emerged in the former Soviet Union in an aerospace research program (Deàk and Czigány, 2009).

A big potential of basalt fibers is in thermal insulation and passive fire protection applications thanks to the presence of a large amount of micro-pores preventing convection and thermal radiation of the air, (Hao and Yu, 2010, 2011).

The manufacturing process is similar to that of glass or carbon fibers but consumed energy is lower, which leads to lower production price. Should be mentioned that manufacturers offer basalt continuous rovings and fabric that are nearly 30 % stronger, 15-20 % stiffer and 8-10 % lighter than the E-glass fibers competing with carbon fibers in several applications. Wind power blades in energy industry (Fiore et al., 2015) is one particular example.

In the building industry, basalt fibers find place for example as geotextiles, reinforce-

ment fabrics, refractory construction materials, fillers for sealants, thermal insulation compound, reinforcements in many conventional composite constructions, thermal insulation boards suitable for pitched roofs, ceilings, walls, facades and floors. The field of electrical applications is also vast where basalt fibers are used as a resistant insulation for electric cables and underground piping. Products can also be used for technical insulation suitable for boilers, for ventilation equipment, chimneys, exhausts and other heating equipment where sound and thermal insulation is required. They can be applied also in the automotive industry, can perfectly substitute asbestos ones, and next can be applied for various components for aircraft, ships, etc. In (de la Rosa García et al., 2013) they were shown as an advantageous bending reinforcement for pine timber beams. They can also be used instead of composites with carbon reinforcement to improve earthquake-resistant properties in existing buildings, see (Fiore et al., 2015).

Basalt fibers have low ductility and therefore they are used as a filler for the production of high-strength, heat-resistant Hi-Tech lines and nets. They are also widespread in the production of sport equipment. In particular, they are successfully utilized for water skies, car and motorcycle outer parts, bicycles, kayaks, canoes and paddles, sky poles, skies and snowboards, tennis rackets, etc.

1.4 Matrix

The matrix is a fundamental component of the final composite. In general, it is continuous, tough and plastic. Its main task is the connection of the reinforcement allowing the transfer of load between individual fibers, ensuring their correct placement, shape, and stability. Additionally, it protects the reinforcing material against external effects. The matrix is the main indicator of corrosion, temperature, and fire and chemical resistance.

The most common matrix material used in the production of composites is the epoxy resin for its specific properties, such as temperature resistance, hydrophobic properties, UV, oxidation by atmospheric oxygen, and ozone (high windiness) resistance. Also, it is inert with respect to other materials, biologically inert, non corrosive and has good electric-insulating properties, see (Veselý and Bezkočka, 2008). Because of that, it can also be applied as a temperature resistant coating material.

The market offers a relatively large variety of epoxy resins to serve as matrices in the

production of composite materials. Among others the L285 epoxy resin has recently been the subject of research aimed at potential improvement of its properties by adding a suitable filler (Novotná, 2021).

With reference to a technical sheet listed in the appendix, extremely good physiological compatibility and mechanical properties of L285 mixed with H500 hardener can be expected. This epoxy resin is designed for curing at room temperature and for combination with glass, carbon and aramid fiber reinforcement. The process of lamination is characterized by a very short curing time, even at low temperatures (good curing is ensured at temperatures starting at +10°C). The optimum processing temperature ranges between 20 and 25°C. Higher processing temperatures are possible, but shorten the pot life. Water (for example, very high humidity or water contained in fillers) can accelerate the resin / hardener reaction. Different temperatures and humidity during processing do not have a significant effect on the strength of the cured product. Even under unfavorable curing conditions, such as low temperature or high relative moisture, non-stick surfaces with high gloss can be achieved.

In the Czech market the 455 and 520 epoxy resins Spolchemie mixed with 492 hardener are also commonly used, see the available technical sheets listed again in the appendix.

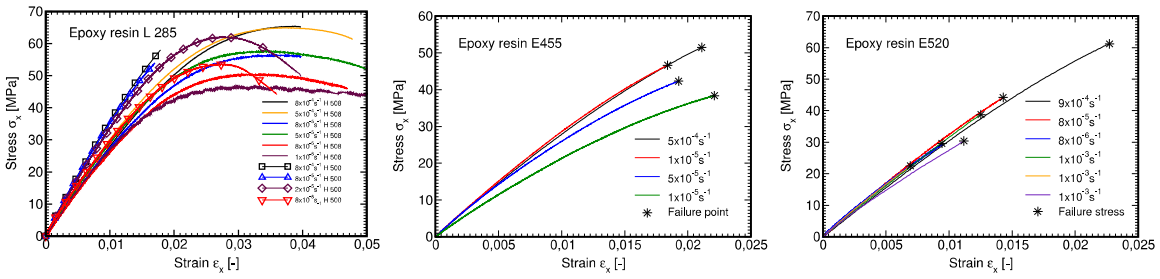

(a) (b) (c)

Figure 1.2: a) L285 Havel, b) E455, c) E520

It is, however, known that the mechanical response of various epoxy resins may considerably vary. This is seen in Fig. 1.2 showing the results from several rate dependent tensile tests. Clearly, it is not just the type of epoxy resin, but as evident in Fig. 1.2(a) even the type of hardener may have a great influence on the material response. Apart from that, the rate of loading also plays an important role. We observe in Fig. 1.2(a) a merely viscous behavior, as

one would expect for the polymer material, being shifted towards brittle-viscous, Fig. 1.2(b), or even brittle, Fig. 1.2(c), behavior with essentially no viscous effects.

Obviously, such a different response not only influences the behavior and thus the range of applications of the corresponding composite material, but also drives the choice of the numerical method when we wish to make any predictions numerically.

1.5 Organization of thesis

The above paragraphs motivated the content of this thesis embedded in the principal goals summarized in Chapter 2. The common bond is the analysis of polymer matrix based textile composites. The current interest in basalt, almost isotropic, fibers and an ongoing interest in carbon, highly orthotropic, fibers influenced the choice of textile reinforcements, while the matrices were selected based on their availability. But as suggested in Fig. 1.2 this brought the main challenge.

To successfully complete the thesis we did not attempt to provide a unified formulation of the model capable of addressing the whole complexity of the matrix behavior. Instead, the viscose and brittle response was addressed separately, but with a common computational framework of the first order homogenization described in Chapter 3. Modeling of viscoelastic behavior of textile composites is presented in Chapters 4 and 5 starting with the formulation (Section 4.1) and calibration (Section 4.2) of the generalized Leonov (nonlinear viscoelastic) model. A comparative numerical study of the two types reinforcements was performed next, first addressing the elastic response of the composite (Section 5.1) followed by numerical simulations carried out at the level of a yarn (Section 5.2) and completed by the multiscale analysis at the level of a textile ply (Section 5.3). Modeling the textile composites with brittle or quasi-brittle behavior of the matrix phase is presented in Chapter 6, again in the framework of multiscale analysis, thus on the yarn scale and subsequently on the scale of the textile ply. The principal outcomes of the thesis with potential future research directions are finally summarized in Chapter 7.

Chapter 2

THESIS OBJECTIVES

1. Implementation of a suitable viscoelastic model representing the response of a viscous matrix based textile composites into the selected finite element code.

2. Calibration of the implemented viscoelastic model.

3. Implementation of the Mori-Tanaka into the selected finite element code to allow for an efficient two scale modeling of textile composites.

4. Reformulation of the original format of the Mori-Tanaka method to provide response comparable with the finite element predictions.

5. Evaluation of the effect of random microstructure on the response provided by the Mori-Tanaka method.

6. Simulation of the macroscopic response of carbon and basalt textile composites via a two-step homogenization combining the finite element and the Mori-Tanaka methods.

7. Implementation of a suitable damage model representing the response of a brittle matrix based unidirectional fibrous composites into the selected finite element code.

8. Calibration of the implemented damage model and derivation of effective fracture properties of a single fiber tow.

Chapter 3

HOMOGENIZATION OF TEXTILE COMPOSITES

To introduce the subject we consider a representative volume of a single ply balanced plain weave composite plotted in Fig. 3.1 with a potential distribution of fibers in the transverse cross-section being represented by a periodic hexagonal array model. These simple geometrical representations allow for a standard periodic homogenization to be exploited on the mesoscopic (ply) as well as microscopic (yarn) scales.

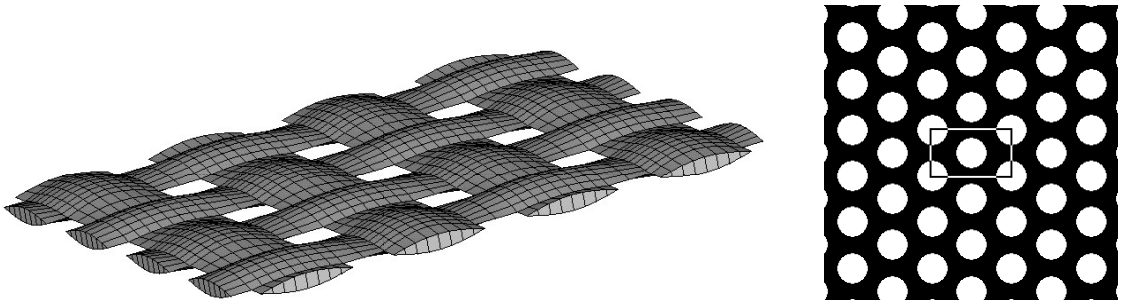

(a) (b)

Figure 3.1: a) Single textile ply showing identical geometry of yarns in both warp and weft direction, b) Hexagonal arrangement of unidirectional fibers in yarn transverse direction

When limiting attention to elasticity, a simple bottom-up fully uncoupled homogenization can be used to predict the macroscopic effective properties of a single ply textile composite. This, however, is no longer possible when loading the composite beyond the elastic regime as the material anisotropy precludes derivation of the homogenized nonlinear constitutive law at the level of yarn. A two step, fully coupled homogenization, is therefore needed. Two options are typically available:

1. Analysis in the framework of FE^2 approach. In this case, the finite element (FE) homogenization is carried out both at the level of yarns and textile ply adopting a suitable computational model at each scale, e.g., the periodic unit cells extracted from composites in Fig. 3.1. In this approach, the ply RVE (mesoscale) is typically loaded by the prescribed macroscopic strains or stresses, while the yarn RVE (microscale) is

subjected to strains developed at an integration point of a finite element located in the yarn. On return, the updated stress averages and potentially the modified yarn effective properties are transferred back on to the mesoscale.

2. The FE^2 approach might be computationally too demanding. This suggests combination of the finite element method at the level of textile ply and the computationally efficient Mori-Tanaka (MT) method which replaces the finite element analysis at the level of yarns. This approach in particular will be examined in the present thesis. A graphical representation of this two-step modeling strategy, where $\Delta\overline{\boldsymbol{\varepsilon}}$ is the mesoscopic strain at a given point of the mesoscopic finite element mesh and $\Delta\overline{\boldsymbol{\sigma}}$ is the corresponding mesoscopic stress increment provided by the Mori-Tanaka method, is shown in Fig. 3.2. The eigenstrain $\Delta\boldsymbol{\mu}$ might be associated with many physical sources, but only the viscoelastic effects are considered in the thesis.

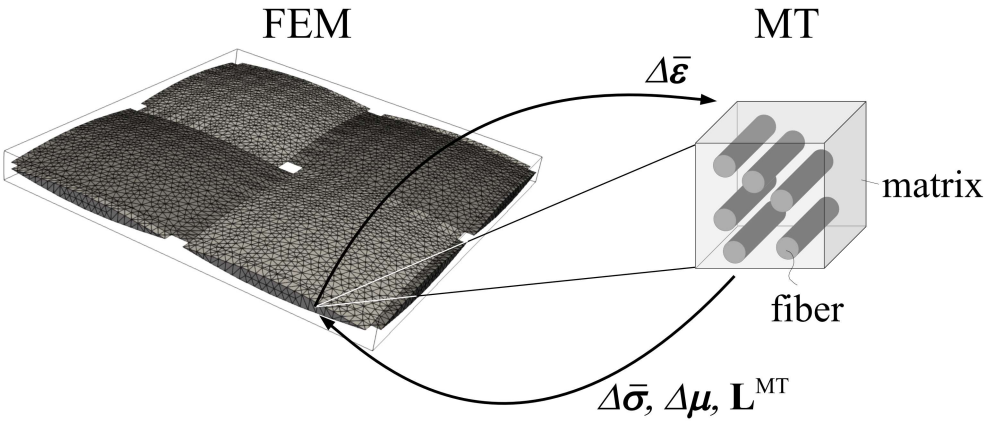

Figure 3.2: Graphical representation of two-scale computational scheme combining FEM at the level of textile ply and the MT method at the level of yarn

Both homogenization approaches, FE and MT method based, will be now briefly reviewed. Only the most relevant formulations will be outlined. Thus for more details, the interested reader is referred to (Dvorak, 2013; Šejnoha and Zeman, 2013). Thought these formulations are generally applicable to any material symmetry, we assume that the matrix phase is isotropic, whereas the material symmetry of the fiber phase corresponds to transverse isotropy. In the latter case, the 6×6 material stiffness matrix $\mathbf{L}$ assumes the form

$$\left\{\begin{array}{c}\sigma_x\\ \sigma_y\\ \sigma_z\\ \tau_{yz}\\ \tau_{xz}\\ \tau_{xy}\end{array}\right\} = \left[\begin{array}{cccccc} k+m & k-m & l & 0 & 0 & 0\\ k-m & k+m & l & 0 & 0 & 0\\ l & l & n & 0 & 0 & 0\\ 0 & 0 & 0 & p & 0 & 0\\ 0 & 0 & 0 & 0 & p & 0\\ 0 & 0 & 0 & 0 & 0 & m \end{array}\right] \left\{\begin{array}{c}\varepsilon_x\\ \varepsilon_y\\ \varepsilon_z\\ \gamma_{yz}\\ \gamma_{xz}\\ \gamma_{xy}\end{array}\right\}, \quad \boldsymbol{\sigma} = \mathbf{L}\boldsymbol{\varepsilon} \tag{3.1}$$

where

$$\begin{aligned} k &= -\left[1/G_{\mathrm{T}} - 4/E_{\mathrm{T}} + 4\nu_{\mathrm{L}}^2/E_{\mathrm{L}}\right]^{-1}\\ m &= G_{\mathrm{T}}\\ l &= 2k\nu_{\mathrm{L}}\\ n &= E_{\mathrm{L}} + 4k\nu_{\mathrm{L}}^2 = E_{\mathrm{L}} + l^2/k\\ p &= G_{\mathrm{L}} \end{aligned} \tag{3.2}$$

where E_{L} is the longitudinal Young modulus, G_{L} is the longitudinal shear modulus, ν_{L} is the longitudinal Poisson ratio, E_{T} is the transverse Young modulus, and G_{T} is the transverse shear modulus. The transverse $xy-$plane is the plane of isotropy.

3.1 First order homogenization using finite element method

The first-order homogenization outlined in this sections grounds on the formulation developed in (Michel et al., 1999). To this end, suppose that a periodic unit cell (PUC) Y, representing all the geometrical and material details of the whole composite, is loaded on its outer boundary by the prescribed displacements or tractions that produce the macroscopically uniform strains $\boldsymbol{E}$ or stresses $\boldsymbol{\Sigma}$ in an equivalent homogeneous medium. The macroscopic constitutive equations then read

$$\Delta\boldsymbol{\Sigma} = \mathbf{L}^{\mathsf{hom}}\Delta\boldsymbol{E} + \Delta\boldsymbol{\Lambda}, \qquad \Delta\boldsymbol{E} = \mathbf{M}^{\mathsf{hom}}\Delta\boldsymbol{\Sigma} + \Delta\boldsymbol{\Upsilon} \tag{3.3}$$

where $\mathbf{L}^{\mathsf{hom}}$ and $\mathbf{M}^{\mathsf{hom}}$ are the instantaneous effective (homogenized) stiffness and compliance matrices, respectively, and $\Delta\boldsymbol{\Lambda}$, and $\Delta\boldsymbol{\Upsilon}$ are the corresponding eigenstresses and eigenstrains. We choose an incremental format in view of the nonlinear viscoelastic model de-

scribed later in Section 4.1. The macroscopic strains and stresses are related to volume strains and stress averages of local fields developed in individual phase $r = f(\text{fiber,yarn}), m(\text{matrix})$ as

$$\Delta \boldsymbol{E} = \langle \Delta \boldsymbol{\varepsilon}(\boldsymbol{x}) \rangle = \sum_{r}^{2} c_r \Delta \boldsymbol{\varepsilon}_r, \qquad \Delta \boldsymbol{\Sigma} = \langle \Delta \boldsymbol{\sigma}(\boldsymbol{x}) \rangle = \sum_{r}^{2} c_r \Delta \boldsymbol{\sigma}_r \tag{3.4}$$

where $\langle \cdot \rangle$ stands for volume averaging, c_r is the volume fraction of a given phase r and $\Delta \boldsymbol{\varepsilon}_r$ and $\Delta \boldsymbol{\sigma}_r$ are increments of piece-wise uniform phase strains and stresses, respectively, see (Šejnoha and Zeman, 2013) for further details. Similar to Eq. (3.3), the local fields can be written in terms of the phase material stiffness $\mathbf{L}_r$ and compliance $\mathbf{M}_r$ matrices as

$$\Delta \boldsymbol{\sigma}_r = \mathbf{L}_r \Delta \boldsymbol{\varepsilon}_r + \Delta \boldsymbol{\lambda}_r, \qquad \Delta \boldsymbol{\varepsilon}_r = \mathbf{M}_r \Delta \boldsymbol{\sigma}_r + \Delta \boldsymbol{\mu}_r \tag{3.5}$$

where $\Delta \boldsymbol{\mu_r}$ and $\Delta \boldsymbol{\lambda}_r = -\mathbf{L}_r \Delta \boldsymbol{\mu}_r$ are increments of local phase eigenstrains and eigenstresses. In the present study, only the viscoelastic strain $\Delta \boldsymbol{\mu}_m$ developed in the matrix will be considered.

Point out that Eqs. (3.3) follow directly from Hill's lemma (Hill, 1963). Hill proved that for the assumed uniform loading conditions the volume average of the internal work (virtual work) done by local fields equals to the internal work (virtual work) done by their macroscopic counterparts. This statement is mathematically written as

$$\left\langle \delta \boldsymbol{\varepsilon}(\boldsymbol{x})^{\mathsf{T}} \Delta \boldsymbol{\sigma}(\boldsymbol{x}) \right\rangle = \delta \boldsymbol{E}^{\mathsf{T}} \Delta \boldsymbol{\Sigma} \tag{3.6}$$

Because in the displacement based finite element method the primary unknowns are the nodal displacements, we continue by decomposing the local displacements, while taking into account the periodicity of the unit cell, into a homogeneous $\Delta \boldsymbol{E} \cdot \boldsymbol{x}$ and fluctuations $\Delta \boldsymbol{u}^*$ parts as

$$\Delta \boldsymbol{u}(\boldsymbol{x}) = \Delta \boldsymbol{E} \cdot \boldsymbol{x} + \Delta \boldsymbol{u}^*(\boldsymbol{x}), \qquad \Delta \boldsymbol{\varepsilon}(\boldsymbol{x}) = \Delta \boldsymbol{E} + \Delta \boldsymbol{\varepsilon}^*(\boldsymbol{x}) \tag{3.7}$$

where Eq. $(3.7)_2$ follows from standard strain-displacement relations. Next, substituting from Eq. $(3.7)_2$ into Eq. (3.6) and realizing that

$$\Delta \boldsymbol{\sigma}(\boldsymbol{x}) = \mathbf{L}(\boldsymbol{x}) \Delta \boldsymbol{\varepsilon}(\boldsymbol{x}) + \Delta \boldsymbol{\lambda}(\boldsymbol{x}) \tag{3.8}$$

provides Hill's lemma in the form

$$\delta \boldsymbol{E}^{\mathsf{T}} \left\langle \mathbf{L}(\boldsymbol{x})(\Delta \boldsymbol{E} + \Delta \boldsymbol{\varepsilon}^*(\boldsymbol{x})) + \Delta \boldsymbol{\lambda}(\boldsymbol{x}) \right\rangle + \left\langle \delta \boldsymbol{\varepsilon}^{*\mathsf{T}} [\mathbf{L}(\boldsymbol{x})(\Delta \boldsymbol{E} + \Delta \boldsymbol{\varepsilon}^*(\boldsymbol{x})) + \Delta \boldsymbol{\lambda}(\boldsymbol{x})] \right\rangle = \delta \boldsymbol{E} \Delta \boldsymbol{\Sigma} \tag{3.9}$$

Because the variations $\delta\boldsymbol{E}$ and $\delta\boldsymbol{\varepsilon}^*$ are independent, Eq. (3.9) can be split into two equalities

$$\delta\boldsymbol{E}^{\mathsf{T}}\Delta\boldsymbol{\Sigma} = \delta\boldsymbol{E}^{\mathsf{T}}(\langle\mathbf{L}(\boldsymbol{x})\rangle\,\Delta\boldsymbol{E} + \langle\mathbf{L}(\boldsymbol{x})\Delta\boldsymbol{\varepsilon}^*(\boldsymbol{x})\rangle + \langle\Delta\boldsymbol{\lambda}(\boldsymbol{x})\rangle) \tag{3.10}$$

$$0 = \left\langle\delta\boldsymbol{\varepsilon}^{*\mathsf{T}}\mathbf{L}(\boldsymbol{x})\right\rangle\Delta\boldsymbol{E} + \left\langle\delta\boldsymbol{\varepsilon}^{*\mathsf{T}}\mathbf{L}(\boldsymbol{x})\Delta\boldsymbol{\varepsilon}^*(\boldsymbol{x})\right\rangle + \left\langle\delta\boldsymbol{\varepsilon}^{*\mathsf{T}}\Delta\boldsymbol{\lambda}(\boldsymbol{x})\right\rangle \tag{3.11}$$

Equation (3.10) is to be solved for unknown increments of macroscopic $\Delta\boldsymbol{E}$ and fluctuation $\Delta\boldsymbol{\varepsilon}^*$ strain fields. In the framework of FEM the fluctuation displacements $\boldsymbol{u}^*$ rather than the total displacements $\boldsymbol{u}$ will be considered as the primary unknowns. Standard finite element discretization then reads

$$\Delta\boldsymbol{u}^*(\boldsymbol{x}) = \mathbf{N}(\boldsymbol{x})\Delta\boldsymbol{r}, \qquad \Delta\boldsymbol{\varepsilon}(\boldsymbol{x}) = \Delta\boldsymbol{E} + \mathbf{B}(\boldsymbol{x})\Delta\boldsymbol{r} \tag{3.12}$$

where matrix $\mathbf{N}$ stores the shape functions for a given partition of the unit cell, $\boldsymbol{B}$ is the corresponding geometrical matrix, and $\boldsymbol{r}$ is the vector of unknown nodal degrees of freedom. Introducing the fluctuation strains from Eq. 3.12 into Eq. (3.10) provides the final set of discretized equations of equilibrium in the form

$$\begin{bmatrix} \int_\Omega \mathbf{L}(\boldsymbol{x})\,\mathrm{d}\Omega & \int_\Omega \mathbf{L}(\boldsymbol{x})\mathbf{B}(\boldsymbol{x})\,\mathrm{d}\Omega \\ \int_\Omega \mathbf{B}(\boldsymbol{x})^{\mathsf{T}}\mathbf{L}(\boldsymbol{x})\,\mathrm{d}\Omega & \int_\Omega \mathbf{B}(\boldsymbol{x})^{\mathsf{T}}\mathbf{L}(\boldsymbol{x})\mathbf{B}(\boldsymbol{x})\,\mathrm{d}\Omega \end{bmatrix} \begin{Bmatrix} \Delta\boldsymbol{E} \\ \Delta\boldsymbol{r} \end{Bmatrix} = \begin{Bmatrix} \Delta\boldsymbol{\Sigma}\Omega - \int_\Omega \Delta\boldsymbol{\lambda}(\boldsymbol{x})\,\mathrm{d}\Omega \\ -\int_\Omega \mathbf{B}(\boldsymbol{x})^{\mathsf{T}}\Delta\boldsymbol{\lambda}(\boldsymbol{x})\,\mathrm{d}\Omega \end{Bmatrix} \tag{3.13}$$

where Ω represents the unit cell volume.

It is worth mentioning that the fluctuation displacements $\boldsymbol{u}^*$ must satisfy certain conditions so that the following relations hold

$$\langle\Delta\boldsymbol{\varepsilon}(\boldsymbol{x})\rangle = \Delta\boldsymbol{E}, \qquad \langle\boldsymbol{\varepsilon}^*(\boldsymbol{x})\rangle = \mathbf{0} \tag{3.14}$$

Point out that Eq. $(3.14)_2$ is for example satisfied when enforcing homogeneous displacements $\boldsymbol{r}$ on the entire boundary of the unit cell Y. Usually, better predictions are obtained when considering periodic boundary conditions which for rectangular PUC amount to enforcing the same fluctuation displacements on opposite faces of PUC. To avoid writing any master-slave type of constrains it is preferable to consider periodic meshes. The periodicity condition is then enforced simply by assigning the same code numbers to the corresponding degrees of freedom on opposite faces of PUC.

When deriving Eq (3.13) we explicitly assumed that the macroscopic stress increment $\Delta\boldsymbol{\Sigma}$ is prescribed thus considering the stress based approach (Šejnoha and Zeman, 2013).

However, the strain based formulation is often needed. In such a case, the unit cell is loaded by the prescribed macroscopic strain $\Delta \boldsymbol{E}$. The virtual change of the prescribed quantity then vanishes ($\delta \boldsymbol{E} = 0$) and Eq. (3.13) simplifies to

$$\int_{\Omega} \mathbf{B}(\boldsymbol{x})^{\mathsf{T}} \mathbf{L}(\boldsymbol{x}) \mathbf{B}(\boldsymbol{x}) \, \mathrm{d}\Omega \Delta \boldsymbol{r} = - \int_{\Omega} \mathbf{B}(\boldsymbol{x})^{\mathsf{T}} \mathbf{L}(\boldsymbol{x}) \Delta \boldsymbol{E} \, \mathrm{d}\Omega - \int_{\Omega} \mathbf{B}(\boldsymbol{x})^{\mathsf{T}} \Delta \boldsymbol{\lambda}(\boldsymbol{x}) \, \mathrm{d}\Omega \qquad (3.15)$$

When limiting attention to elasticity Eqs. (3.13) and (3.15) can be used to estimate the effective elastic stiffness or compliance matrices we introduced in Eq. (3.3). In particular, using Eq. (3.13) the effective compliance matrix $\mathbf{M}^{\mathsf{hom}}$ can be obtained by loading PUC in turn by each of the six components of $\boldsymbol{\Sigma}$ set equal to 1, while the other five components vanish. The volume strain averages then supply individual columns of $\mathbf{M}^{\mathsf{hom}}$. The stiffness matrix $\mathbf{L}^{\mathsf{hom}}$ is derived analogously from Eq. (3.15) again by running six elasticity analyses where the unit states of macroscopic strain $\mathbf{E}$ are prescribed. The volume stress averages then correspond to individual columns of $\mathbf{L}^{\mathsf{hom}}$. For practical application of this procedure we refer to Section 5.1. Note that general 3D formulation will be adopted when studying the textile ply, while the homogenization at the level of yarn will be performed assuming plane-strain conditions. Such a simplification thus does not allow for the prediction of out-of-plane longitudinal shear modulus. This parameter can, however, be estimated from the MT method described in the next section.

3.2 Mori Tanaka method in framework of Dvorak's transformation field analysis

The Mori-Tanaka method belongs to the class of micromechanical models that ground on the Eshelby solution of an ellipsoidal inclusion problem where a single inclusion is imagined in an unbounded homogeneous body loaded at infinity by a uniform stress or strain (Eshelby, 1957) fields. Eshelby showed that in such a case the distribution of inclusion strains and stresses is also uniform and derived a localization tensor that identifies the inclusion strain and stresses in terms of the applied far fields, material properties of the two phases and geometry of the inclusion. A number of existing micromechanical models take advantage of this result and attempt to extend the Eshelby solution to a composite with a large number of interacting inclusions. In his reformulation of the original Mori-Tanaka method (Mori and Tanaka, 1973), Benveniste (Benveniste, 1987) showed that the MT method accounts for the interaction of inclusions by introducing a single inclusion into an infinite matrix, but

unlike the Eshelby solution this system is loaded by yet unknown average strain or stress found in the matrix phase. This method is therefore explicit and for that reason enjoys popularity. As there is voluminous literature on this subject we do not attempt to present all the details of the method but provide just the relations needed in the context of this thesis. To become more familiar with this method we point the interested reader to the following two monographs (Dvorak, 2013; Šejnoha and Zeman, 2013).

To be consistent with the previous section we consider again a two-phase fiber-matrix composite and write the local constitutive equations $(3.5)_1$ assuming elastic response of the fiber phase and viscoelastic response of the matrix as

$$\Delta\boldsymbol{\sigma}_f = \mathbf{L}_f \Delta\boldsymbol{\varepsilon}_f, \qquad \Delta\boldsymbol{\sigma}_m = \widehat{\mathbf{L}}_m \Delta\boldsymbol{\varepsilon}_m + \Delta\boldsymbol{\lambda}_m \tag{3.16}$$

where $\mathbf{L}_r$, $r = f, m$[1], is the phase material stiffness matrix and $\widehat{(\cdot)}$ represents the dependence on the current viscoelastic shear modulus as will become evident later in Section 4.1. The local strains in individual phases follow from the application of Dvorak's transformation field analysis (Dvorak and Benveniste, 1992) and are provided by

$$\Delta\boldsymbol{\varepsilon}_f = \widehat{\mathbf{A}}_f \Delta\boldsymbol{E} + \widehat{\boldsymbol{D}}_{fm} \Delta\boldsymbol{\mu}_m, \qquad \Delta\boldsymbol{\varepsilon}_m = \widehat{\mathbf{A}}_m \Delta\boldsymbol{E} + \widehat{\boldsymbol{D}}_{mm} \Delta\boldsymbol{\mu}_m \tag{3.17}$$

where $\widehat{\boldsymbol{A}}_r$ and $\widehat{\boldsymbol{D}}_{rm}$ are the mechanical strain localization factors and strain and stress transformation influence functions, respectively. It can be shown (Dvorak and Benveniste, 1992; Dvorak, 2013) that for a two-phase composite the transformation influence functions are readily provided in terms of the localization factors as

$$\widehat{\mathbf{D}}_{fm} = \left(\mathbf{I} - \widehat{\mathbf{A}}_f\right)\left(\widehat{\mathbf{L}}_m - \mathbf{L}_f\right)^{-1}\widehat{\mathbf{L}}_m, \qquad \widehat{\mathbf{D}}_{mm} = \left(\mathbf{I} - \widehat{\mathbf{A}}_m\right)\left(\widehat{\mathbf{L}}_m - \mathbf{L}_f\right)^{-1}\widehat{\mathbf{L}}_m \tag{3.18}$$

It remains to determine the mechanical strain localization factors $\mathbf{A}_r$. To do so, we consider, in light of the MT method, a single inclusion of an elliptical shape being embedded into an unbounded matrix, which is loaded at infinity by the average strain in the matrix phase as shown in Fig. 3.3.

In the absence of viscoelastic contribution the strain increment in the fiber phase can be then written with the help of partial strain localization factor $\widehat{\mathbf{T}}_f$ as

$$\Delta\boldsymbol{\varepsilon}_f = \widehat{\mathbf{T}}_f \Delta\boldsymbol{\varepsilon}_m \tag{3.19}$$

[1] Subscripts f, m stand for the fiber and matrix phase, respectively.

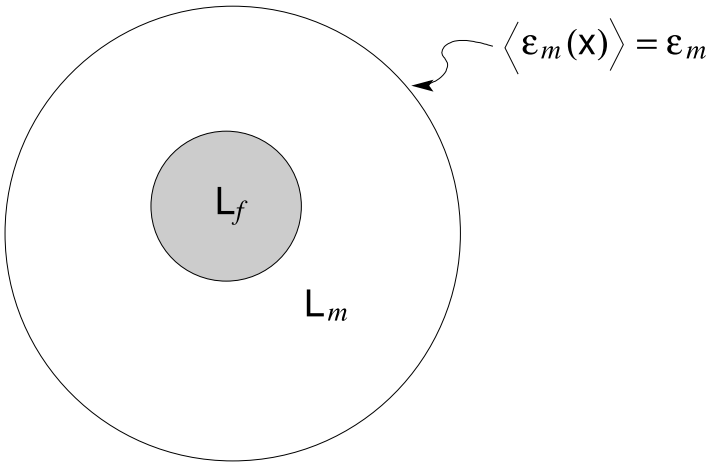

Figure 3.3: Mori-Tanaka method - graphical representation

With reference to Eq. $(3.4)_1$ it is now possible to express the average matrix strain increment $\Delta\boldsymbol{\varepsilon}_m$ in the form

$$\Delta\boldsymbol{\varepsilon}_m = \left[c_m \boldsymbol{I} + c_f \widehat{\mathbf{T}}_f\right]^{-1} \Delta\boldsymbol{E} = \widehat{\mathbf{A}}_m \Delta\boldsymbol{E} \tag{3.20}$$

where $\mathbf{I}$ is the identity matrix. Substituting the right hand side of Eq. (3.20) back to Eq. (3.19) finally gives

$$\Delta\boldsymbol{\varepsilon}_f = \widehat{\mathbf{T}}_f \left[c_m \boldsymbol{I} + c_f \widehat{\mathbf{T}}_f\right]^{-1} \Delta\boldsymbol{E} = \widehat{\mathbf{A}}_f \Delta\boldsymbol{E} \tag{3.21}$$

Without derivation, see for example (Eshelby, 1957) for details, we provide the particular form of $\widehat{\mathbf{T}}_f$, the result of the Eshelby transformation inclusion problem, as

$$\widehat{\mathbf{T}}_f = \left[\mathbf{I} - \widehat{\mathbf{P}}(\widehat{\mathbf{L}}_m - \mathbf{L}_f)\right]^{-1} \tag{3.22}$$

The matrix $\mathbf{P}$ depends on the properties of the matrix phase and geometry of the inclusion and for the case of infinite longitudinal fibers, the only type of inclusion considered in this

study, is given by (Walpole, 1969)

$$\mathbf{P} = \begin{bmatrix} 0 & 0 & 0 & 0 & 0 & 0 \\ 0 & \dfrac{k+4m}{8m(k+m)} & \dfrac{-k}{8m(k+m)} & 0 & 0 & 0 \\ 0 & \dfrac{-k}{8m(k+m)} & \dfrac{k+4m}{8m(k+m)} & 0 & 0 & 0 \\ 0 & 0 & 0 & \dfrac{k+2m}{2m(k+m)} & 0 & 0 \\ 0 & 0 & 0 & 0 & \dfrac{1}{2p} & 0 \\ 0 & 0 & 0 & 0 & 0 & \dfrac{1}{2p} \end{bmatrix} \tag{3.23}$$

where k, m, p are the Hill moduli of the matrix phase introduced in Eq. (3.2).

As mentioned at the beginning of this chapter, the multiscale analysis will require the knowledge of the homogenized stiffness matrix, overall stress and eigenstress associated with a lower scale, here being represented by the level of yarn (microscale). For the sake of simplicity we assume that the mesoscopic strains and stresses are denoted by $\boldsymbol{E}$ and $\boldsymbol{\Sigma}$, respectively. A slight change of notation to properly distinguish individual scales will be introduced in Section 5.3.

With this assumption at hand the average mesoscopic stress follows directly from stress averaging Eq. $(3.4)_2$. Thus, substituting the local stress increments from Eq. (3.16) into Eq. $(3.4)_2$ and using relations (3.17) together with $\Delta\boldsymbol{\lambda}_m = -\widehat{\mathbf{L}}_m \Delta\boldsymbol{\mu}_m$ yields

$$\begin{aligned} \Delta\boldsymbol{\Sigma} &= c_f \Delta\boldsymbol{\sigma}_f + c_m \Delta\boldsymbol{\sigma}_m = c_f \mathbf{L}_f \Delta\boldsymbol{\varepsilon}_f + c_m \widehat{\mathbf{L}}_m \left(\Delta\boldsymbol{\varepsilon}_m - \Delta\boldsymbol{\mu}_m\right) \\ &= c_f \mathbf{L}_f (\widehat{\mathbf{A}}_f \Delta\boldsymbol{E} + \widehat{\boldsymbol{D}}_{fm} \Delta\boldsymbol{\mu}_m) + c_m \widehat{\mathbf{L}}_m (\widehat{\mathbf{A}}_m \Delta\boldsymbol{E} + \widehat{\boldsymbol{D}}_{mm} \Delta\boldsymbol{\mu}_m) - c_m \widehat{\mathbf{L}}_m \Delta\boldsymbol{\mu}_m \\ &= (c_f \mathbf{L}_f \widehat{\mathbf{A}}_f + c_m \widehat{\mathbf{L}}_m \widehat{\mathbf{A}}_m) \Delta\boldsymbol{E} + \\ &+ (c_f \mathbf{L}_f \widehat{\mathbf{D}}_{fm} + c_f \widehat{\mathbf{L}}_m \widehat{\mathbf{D}}_{mm} - c_m \widehat{\mathbf{L}}_m) \Delta\boldsymbol{\mu}_m \end{aligned} \tag{3.24}$$

Comparing Eq. (3.24) with Eq. $(3.3)_1$ finally gives the homogenized stiffness matrix $\mathbf{L}^{\mathsf{hom}}_{\mathsf{MT}}$ and the increment of mesoscopic eigenstress $\Delta\boldsymbol{\Lambda}_{\mathsf{MT}}$

$$\mathbf{L}^{\mathsf{hom}}_{\mathsf{MT}} = c_f \mathbf{L}_f \widehat{\mathbf{A}}_f + c_m \widehat{\mathbf{L}}_m \widehat{\mathbf{A}}_m \tag{3.25}$$

$$\Delta\boldsymbol{\Lambda}_{\mathsf{MT}} = (c_f \mathbf{L}_f \widehat{\mathbf{D}}_{fm} + c_f \widehat{\mathbf{L}}_m \widehat{\mathbf{D}}_{mm} - c_m \widehat{\mathbf{L}}_m) \Delta\boldsymbol{\mu}_m \tag{3.26}$$

Chapter 4

GENERALIZED LEONOV MODEL

It has been shown in the introductory part that the polymer matrices adopted in the present study exhibit a strain rate dependent nonlinear viscoelastic response. It has also been experimentally observed that polymers show, in general, a negligible volumetric strain during plastic flow. This is supported in (Valenta and Šejnoha, 2004) where the application of the generalized Leonov model proved useful in the modeling of such materials. This is also why this constitutive model is exploited in the present work. As details of the model can be found in a number of contributions, see e.g. (Tervoort, 1996; Valenta, 2011), we address the theoretical grounds of the model only shortly in Section 4.1 while concentrating on the calibration details in Section 4.2.

4.1 Formulation of generalized Leonov model

The stepping stone in the formulation of the Leonov model is the Eyring flow equation representing the plastic component of the shear strain rate in the form

$$\frac{\mathrm{d}e_p}{\mathrm{d}t} = \frac{1}{2A}\sinh(\tau/\tau_0) \tag{4.1}$$

The total shear strain rate combining the elastic and plastic strain rates then becomes

$$\frac{\mathrm{d}e}{\mathrm{d}t} = \frac{\mathrm{d}e_e}{\mathrm{d}t} + \frac{\mathrm{d}e_p}{\mathrm{d}t} = \frac{\mathrm{d}e_e}{\mathrm{d}t} + \frac{\tau}{\eta(\,\mathrm{d}e_p/\,\mathrm{d}t)} \tag{4.2}$$

which is the one-dimensional Leonov constitutive (Leonov, 1976) model with the shear-dependent viscosity η given by

$$\eta(\,\mathrm{d}e_p/\,\mathrm{d}t) = \frac{\eta_0\tau}{\tau_0\sinh(\tau/\tau_0)} = \eta_0 a_\sigma(\tau) \tag{4.3}$$

where τ is the shear stress and A, τ_0 are the model parameters, η_0 is the viscosity corresponding to a linear viscoelastic response and a_σ is the stress dependent shift factor. Notice that Eq. (4.2) represents a single Maxwell unit with a variable viscosity. To describe the material response sufficiently accurately, the generalized Maxwell chain model in Fig. 4.1 is typically used.

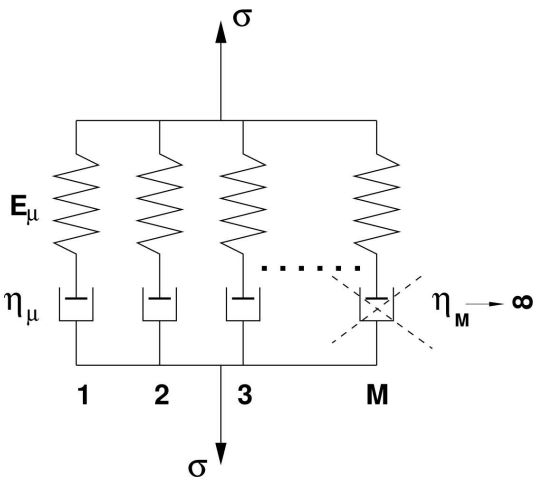

Figure 4.1: Maxwell chain model

Extension to multidimensional behavior introduces an equivalent deviatoric stress τ_{eq}

$$\tau_{eq} = J = \sqrt{J_2} = \sqrt{\frac{1}{2}\boldsymbol{s}^{\mathsf{T}}\mathbf{Q}^{-1}\boldsymbol{s}}, \quad \mathbf{Q} = \text{diag}\left[1,1,1,\frac{1}{2},\frac{1}{2},\frac{1}{2}\right] \tag{4.4}$$

where $\boldsymbol{s}$ is the deviatoric stress vector. The viscosity of the μ_{th} unit is then provided by

$$\eta_\mu = \eta_{0,\mu} a_\sigma(\tau_{eq}) = \frac{\eta_{0,\mu}\tau_{eq}}{\tau_0 \text{sinh}(\tau_{eq}/\tau_0)} \tag{4.5}$$

Admitting material isotropy, small strain theory, and the bulk response to be linearly elastic we arrive at the complete set of constitutive equations defining the compressible generalized Leonov model

$$\sigma_m = K\varepsilon_v \tag{4.6}$$

$$\frac{\mathrm{d}\boldsymbol{s}}{\mathrm{d}t} = \sum_{\mu=1}^{M} 2G_\mu \mathbf{Q}\left(\frac{\mathrm{d}\boldsymbol{e}}{\mathrm{d}t} - \frac{\mathrm{d}\boldsymbol{e}_{p,\mu}}{\mathrm{d}t}\right), \quad \boldsymbol{s} = \sum_{\mu=1}^{M}\boldsymbol{s}_\mu \tag{4.7}$$

$$\boldsymbol{s}_\mu = 2\eta_\mu \mathbf{Q}\frac{\mathrm{d}\boldsymbol{e}_{p,\mu}}{\mathrm{d}t} = 2\eta_{0,\mu}a_\sigma(\tau_{eq})\mathbf{Q}\frac{\mathrm{d}\boldsymbol{e}_{p,\mu}}{\mathrm{d}t} \tag{4.8}$$

where $\sigma_m = \frac{1}{3}(\sigma_x + \sigma_y + \sigma_z)$ is the mean stress, $\varepsilon_v = (\varepsilon_x + \varepsilon_y + \varepsilon_z)$ is the volumetric strain, K is the material bulk modulus, G_μ is the shear modulus, associated with the μ-th unit, $\boldsymbol{e} = \boldsymbol{\varepsilon} - \frac{1}{3}\mathbf{m}\varepsilon_v$ stores the components of the deviatoric strain and $\mathbf{m}^{\mathsf{T}} = \{1,1,1,0,0,0\}$. To integrate Eq. (4.7) in time we settle for the most simple fully explicit forward Euler integration. Provided that the total strain rate is constant during integration a new state of

stress in the matrix phase at the end of the current time step Δt assumes the form

$$\sigma_m(t_i) = \sigma_m(t_{i-1}) + K\Delta\varepsilon_v \tag{4.9}$$

$$\boldsymbol{s}(t_i) = \boldsymbol{s}(t_{i-1}) + 2\widehat{G}(t_{i-1})\mathbf{Q}\Delta\boldsymbol{e} + \Delta\boldsymbol{\lambda}(t_{i-1}) \tag{4.10}$$

where t_i is the current time at the end of the i-th time increment. In light of the assumed Dirichlet series expansion to represent the shear relaxation function, see ahead Section 4.2, the instantaneous shear modulus $\widehat{G}$ and the increment of eigenstress $\Delta\boldsymbol{\lambda}$, recall Eq. (3.16), read

$$\widehat{G} = \sum_{\mu=1}^{M} G_\mu \frac{\theta_\mu a_\sigma(t_{i-1})}{\Delta t}\left[1 - \exp\left(-\frac{\Delta t}{\theta_\mu a_\sigma(t_{i-1})}\right)\right] \tag{4.11}$$

$$\Delta\boldsymbol{\lambda} = -\sum_{\mu=1}^{M}\left[1 - \exp\left(-\frac{\Delta t}{\theta_\mu a_\sigma(t_{i-1})}\right)\right]\boldsymbol{s}_\mu(t_{i-1}) \tag{4.12}$$

4.2 Calibration of generalized Leonov model

Although formulation presented in the previous section would promote loading the specimens in shear (Valenta, 2011; Šejnoha and Zeman, 2013), we proceed in the footsteps set in (Tervoort, 1996) and adopt standard tensile tests performed at different strain rates and standard creep tests carried out at different stress levels. This will allow us to calibrate both the Eyring flow model and Maxwell chain model.

(a) (b)

Figure 4.2: Specimens used in tensile and creep tests: a) Prior to testing, b) After testing

Flat specimens of a dog-bone type, seen in Fig. 4.2, were used in all experiments. All specimens were produced in a standard way by first mixing the epoxy resin at room temperature for about 10 minutes with a corresponding hardener via magnetic stirrers. The mixing

ratio by weight (resin:hardener) for individual epoxy resins is available in Table 4.1 [1]. The mixture was then cured in a mold for about 24 hours at room temperature and subsequently post-cured for additional 15 hours at higher temperature of 60°C.

Table 4.1: Basic parameters of epoxy resins (25°C)

Parameter	L285	E455	E520
Mixing ratio by wight	100:40	100:22	100:26
Viscosity [Pa.s]	0.6-0.9	>20	12-14.5
Density [g/cm^3]	1.18-1.23	>1.16	>1.16
Modulus of elasticity [GPa]	3.0-3.3		
Tensile strength [MPa]	70-80	>30	>40
Compressive strength [MPa]		>60	
Bending strength [MPa]	65		>90

The L285 epoxy based specimens were initially prepared with H508 hardener. These specimens were used in tensile tests only. Expecting the same properties, the second set of specimens was produced, mainly because of availability, with H500 hardener. It will, however, be seen that the specimens manufactured with the two hardeners considerably differ in their mechanical response. The specimens based on the remaining two resins (E455, E520) were produced with the help of H492 hardener. Selected physical properties of the three hardeners are given in Table 4.2. Further details are available in technical sheets included in the thesis.

Table 4.2: Basic parameters of hardeners (25°C)

Parameter	H508	H500	H492
Viscosity [mPa.s]	7-11	200-350	> 15
Density [g/cm^3]	0.93-0.96	1.00-1.06	> 0.93

[1] The mechanical properties refer to a fully cured state and room temperature. Further details can be found in Appendix A.

Tables 4.3 - 4.5 store the specimens basic geometrical parameters. Point out that the groups of specimens experiencing the highest variability, L285/H500 and E455/H492, were essentially used in calibrating the generalized Leonov model.

Because tensile tests of E520/H492 epoxy matrix revealed more or less brittle behavior, recall Fig. 1.2(c), they were excluded from creep tests and therefore also from the calibration process outlined in the next two sections for L285 (Section 4.2.1) and E455 (Section 4.2.2) epoxy matrices, respectively.

Table 4.3: Epoxy resin L285 - geometry of specimens

Parameter (H508)	Width [mm]	Thickness [mm]	Cross-section area [mm^2]
Mean	5.04	2.76	13.90
Std. dev.	0.02	0.05	0.28
Parameter (H500)	Width [mm]	Thickness [mm]	Cross-section area [mm^2]
Mean	4.11	2.95	12.13
Std. dev.	0.28	0.14	0.98

Table 4.4: Epoxy resin E455/H492 - geometry of specimens

Parameter	Width [mm]	Thickness [mm]	Cross-section area [mm^2]
Mean	4.39	3.51	15.46
Std. dev.	0.38	0.35	1.90

Table 4.5: Epoxy resin E520/H492 - geometry of specimens

Parameter	Width [mm]	Thickness [mm]	Cross-section area [mm^2]
Mean	5.03	2.32	11.7
Std. dev.	0.04	0.05	0.30

4.2.1 L285 Havel epoxy resin

4.2.1.1 Tensile tests at different strain rates

The most straightforward calibration of the stress shift factor a_σ is to construct an Eyring plot (Tervoort, 1996; Valenta, 2003) assuming that at plastic yielding the plastic strain rate equals the total strain rate. The yield stress is then defined as a stress level, which remains constant at further straining. With reference to the Leonov model we recognize analogy with an elastic perfectly plastic von Mises material. Thus beyond the yield point the material behaves as a generalized Newton fluid

$$\boldsymbol{\sigma} = \mathbf{m}\sigma_m + 2\eta(\dot{E}_d)\dot{\boldsymbol{e}}_p = \mathbf{m}\sigma_m + 2\eta(\dot{E}_d)\dot{\boldsymbol{e}} \tag{4.13}$$

where the notation $\dot{\boldsymbol{e}} = \dfrac{\mathrm{d}\boldsymbol{e}}{\mathrm{d}t}$ was introduced for the sake of conciseness and $\dot{E}_d = \sqrt{2\dot{\boldsymbol{e}}^{\top}\mathbf{Q}\dot{\boldsymbol{e}}}$ is the rate of equivalent deviatoric strain. In simple tension and at plastic yielding $\sigma_x = f_y$ we get

$$\dot{\varepsilon}_v = 0, \quad \dot{E}_d = \sqrt{3}\dot{\varepsilon}_x, \quad J = \frac{1}{\sqrt{3}} f_y \tag{4.14}$$

With reference to Eq. (4.1) and realizing that $2\dot{e}_p = \dot{\gamma}_p$ is equivalent to $\dot{E}_d$ in plastic yielding and multidimensional space we may write

$$f_y = \tau_0\sqrt{3}\mathrm{arcsinh}(A\sqrt{3}\dot{\varepsilon}_x) \tag{4.15}$$

which for large values of $A\dot{E}_d$ simplifies as

$$f_y = \tau_0\sqrt{3}\ln(2A\sqrt{3}) + \tau_0\sqrt{3}\ln\dot{\varepsilon}_x \tag{4.16}$$

Equation (4.16) thus suggests that parameters of the Eyring flow model A, τ_0 can be found through a linear regression in the $f_y \times \dot{\varepsilon}_x$ diagram.

To that end, six specimens corresponding to L285/H508 epoxy matrix were loaded in the displacement controlled regime at a specific strain rate until failure using the MTS Alliance 30kN electromechanical testing machine equipment with 30kN load cell. The evolution of strain ε_x was measured using a clip on extensometer with an initial gauge length of 25 mm tightly mounted on the surface of the tested specimen, see Fig. 4.3(a). The corresponding stresses were derived by dividing the chamber force by the average cross-section area obtained from several measurements along the specimen length, see Table 4.3.

(a)

(b)

Figure 4.3: a) MTS Alliance 30kN electromechanical testing system, b) MTS Mini Bionix 858.02 testing system

Figure 4.4(a) shows the resulting stress-strain curves confirming a strong strain rate dependency and nonlinear viscous behavior over the whole range of the applied strain rates manifested by variation of both the initial shear stiffness and yield stress f_y. The latter quantity is defined as the maximum stress attained in the experiment. The corresponding Eyring plot is presented as a dashed line in Fig. 4.4(d) resulting in $\tau_0 = 1.7$MPa.

As already mentioned, we expected this value to be applicable in the definition of the shift factor a_σ when attempting to construct the shear compliance Master curve from standard creep tests performed at variable stress level. Point out that all creep experiments were performed for the L285/H500 epoxy matrix. It will be seen in the next Section 4.2.1.2 that replacing the original H508 hardener with H500 has a considerable impact on the mechanical behavior of the resulting material. This can be partially explained from the results of the tensile tests plotted in Fig. 4.4(b) for the L285/H500 material showing essentially a brittle response at higher strain rates. The Eyring plot constructed from two points only appears as a solid line in Fig. 4.4(d) and with $\tau_0 = 7.3$MPa significantly deviates from that of L285/H508 material.

It is, however, necessary to mention that the tensile tests for L285/E500 material were carried out not until the calibration process was completed exploiting purely creeps tests. Therefore, we may use these results just to compare the value of τ_0 derived from two different approaches. To finally appreciate the influence of the applied hardener, we plot all the results in one graph in Fig. 4.4(c).

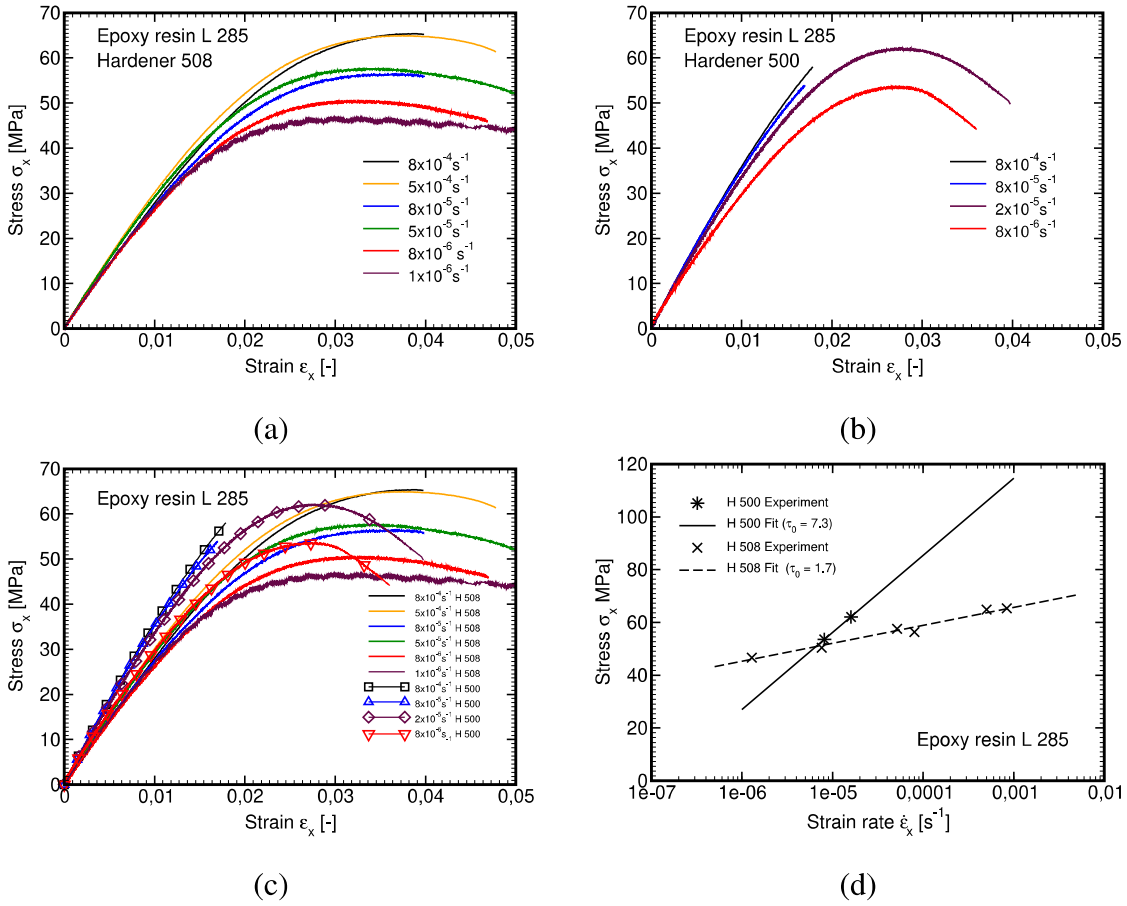

Figure 4.4: Tensile tests: a) Hardener 508, b) Hardener 500, c) All tests, d) Eyring plot

4.2.1.2 Creep tests at different stress levels

We open this section by assuming that the creep compliance function $J(t)$ can be well approximated by the Dirichlet series as

$$J(t) = \sum_{\mu=1}^{M} J_\mu \left[1 - \exp\left(-\frac{t}{\tau_\mu a_\sigma(t)}\right)\right] \tag{4.17}$$

where τ_μ are the selected retardation times. Note that the first term is typically assumed sufficiently small to represent in the limit $\tau \to 0$ an elastic solid. The compliances J_μ of the Kelvin units with nonlinear viscosities $\eta_\mu(\tau_{eq}) = \tau_\mu J_\mu a_\sigma(\tau_{eq})$ are derived by matching Eq. (4.17) with the experimentally derived Master curve.

To this end, we performed a series of creep tests at different stress levels. The creep experiments were performed for the L285/H500 material using the MTS Mini Bionix 858.02 testing system equipped with 1000N load cell, see Fig. 4.3(b). In the present study, four-

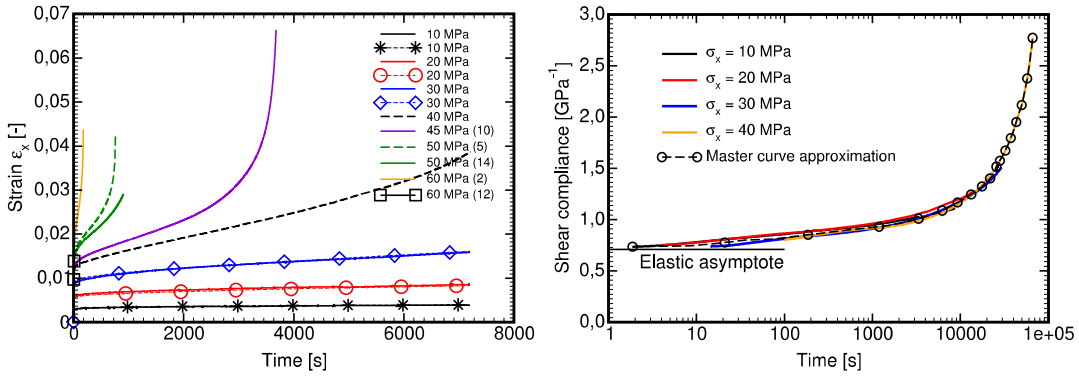

(a) (b)

Figure 4.5: L285/H500: a) Creep experiment, b) Master curve derived from experiments

teen specimens were loaded by a constant force corresponding to the required stress level evident in Fig. 4.5(a). The specimen preload was carried out at a constant loading speed of 500Ns^{-1}. The strains were then recorded for two hours using again the 25mm gauge length extensometer. Each test, except for tests at 40 and 45MPa, was run twice. As seen in Fig. 4.5(a), the results at low stress levels (10-30MPa) are comparable thus supporting the measurement credibility. The maximum stress level was suggested based on the maximum yield stress observed in the tensile tests, recall Section 4.2.1.1. It is evident that particularly at high stress levels the acquired measurements were greatly affected by the quality of the specimen, compare the curves for 50 and 60MPa. In addition, for stress levels exceeding 40MPa the tertiary creep can easily be identified. Exploiting these measurements would thus require a large strain formulation. Because of that, only the measurements up to 40MPa were adopted in further processing.

To construct the creep compliance function from the above tests we adopted the following steps:

1. Transform $t \times \varepsilon_x$ data into $t \times e_x$ plots where t is the time in [s] and e_x is the deviatoric normal strain provided by

$$e_x = \varepsilon_x - \frac{1}{3}\varepsilon_v = \varepsilon_x - \frac{\sigma_m}{K}, \quad \sigma_m = \frac{1}{3}\sigma_x, \quad K = \frac{E}{3(1-2\nu)} \tag{4.18}$$

where ε_v is the volumetric strain, σ_m is the mean stress, recall Eq. (4.6). The bulk modulus K is calculated from the elastic modulus E estimated from the elastic part of

the stress-strain curve when preloading the specimen to the desired stress level. The Poisson ratio ν is assumed to be known.

2. Transform the $t \times e_x$ curves into $t \times J$ data where J is the creep compliance in shear provided by
$$J = \frac{2e_x}{s_x}, \quad s_x = \sigma_x - \sigma_m = \frac{2}{3}\sigma_x \tag{4.19}$$

3. Shift the $t \times J$ data along the t-axis using the corresponding shift factor $a_\sigma(\tau_{eq})$. This is achieved by multiplying the original time by $a_\sigma(\tau_{eq})$. This way we arrive at the creep compliance curve (Master curve) we would obtain for a sufficiently low stress that produces viscoelastic response and is maintained for a long time.

As already mentioned in Section 4.2.1.1 we were unable to perform the 3rd step successfully owing to inadequacy of τ_0 derived originally for L285/H508 material. In the absence of tensile experiments for L285/H500 we thus adopted a different route and estimated τ_0 directly from creep tests. To this purpose, a simple optimization algorithm was implemented in MATLAB software. In particular, the search for τ_0 defining the shift factor a_σ via Eq. (4.3) amounts to finding a minimum of a single-variable function a_σ on a fixed interval. When formulating the objective function to be minimized we remember that the creep compliance functions, when shifted horizontally based on a given value of a_σ, partially overlap. In light of this the objective function was defined as the square root of sum of squares of deviations between the experimental data points, corresponding to consecutive load levels, over the current overlapping region. All curves were exploited at once. The minimization was performed with the help of the MATLAB function *fminbnd*.

The experimental data shifted on the basis of the derived parameter $\tau_0 = 5.3$MPa appear in Fig. 4.5(b) together with the resulting Master curve. It was confirmed that the elastic asymptote $J(t \to 0) = \frac{1}{G}$ approaches the inverse of the shear modulus G derived from the same Young modulus E and the Poisson ration ν as used in calculating the bulk modulus K in Eq. (4.18). Given the Master curve we may return to Eq. (4.17) to identify the compliances J_μ via, e.g., the least square method. They are listed in Table 4.6 assuming 9 Kelvin units and particular values of the retardation times τ_μ. The initial value of τ_1 =1E-5 was found sufficiently small. It should be mentioned that the approximation of creep compliance function using Eq. (4.17) is valid only for the time range specified by the retardation times.

Table 4.6: Parameters of Maxwell chain model - L285 epoxy resin

μ	τ_μ [s]	J_μ [MPa^{-1}]	θ_μ [MPa·s]	G_μ [MPa]
1	1E-05	7.047033×10^{-4}	9.655035×10^{-2}	4.915541×10^{1}
2	0.1	2.507001×10^{-5}	9.672027×10^{-1}	4.501054×10^{1}
3	1	2.469968×10^{-5}	$9.569420\times10^{+0}$	5.732147×10^{1}
4	10	3.377764×10^{-5}	$9.321383\times10^{+1}$	8.651850×10^{1}
5	100	5.703039×10^{-5}	$9.312438\times10^{+2}$	8.338651×10^{1}
6	1000	6.067732×10^{-5}	$9.073146\times10^{+3}$	1.324220×10^{2}
7	10000	6.906896×10^{-5}	$3.361408\times10^{+4}$	7.832536×10^{2}
8	100000	8.026744×10^{-4}	$1.565791\times10^{+5}$	1.294026×10^{2}
9	1000000	1.724650×10^{-2}	$7.293674\times10^{+5}$	5.256629×10^{1}

Application of Eqs. (4.11) and (4.12) calls for the transformation of creep compliance function (4.17) to relaxation function $R(t)$ given by

$$R(t) = \sum_{\mu=1}^{M} G_\mu \exp\left(-\frac{t}{\theta_\mu a_\sigma(t)}\right) \tag{4.20}$$

Typically, the Laplace transformation is employed to obtain the relaxation times θ_μ and the shear stiffnesses G_μ of the Maxwell units, see e.g. (Valenta et al., 2003). The results corresponding to creep compliance function at hand are stored in Table 4.6.

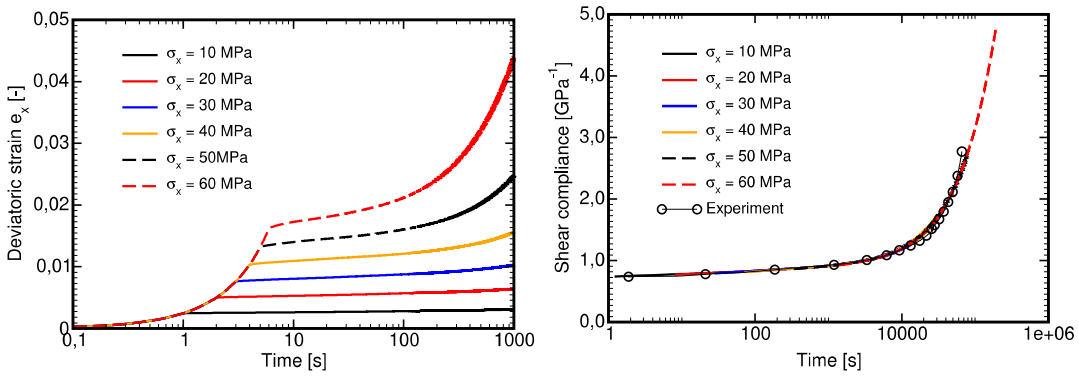

(a) (b)

Figure 4.6: a) Simulation of creep experiment, b) Master curve derived from simulations

To support applicability of the adopted generalized Leonov model we performed the creep tests numerically. The results are available in Fig. 4.6(a). The dashed lines correspond to stress levels not used in the experimental part. Figure 4.6(a) shows the numerically derived Master curve obtained by shifting the creep data with the help of the shift factor $a_\sigma(\tau_0)$ with $\tau_0 = 5.3$MPa found via the proposed optimization procedure. A relatively good match with experimental data is evident.

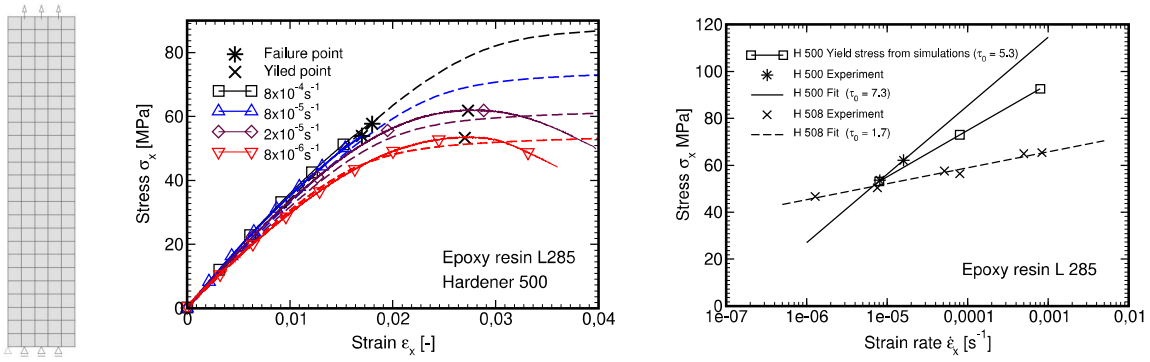

(a) (b) (c)

Figure 4.7: a) Finite element mesh, b) Simulation of tensile experiment, b) Eyring plot

For illustration we also reproduced the tensile test numerically. The analysis was performed in the plane stress regime using 4-node quadrilateral elements. Similarly to experimental measurements the analysis was carried out in the displacement control regime. The geometry of the computational model was selected such as to represent the part of the specimen covered by the extensometer. The resulting finite element mesh together with boundary and loading conditions is available in Fig. 4.7(a). The comparison with the experimental measurements is plotted in Fig. 4.7(b). A reasonable agreement is observed. A higher value of τ_0(H500-tension) $= 7.3$MPa in comparison to τ_0(H500-creep) $= 5.3$MPa used in simulations is reflected in a higher value of the yield stress f_y obtained experimentally. For illustration, the Eyring plots constructed from tensile tests (τ_0(tension)) and calculated numerically (τ_0(creep)) are compared in Fig. 4.7.

4.2.2 E455 epoxy resin

4.2.2.1 Tensile tests at different strain rates

Figure 4.8 shows the results of tensile tests performed at four different strain rates. These strains rates were selected such as to allow for a direct comparison with the tests carried out previously on L285/E508 material. As seen the assumed rate of loading was clearly to fast to arrive at the yield stress needed in the calibration of Eyring flow model. Therefore, similarly to L285/H500, these tests were not used any further and the necessary parameter τ_0 for the determination of the shift factor a_σ was obtained again in the process of constructing the Master curve from creep tests.

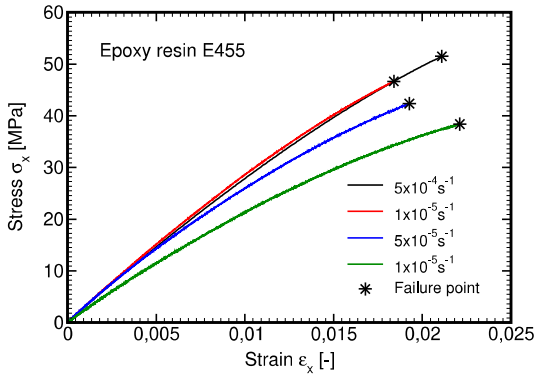

Figure 4.8: Tensile tests

4.2.2.2 Creep tests at different stress levels

The Master curves plotted in Figs. 4.9(b) and 4.10(b) were found following the same lines as described in Section 4.2.1.2. A higher brittleness in comparison to L285/H500 material supported by the tensile tests allowed for performing the creep tests at low stress levels only. The results of all usable creep tests (creep tests at stresses above 30MPa failed in a brittle manner) are displayed in Fig. 4.9. When compared to Fig. 4.5(a) the test reproducibility for E455/H492 material is not so obvious.

It is evident from experimental approximation of the Master curve in Fig. 4.9 that the creep tests cover a relatively short period of time. Extrapolation for longer times was thus achieved through a convenient definition of the creep compliance function given by

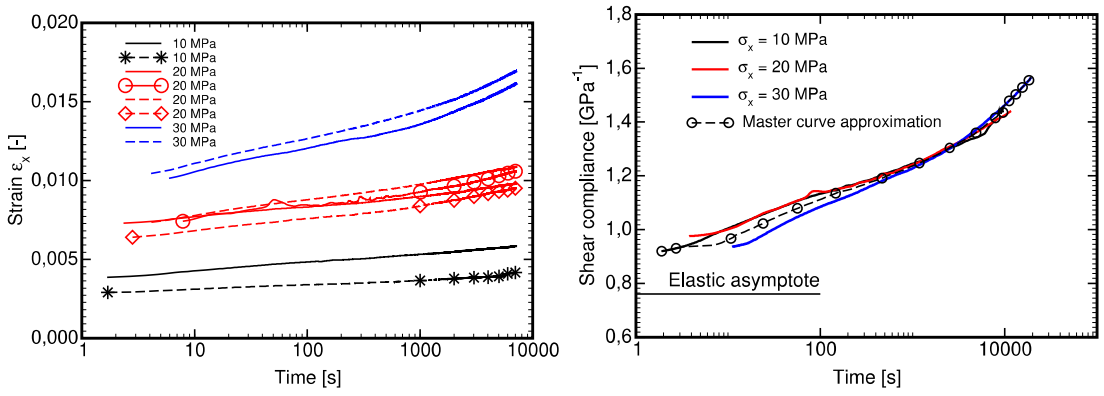

(a) (b)

Figure 4.9: E455/H492: a) Creep experiment, b) Master curve derived from experiments

Eq. (4.17). Similarly to the previous section a set of numerical creep tests was performed to compare the Dirichlet series approximation of the Master curve with the one obtained experimentally. The parameters of the fitted creep compliance function together with the used relaxation function found again through the Laplace transformation are presented in Table 4.7. Point out that the dashed lines in Fig. 4.10 correspond to stress levels not supported experimentally. While the theoretical representation of the Master curve for time range covered by experiments is reasonably close to the experimental one, its reliability beyond this range is questionable.

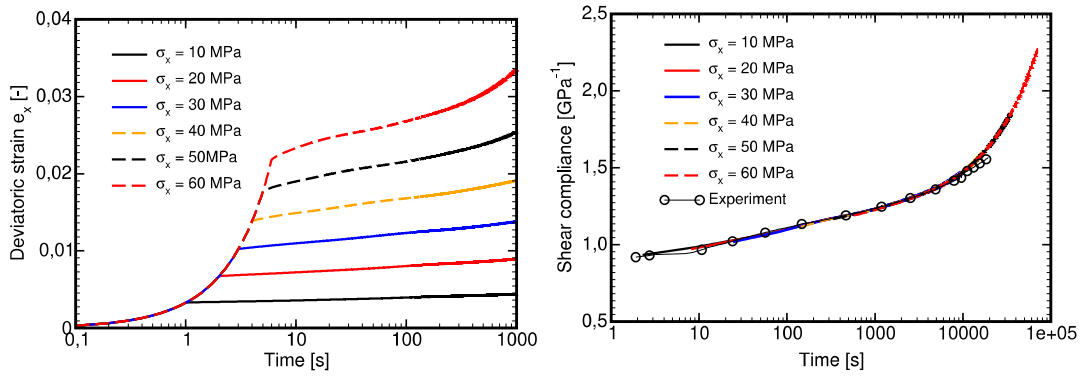

(a) (b)

Figure 4.10: a) Simulation of creep experiment, b) Master curve derived from simulations

Table 4.7: Parameters of Maxwell chain model - E455 epoxy resin

μ	τ_μ [s]	J_μ [MPa^{-1}]	θ_μ [MPa·s]	G_μ [MPa]
1	1E-05	7.623339×10^{-4}	8.633666×10^{-2}	1.802971×10^{2}
2	0.1	1.198067×10^{-4}	9.488823×10^{-1}	5.754286×10^{1}
3	1	4.778511×10^{-5}	$9.250901\times10^{+0}$	8.107289×10^{1}
4	10	7.467420×10^{-5}	$8.825322\times10^{+1}$	1.168796×10^{2}
5	100	1.333789×10^{-4}	$9.142418\times10^{+2}$	7.574899×10^{1}
6	1000	1.058116×10^{-4}	$8.920086\times10^{+3}$	9.495660×10^{1}
7	10000	1.355415×10^{-4}	$5.627064\times10^{+4}$	3.646023×10^{2}
8	100000	7.662422×10^{-4}	$2.679350\times10^{+5}$	2.327864×10^{2}
9	1000000	7.124439×10^{-3}	$1.275784\times10^{+5}$	1.078744×10^{2}

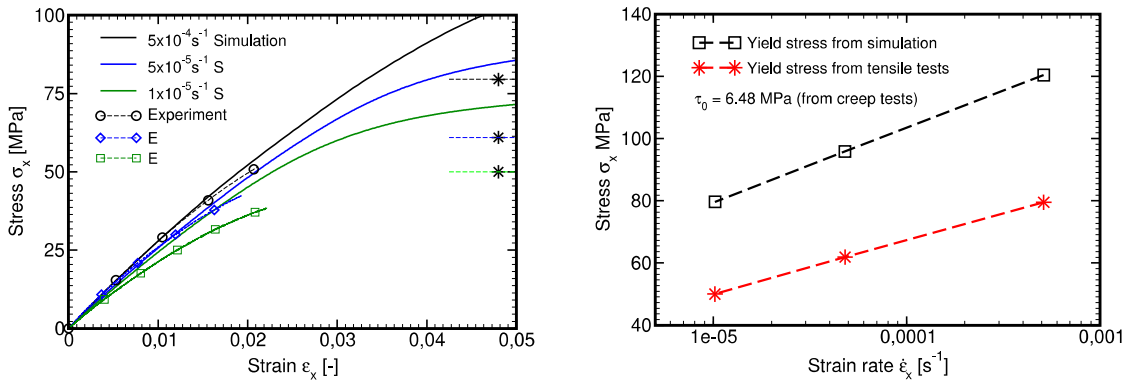

(a) (b)

Figure 4.11: a) Simulation of tensile experiment, b) Eyring plot

Difficulties in deriving the theoretical representation of the creep compliance function via Eq. (4.17) are further projected in numerical predictions of tensile tests plotted in Fig. 4.11(a). Clearly, the tensile tests suggest a considerably more compliant material than predicted numerically. If successful, the experiments would yield a significantly lower yield stress marked by the star symbol. The line passing through these points is the expected asymptote. The values are only approximate as they were obtained by an artificial prolongation of the tensile tests. The differences between the Eyring plot derived from simulations with

$\tau_0 = 6.48$MPa and the one potentially obtained from tensile tests are evident in Fig. 4.11(b) further highlighting a low credibility of the Dirichlet series approximation with the data in Table 4.7. On the contrary, the two lines are more or less parallel rendering, with reference to Eq. (4.16), a comparable value of τ_0 from both creep and tensile tests.

Despite previous discussions, the data in Table 4.7 were used in all simulations presented in Chapter 5. The interpretation of numerical predictions of the behavior of E455 matrix based composites should, however, be approached with caution.

Chapter 5

NONLINEAR VISCOELASTIC MODELING OF TEXTILE PLIES

With reference to the previous chapter, we limit our attention to material systems made of either unidirectional fiber or plane weave textile reinforcement bonded to either L285 or E455 polymer matrices. We begin with the estimation of the effective elastic properties both at the level of yarns and textile plies in Section 5.1. A detailed discussion on the nonlinear viscoelastic response at the level yarns is presented next in Section 5.2 with emphases on essential drawbacks associated with a standard implementation of the Mori-Tanaka method based on two-point averaging. The proposed two-step homogenization scheme needed in the simulation of nonlinear viscoelastic response of plane weave textile composites is finally discussed in Section 5.3. Because in standard multiscale FEM formulation the unidirectional composite is loaded by the strain increment developed in the corresponding finite element in the yarn we consider in all simulations the strain-control loading conditions only.

5.1 Elastic response on individual scales

This section serves to define basic computational models adopted on individual scales and to summarize the phase elastic properties. The elastic homogenization is then carried out to test implementation of these models and to identify basic differences of the studied material systems.

5.1.1 Computational models on individual scales

We start from the level of yarns and address the computational models we developed in our preceding papers (Valentová et al., 2020, 2021, 2022) for unidirectional fibrous composites. In particular, a sufficiently large test window was considered when extracting a representative image from a photograph of a real microstructure. Standard image analysis was then carried out to arrive at its binary counterpart, which in turn allowed us to estimate the volume fractions of individual phases. These images for carbon and basalt fiber based composites, which are considered in this study, are plotted in Fig. 5.1 rendering the volume fraction of carbon c_f^c and basalt c_f^b fibers equal to 0.56337 and 0.55808, respectively.

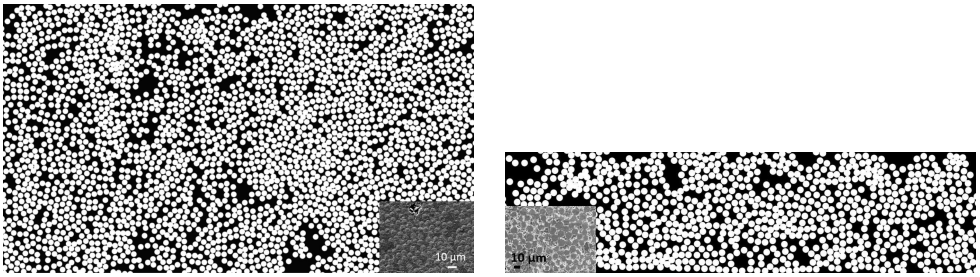

(a) (b)

Figure 5.1: Cross-sections of examined fibrous composites. a) Carbon fiber composite, b) Basalt fiber composite

Both images clearly suggest a random nature of the distribution of fibers in the transverse cross-section. A detailed study on similar microstructures, see e.g. (Zeman and Šejnoha, 2001; Zeman, 2003; Zeman and Šejnoha, 2007; Šejnoha and Zeman, 2013), revealed that such microstructures can be treated as statistically uniform thus promoting the application of classical micromechanical models such as the Mori-Tanaka method to estimate the macroscopic response, recall Section 3.2. However, when adopting the first-order homogenization presented in Section 3.1 the concept of statistically equivalent unit cell (SEPUC) (Zeman, 2003; Zeman and Šejnoha, 2007) is worth considering. On the contrary, it has also been suggested that for systems with a sufficiently large number of fibers exceeding 50% of their volume fraction the periodic hexagonal array (PHA) model (Teplý and Dvorak, 1988) appears as a suitable approximation. In light of the desired study that compares the MT and FEM based predictions of the macroscopic response, the use of PHA model in FEM simulations is further supported by the fact that for transversely isotropic phases, which is the present case, the MT method and PHA model yield the same effective elastic response being also transversely isotropic. While the MT method keeps this property even beyond elasticity, the PHA model may yield the overall behavior orthotropic (Valentová et al., 2020). This is rather intuitive given the geometry of the PHA model plotted together with periodic finite element mesh for the carbon phase in Fig. 5.2 for illustration. Although used in all simulations presented in Sections 5.2.1 and 5.2.2, its reliability in the scope of nonlinear viscoelastic response will be eventually tested in Section 5.2.3 on ensemble of computational models of a variable complexity generated as random cuts from the large images in Fig. 5.1.

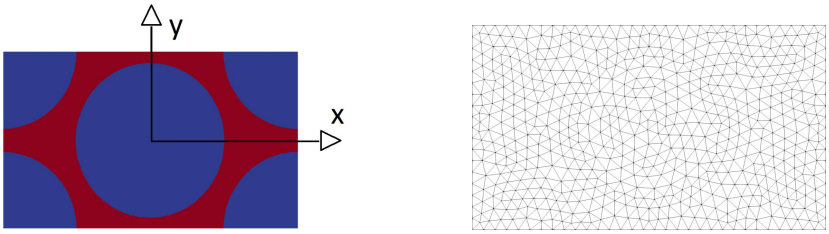

(a) (b)

Figure 5.2: PHA model: a) Geometry, b) Finite element mesh

Random or imperfect mesostructures with imperfections caused by the manufacturing process can also be encountered at the level of textile plies (Lomov et al., 2003; Šejnoha and Zeman, 2008; Vorel and Šejnoha, 2009; Vorel et al., 2015). To treat such imperfections is, however, a relatively complex task and goes beyond the present scope. Instead, we accept a considerably more simple problem and consider a single ply periodic unit cell (PUC) of a plain weave textile composite. The geometrical details including the finite element mesh are evident in Fig. 5.3.

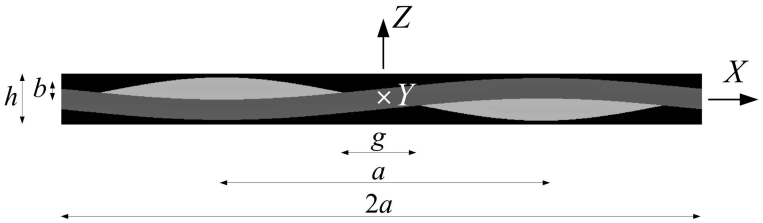

a)

(b) (c)

Figure 5.3: Example of periodic unit cell of a single ply textile composite: a) Basic geometrical data, b) Fiber tows, c) Finite element mesh

The basic geometrical data in Fig. 5.3a are taken from literature (Šejnoha and Zeman, 2013) and for the two material systems are summarized in Table 5.1 for the sake of completeness.

Table 5.1: Geometrical parameters of periodic unit cell

Parameter [μm]		Basalt	Carbon
Yarn period	$(2a)$	4072	1726
Yarn width	(b)	140	87
Inter-yarn gap	(g)	490	312
Ply height	(h)	314	183

Point out that the nonlinear viscoelastic analysis at the level of textile plies calls for the application of a two-scale computational scheme. Implementation of the MT method as a stress updater providing increments of effective stresses and instantaneous homogenized properties for a given time increment at each integration point of the yarn finite element is one of the principal thesis objectives independent of the PUC complexity. Thus this approach can easily by exploited once more credible PUCs are at hand.

5.1.2 Elastic properties of individual phases

Calibration of the material models describing the response of L285 and E455 polymer matrices has been presented in Section 4.2. Recall that the initial elastic response was estimated from both the tensile tests performed at the highest strain rate and slopes of the initial run-up of creep tests. The corresponding elastic shear moduli used in all presented simulations are provided by

$$G_m^{\mathrm{el}} = \sum_{\mu=1}^{N} G_\mu \tag{5.1}$$

where subscript m stands for the matrix. The shear stiffnesses G_μ of the Maxwell chain model are listed in Tables 4.6 and 4.7 for L285 and E455 matrices, respectively. The specific values of G_m^{el} are stored in Table 5.3. It is also worth mentioning that in all simulations the bulk modulus K_m^{el} is kept constant and is derived from G_m^{el} as

$$K_m^{\mathrm{el}} = \frac{2G_m^{\mathrm{el}}(1+\nu_m)}{3(1-2\nu_m)} \tag{5.2}$$

assuming the initial value of the Poisson number ν_m equal to 0.34 for both matrices. The actual value of ν_m is then adjusted based on the evolution of $G_m^{\rm vp}$ by replacing $G_m^{\rm el}$ by $G_m^{\rm vp}$ in Eq. (5.2).

The properties of carbon fibers in Table 5.3 were taken from literature (Šejnoha and Zeman, 2013), while the elastic Young moduli of the basalt fibers were estimated from nanoindentation. To that end, a specimen of basalt fiber based composite was embedded into an epoxy resin and left for 24 hours to harden in a cylindrical mold (25 mm in diameter). Approximately a 15 mm thick part of the sample was separated using a diamond cut-off wheel. To ensure an adequate surface roughness, the investigated sample was ground on an MD-Piano plate using 1200, 2000 and 4000 grain cm^{-2} grid and water as a lubricant under 5 N force. Consequently, a water based DP-Suspension containing 3 and 1 μm poly-crystalline diamonds on MD-Dur and MD-Nap cloths, respectively, was used for fine polishing. An MD-Chem cloth combined with the water-based DP-Suspension containing 0.25 μm and 0.1 μm diamond particles was selected for final polishing. In such a way, two surfaces for the measuring of longitudinal (Fig. 5.4) and transverse (Fig. 5.5) properties of the basalt fiber were prepared. Cutting the specimen in the direction normal to the fibers resulted in the average root mean square roughness R_q = 95.08 nm, whereas in case of cuts along the longitudinal direction an increase of the average root mean square roughness R_q = 300.75 nm was observed owing to the cleavage of fibers during preparation.

The measurements were carried out analogously for both longitudinal and transverse directions starting with scanning the composite surfaces with an in-build scanning probe microscopy (SPM) (Figs. 5.4a and Figs. 5.5a) to identify location of individual indents. These are seen for the fibers in Figs. 5.4b and 5.5b. The indented surfaces are evident in Figs. 5.4c and 5.5c. Each phase was subjected to a different loading function. Separation of indents ensured no interaction of individual indents. The indented surfaces were finally scanned again to check the measurements accuracy.

The load-controlled quasi-static indentation was performed with the load function consisting of "loading" and "unloading" segments lasting 5 seconds each with an in-between 300 seconds segment of "holding" time. The maximum applied force of 2500 μN was used. This procedure was applied to several positions on the sample. The resulting reduced moduli, corresponding to longitudinal and transverse indentations into the fibers, were derived

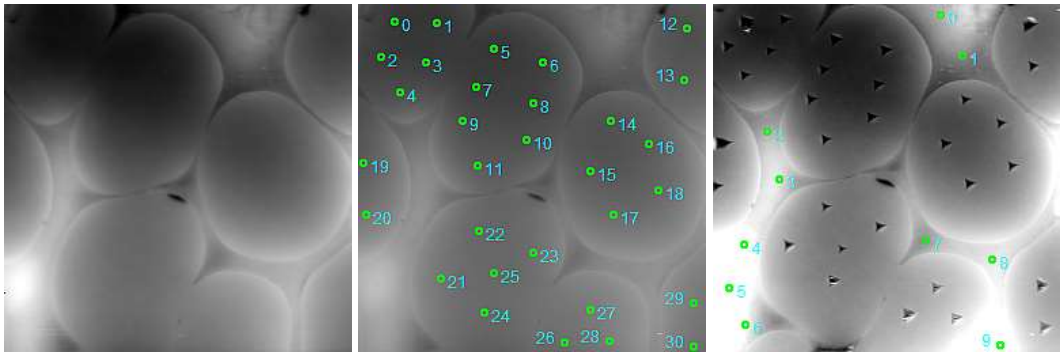

(a) (b) (c)

Figure 5.4: Indentation steps in longitudinal direction

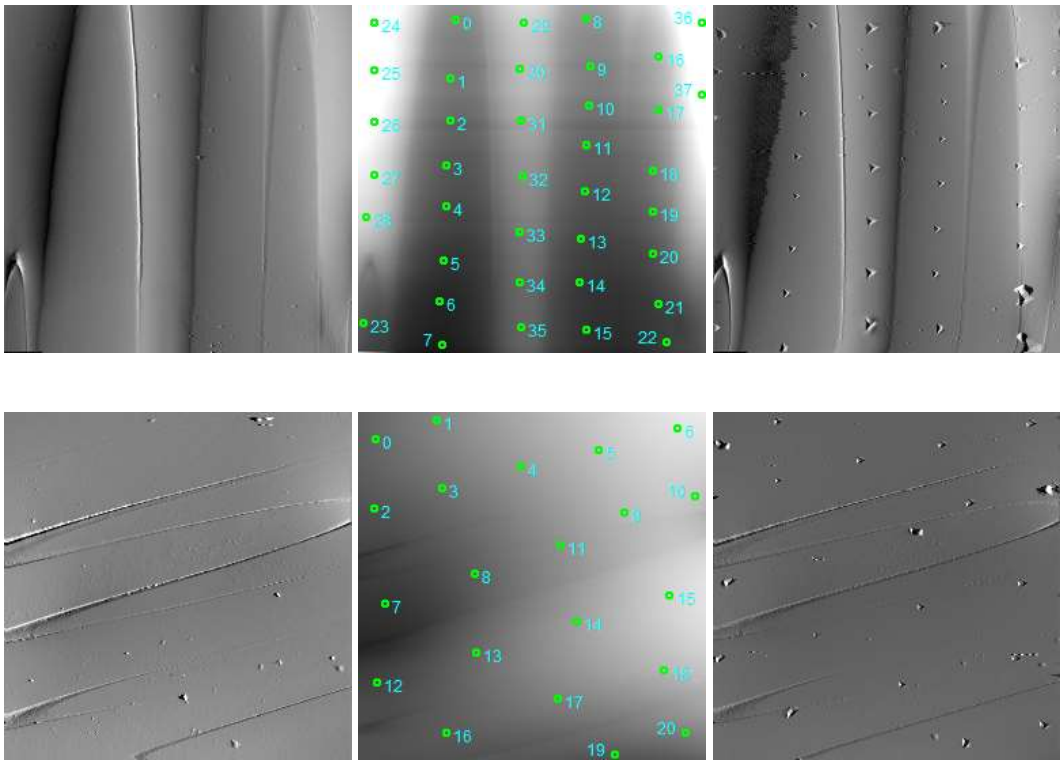

(a) (b) (c)

Figure 5.5: Indentation steps in transverse direction

from unloading part of the indentation curve. Next, the required Young moduli were calculated based on the contact mechanics of colliding solid bodies (Hertz, 1882; Oliver and Phar, 2004) assuming the Poisson ratio $\nu = 0.24$ for all phases and a diamond tip with material parameters E= 1140 GPa and $\nu = 0.07$. Taking into account all indents gave the average values of the Young modulus equal to 69.68 GPa and 64.82 GPa for the longitudinal and transverse

Table 5.2: Indentation results of basalt fibers

Position	**Red. mod.** E_r [GPa]	**Young's mod.** E [GPa]	**Hardness** H [GPa]	**Indentation depth** h_c [nm]
Longitudinal direction				
P127_2	67.81 ± 8.09	67.72 ± 7.68	5.27 ± 0.56	191.92 ± 6.55
P128_1	75.95 ± 6.55	75.66 ± 6.21	5.95 ± 0.88	106.09 ± 8.91
P128_2	76.85 ± 7.75	76.63 ± 7.35	5.71 ± 0.76	108.33 ± 7.98
P130_1	66.17 ± 10.44	66.08 ± 9.93	5.49 ± 0.75	161.55 ± 12.22
P130_2	71.76 ± 7.30	71.15 ± 6.92	5.79 ± 0.38	155.99 ± 5.62
P130_3	61.12 ± 6.68	60.85 ± 6.33	5.28 ± 0.74	239.19 ± 18.71
average	69.94 ± 7.80	69.68 ± 7.40	5.58 ± 0.68	160.51 ± 10.00
Transverse direction				
P120_1	74.09 ± 6.22	73.65 ± 6.22	5.88 ± 1.17	107.60 ± 11.80
P121_2	75.98 ± 3.79	75.69 ± 3.58	5.94 ± 0.54	105.58 ± 5.57
P121_3	57.31 ± 3.58	56.85 ± 3.38	5.00 ± 0.55	116.33 ± 7.25
P122_1	55.34 ± 10.55	54.80 ± 10.03	4.45 ± 1.16	126.64 ± 17.08
P122_2	68.77 ± 8.09	68.65 ± 7.68	5.15 ± 0.54	114.39 ± 6.80
P124_1	59.61 ± 11.70	59.26 ± 9.44	5.29 ± 1.22	117.95 ± 15.13
average	65.18 ± 7.32	64.82 ± 7.03	5.29 ± 1.19	114.52 ± 14.15

fiber directions, respectively. Further details including basic statistics are available in Tables 5.2 and 5.3. As seen in Table 5.3, the matrix is considered isotropic whereas fibers are taken as transversely isotropic.

5.1.3 Homogenized elastic properties on individual scales

The results of elastic homogenization on both scales are presented in the following two sections. On microscale (level of yarns) the first order homogenization using FEM as well as the MT method are employed and compared. On mesoscale (level of textile plies) the MT method is used to get the yarn effective properties, whereas the ply effective properties are derived solely via FEM based homogenization. For application of the MT method on both

Table 5.3: Phase elastic properties. Elastic moduli are in [GPa]

fibers	E_{L}	E_{T}	G_{L}	ν_{L}	ν_{T}
Carbon	294	13	12	0.24	0.30
Basalt	69.7	64.8	28.1	0.40	0.24
matrix	G^{el}	K^{el}			
L285	1.42	3.96			
E455	1.31	3.66			

scales the interested reader is referred to (Vorel and Šejnoha, 2009).

5.1.3.1 Homogenized elastic properties at the level of yarns

The MT estimate of the effective stiffness matrix follows from Eq. (3.25). In the framework of first-order homogenization the effective elastic properties are derived from Eq. (3.15) following the procedure described in the last paragraph of Section 3.1. Recall, that plane-strain conditions are enforced so that the out-of-plane shear stresses cannot be delivered by FEM and, therefore, are not displayed in Table 5.4. The elastic moduli and the longitudinal Poisson ratio ν_L were extracted from the reduced stiffness matrix in Eq. (3.1) using the relations (3.2).

Table 5.4: Yarn effective properties - comparing FEM and MT method based homogenization. Elastic moduli are in [GPa]

Composite	$E_{\mathrm{L}}^{\mathrm{FEM}}$	$E_{\mathrm{L}}^{\mathrm{MT}}$	$E_{\mathrm{T}}^{\mathrm{FEM}}$	$E_{\mathrm{T}}^{\mathrm{MT}}$	$G_{\mathrm{T}}^{\mathrm{FEM}}$	$G_{\mathrm{T}}^{\mathrm{MT}}$	$\nu_{\mathrm{L}}^{\mathrm{FEM}}$	$\nu_{\mathrm{L}}^{\mathrm{MT}}$
L285-Carbon	167.3	167.3	7.5	7.4	2.7	2.6	0.28	0.28
L285-Basalt	40.6	40.6	11.7	10.8	4.1	3.8	0.38	0.38
E455-Carbon	167.2	167.2	7.2	7.1	2.5	2.5	0.28	0.28
E455-Basalt	40.4	40.4	10.9	10.1	3.8	3.6	0.38	0.38

As expected, a perfect match is observed for properties along the longitudinal (L) direction while a small difference is evident for properties in the transverse (T) direction. These differences are more pronounced for basalt fibers, which can be attributed to a significant

mismatch of elastic moduli of the two phases, recall Table 5.3. These results will be further supported by stress-strain diagrams plotted in Section 5.2.

5.1.3.2 Homogenized elastic properties at the level of textile ply

The effective elastic properties at the level of textile ply are estimated analogously to the previous section by running a 3D FEM analysis of PUC in Fig. 5.3. What is useful to mention is the way the individual components of the 6×6 elastic compliance matrix $\mathbf{M}$ are treated in Eq. (5.3)

$$\begin{Bmatrix} \varepsilon_{XX} \\ \varepsilon_{YY} \\ \varepsilon_{ZZ} \\ \gamma_{YZ} \\ \gamma_{ZX} \\ \gamma_{XY} \end{Bmatrix} = \begin{bmatrix} \frac{1}{E_{XX}} & -\frac{\nu_{YX}}{E_{YY}} & -\frac{\nu_{ZX}}{E_{ZZ}} & 0 & 0 & 0 \\ -\frac{\nu_{XY}}{E_{XX}} & \frac{1}{E_{YY}} & -\frac{\nu_{ZX}}{E_{ZZ}} & 0 & 0 & 0 \\ -\frac{\nu_{XZ}}{E_{XX}} & -\frac{\nu_{YZ}}{E_{YY}} & \frac{1}{E_{ZZ}} & 0 & 0 & 0 \\ 0 & 0 & 0 & \frac{1}{G_{YZ}} & 0 & 0 \\ 0 & 0 & 0 & 0 & \frac{1}{G_{XZ}} & 0 \\ 0 & 0 & 0 & 0 & 0 & \frac{1}{G_{XY}} \end{bmatrix} \begin{Bmatrix} \sigma_{XX} \\ \sigma_{YY} \\ \sigma_{ZZ} \\ \tau_{YZ} \\ \tau_{XZ} \\ \tau_{XY} \end{Bmatrix} = \mathbf{M}\boldsymbol{\sigma} \tag{5.3}$$

With this particular definition of $\mathbf{M}$, the Poisson ratios are provided, e.g., by

$$\nu_{XY} = -\frac{\varepsilon_{XX}}{\varepsilon_{YY}} = -\frac{M_{YX}}{M_{XX}}, \qquad \nu_{YX} = -\frac{\varepsilon_{YY}}{\varepsilon_{XX}} = -\frac{M_{XY}}{M_{YY}} \tag{5.4}$$

Table 5.5: Textile ply effective properties from FEM homogenization.
Elastic moduli are in [GPa] ($\nu_{XY} = \nu_{YX}, \nu_{XZ} = \nu_{YZ}, \nu_{ZX} = \nu_{ZY}$)

Composite	E_{XX}	E_{YY}	E_{ZZ}	G_{YZ}	G_{XZ}	G_{XY}	ν_{XY}	ν_{XZ}	ν_{ZY}
L285-Carbon	30.0	30.0	6.6	2.0	2.0	2.5	0.06	0.44	0.10
L285-Basalt	12.4	12.4	6.6	2.1	2.1	2.6	0.19	0.41	0.22
E455-Carbon	29.1	29.1	6.2	1.9	1.9	2.3	0.06	0.44	0.09
E455-Basalt	12.0	12.0	6.2	2.0	2.0	2.4	0.19	0.41	0.21

The resulting effective properties are summarized in Table 5.5 confirming the macroscopic orthotropy of the balanced plane weave composites, which make no difference be-

tween the warp and weft directions. As the elastic properties of the two polymer matrices are comparable, recall Table 5.3, the macroscopic elastic response of the L285/carbon and E455/carbon systems can be expected comparable. The same holds for the L285/basalt and E455/basalt systems as evident from Table 5.5. However, the rheological response of the L285 polymer matrix vastly differs from that of the E455 matrix, which will become evident in the following section when addressing the mechanical response beyond elasticity.

5.2 Nonlinear viscoelastic modeling of unidirectional fibrous composites

The results of the nonlinear viscoelastic analysis performed at the level of yarns are presented aiming at principal drawbacks of the original formulation of the MT method, recall Section 3.2, and its potential improvement. The matter concerning the definition of a reliable computational model for random composite in the framework of first-order homogenization is also addressed.

5.2.1 Comparing FEM simulation and standard implementation of MT method

A considerable difference between the MT and FEM predictions has already been observed in (Valentová et al., 2020) for purely viscoelastic behavior of the polymer matrix. This issue is revisited here in light of nonlinear viscoelasticity. To keep formal similarity with Section 4.2 the prescribed macroscopic strain rate is considered. For simplicity, only the response in transverse shear is examined. In particular, the macroscopic engineering shear strain rate $\dot{E}_{xy} = 0.001\text{s}^{-1}$ is prescribed in all simulations, recall the assumed coordinate system in Fig. 5.2. Again, all four material systems discussed already in Section 5.1.2 are analyzed.

To introduce the subject we first recall the differences in the rheological behavior of the two polymer matrices by plotting the Dirichlet approximation of their master-curves in Fig. 5.6a. In order to verify the implementation of the generalized Leonov model we also compare in Fig. 5.6b the response generated by FEM simulation using the PHA model and the MT method. As seen, for purely isotropic material the predictions are identical. Applicability of the model to address the rate effect observed experimentally is also confirmed.

The composite response is shown in Fig. 5.7 for individual material systems. A con-

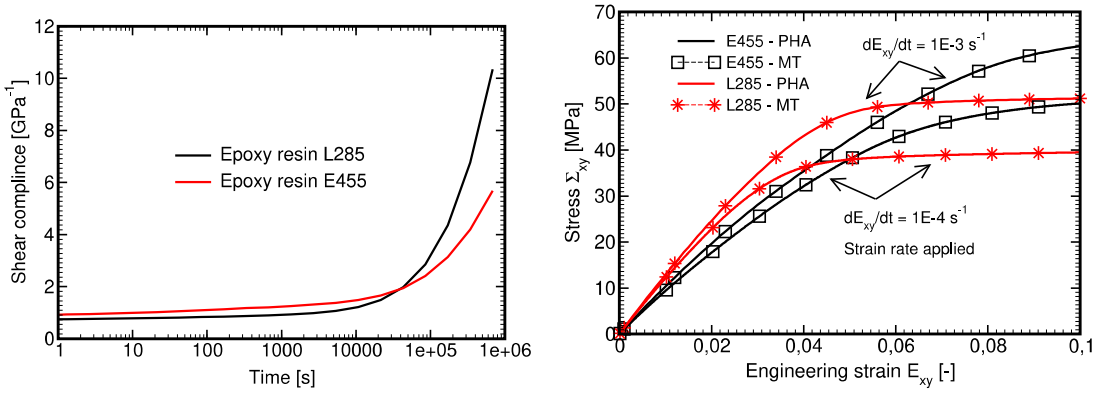

(a) (b)

Figure 5.6: Nonlinear viscoelastic response of L285 and E455 polymer matrices: a) Approximation of master-curve via Dirichlet series, b) Stress-strain diagrams for two different strain rates provided by FE and MT methods

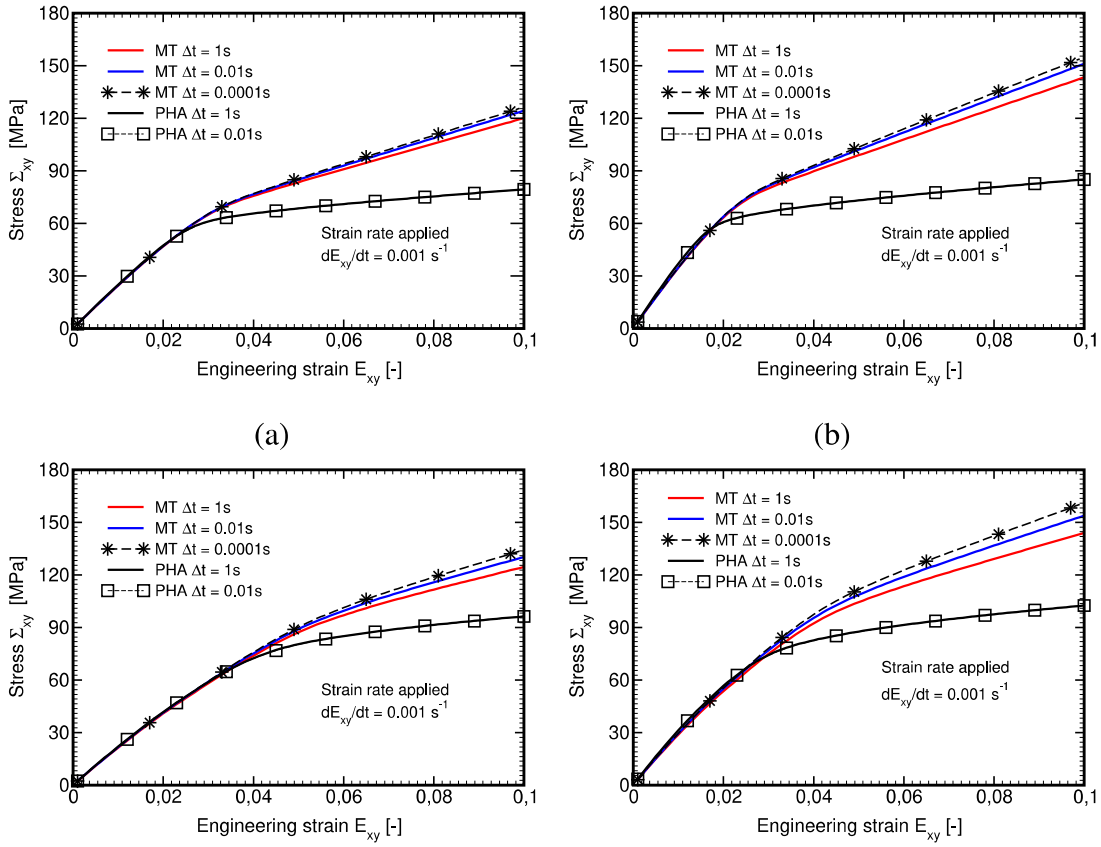

(a) (b)

(c) (d)

Figure 5.7: Time step effect of macroscopic response (comparing FEM and MT): a) L285-Carbon, b) L285-Basalt, c) E455-Carbon, d) E455-Basalt

siderably stiffer behavior predicted by the original formulation of the MT method is evident. What is also clear is the dependence of the MT method based macroscopic predictions on the adopted time step Δt, the result not observed for FEM simulations. This dependence is more evident for basalt fiber based composites having a larger mismatch in shear elastic moduli between the fiber and the matrix phase when compared to carbon fiber based composite, where the shear stiffness of both phases is of the same order.

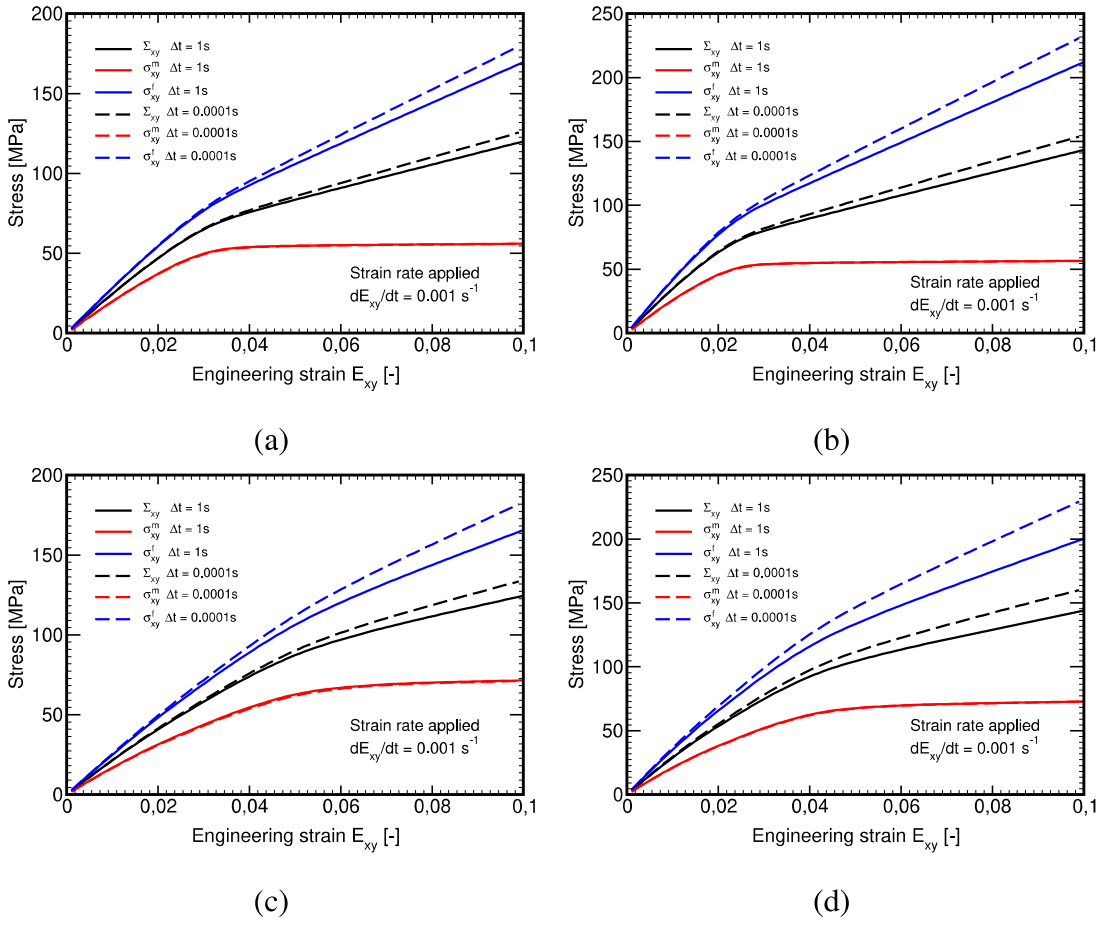

Figure 5.8: Time step effect on local response (MT): a) L285-Carbon, b) L285-Basalt, c) E455-Carbon, d) E455-Basalt

Therefore, it can be expected that the time step dependence of the macroscopic response will be attributed merely to the fiber phase. This is manifested in Fig. 5.8 where the matrix phase response is clearly shown to be controlled by the Leonov constitutive model whereas the transition of the stress into the fiber phase might be affected by the time dependence of

the instantaneous matrix phase Poisson ratio.

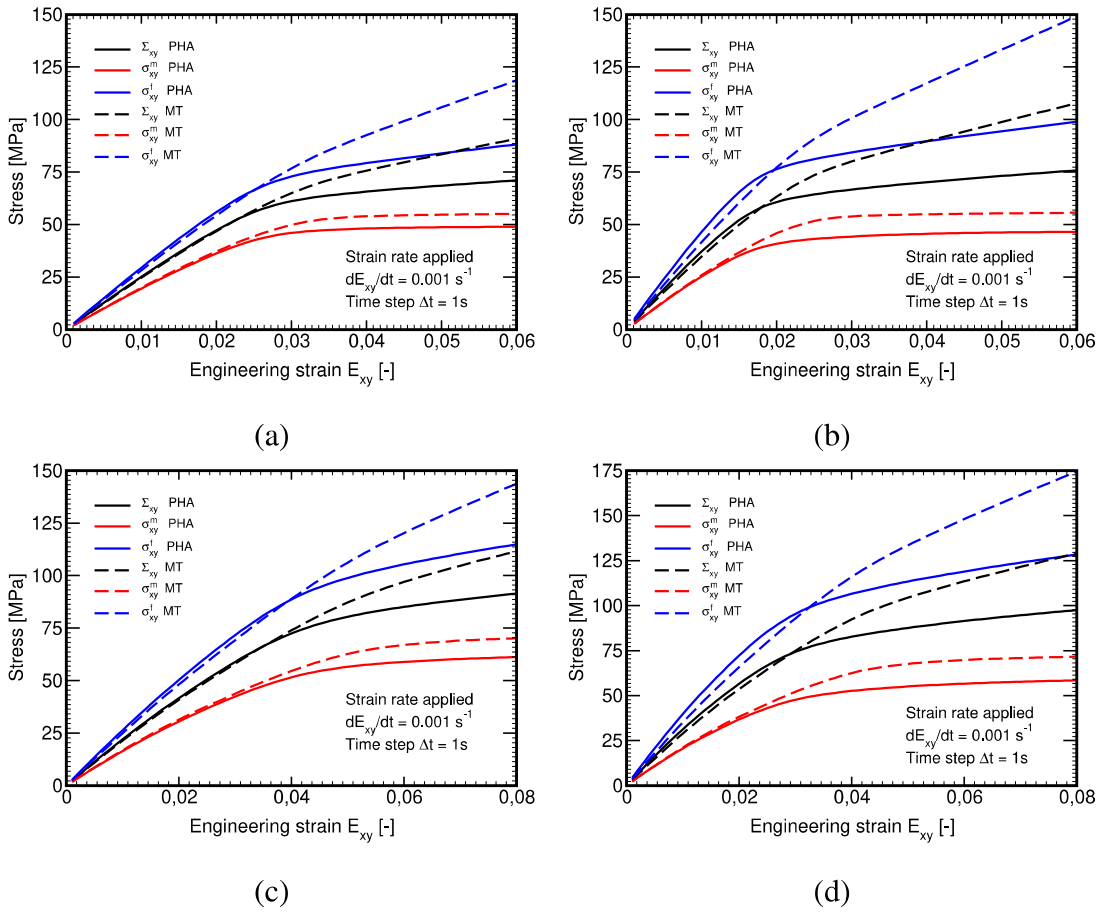

Figure 5.9: Local response (comparing FEM and MT): a) L285-Carbon, b) L285-Basalt, c) E455-Carbon, d) E455-Basalt

An inadequate transition of the macroscopic stress into the fiber phase is also evident in Fig. 5.9 showing much stronger deviation of the MT predictions from the FEM results for the fiber phase, while for the matrix phase the stress mismatch is not so significant, again because of the elastic-perfectly plastic character of the Leonov model with the rate dependent yield stress, recall Chapter 4. This observation will be exploited in the next section, where we attempt to improve the macroscopic prediction of the MT method by adjusting the local constitutive law of the fiber phase.

5.2.2 Reformulation of MT method

Unlike standard formulation of Dvorak's transformation field analysis that considers constant localization tensors and transformation influence functions based on elasticity solution, we assumed in the formulation presented in Section 3.2 a time evolution of the instantaneous shear modulus. However, the results presented in the previous section show that this modification still does not present satisfactory results when compared to the results provided by FEM in combination with the PHA model. In the following text we propose potential modifications to improve the MT predictions.

The modified formulation grounds on the fact, recall the last paragraph in the previous section, that the stiff average response is attributed to the way the stresses are localized into the fiber phase as the matrix response is assumed to be controlled solely by the constitutive law. In FEM simulation the stress transfer between individual phases is most probably affected by the formation of shear bands in the matrix. We attempt to address this issue by suitably modifying the local constitutive model of the fiber phase by replacing the elastic stiffness matrix $\mathbf{L}_f$ in Eq. (3.25) via a properly adjusted instantaneous stiffness matrix $\tilde{\mathbf{L}}_f$ so that

$$\Delta\boldsymbol{\sigma}_f = \tilde{\mathbf{L}}_f \Delta\boldsymbol{\varepsilon}_f. \tag{5.5}$$

Being inspired by (Šejnoha et al., 2004; Valenta et al., 2010; Valenta and Šejnoha, 2012) we suggest to reduce the stresses taken by the fibers through a damage like parameter ω and write the fiber stress increment as

$$\Delta\tilde{\boldsymbol{\sigma}}_f = \mathbf{L}_f \Delta\boldsymbol{\varepsilon}_f, \tag{5.6}$$

$$\Delta s_{f,ij} = (1-\omega)(\Delta\tilde{\sigma}_{f,ij} - \delta_{ij}\Delta\tilde{\sigma}_{f,m}), \quad \Delta\tilde{\sigma}_{f,m} = \frac{1}{3}\Delta\tilde{\sigma}_{f,ii}, \tag{5.7}$$

$$\Delta\sigma_{f,ij} = \Delta s_{f,ij} + \delta_{ij}\Delta\tilde{\sigma}_{f,m}, \tag{5.8}$$

where $\Delta\boldsymbol{s}_f, \Delta\tilde{\sigma}_{f,m}$ represent the deviatoric and mean components of the fiber stress increment $\Delta\boldsymbol{\sigma}_f$. The tensorial notation in Eqs. (5.7) and (5.8) is adopted just for the sake of convenience. Point out that the stress reduction applies to the deviatoric stress components only.

Two particular formulations of the damage parameter ω are investigated.

5.2.2.1 Formulation based on stress

With reference to the definition of the Eyring flow model and the study performed in (Valentová et al., 2021) we first consider a stress-based evolution of the damage parameter in the form

$$\omega = N\left[1 - \left(\frac{\tau_{eq}^t - T}{\tau_0}/\sinh(\frac{\tau_{eq}^t - T}{\tau_0})\right)\right]^M, \tag{5.9}$$

where M, N, T are the model parameters. Recall that τ_0 is the Eyring flow model parameter (4.1), τ_{eq} is the equivalent deviatoric stress (4.4) and the superscript t links τ_{eq} with the current time.

Figure 5.10 shows how these parameters control the evolution of ω. While parameter M adjusts the rate of evolution of ω with τ_{eq}, the other two parameters N, T merely shift the damage curve horizontally and vertically. Thus N controls the minimum stress that the fibers may take and T serves to delay the onset of damage evolution. Note that these two parameters are subject to some limitations, particularly

$$N = \langle 0, 1\rangle, \tag{5.10}$$

and

$$\text{if } \tau_{eq} < T \text{ then } \omega = 0, \tag{5.11}$$

$$\text{if } \tau_{eq} > T \text{ then } \omega \text{ follows from Eq. (5.9).} \tag{5.12}$$

As seen in Fig. 5.11 that with a properly adjusted parameters M, N, T the new formulation may provide almost a perfect match of the MT and PHA model based predictions for a given strain rate and loading direction. Localization of the macroscopic shear stress into individual phases is evident in Fig. 5.12. Comparing these results with those presented in Fig. 5.9 clearly suggests that the damage parameter ω influences, as expected, the fiber stress only with no effect on the matrix stress.

Intuitively, some drawbacks of this formulation can be expected. Similarly to standard damage models the damage parameter ω is only allow to grow. But the damage is turned off once reduction of ω is experienced thus resuming the elastic behavior similarly to elastic unloading in plasticity. Therefore, there is no adjustment of the fiber stresses when for example relaxation response is studied as is shown in Fig. 5.13. While this approach appears

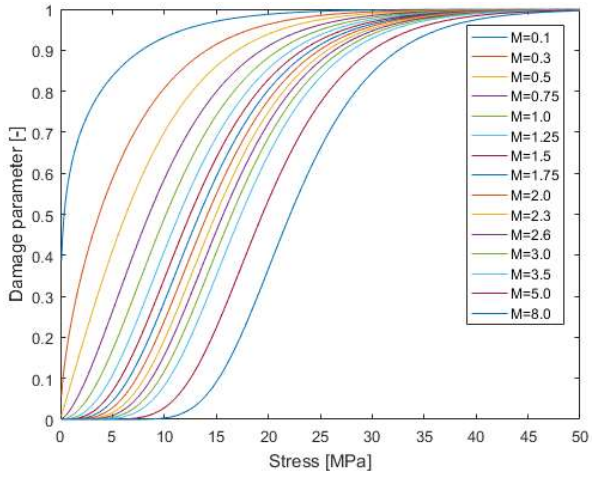

(a)

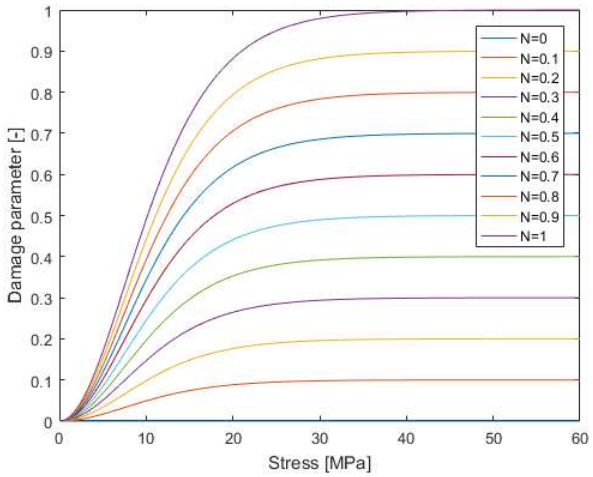

(b)

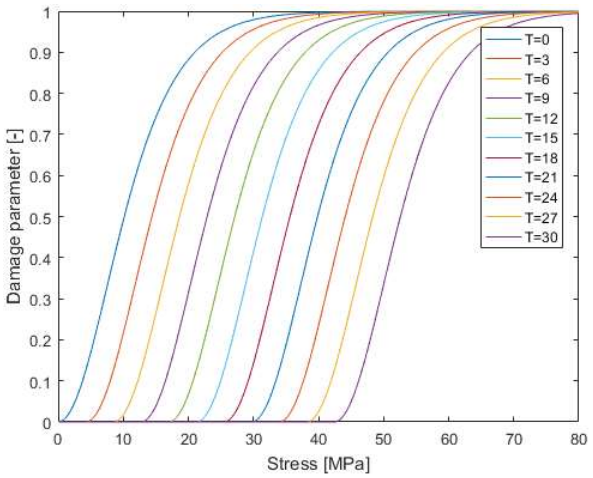

(c)

Figure 5.10: Influence of parameters M, N in describing the evolution of ω according to Eq. (5.9): a) Influence of parameter M, N=1, T=0; b) Influence of parameter N, M=1, T=0; c) Influence of parameter T, M=N=1 (results are replotted from (Valentová et al., 2021))

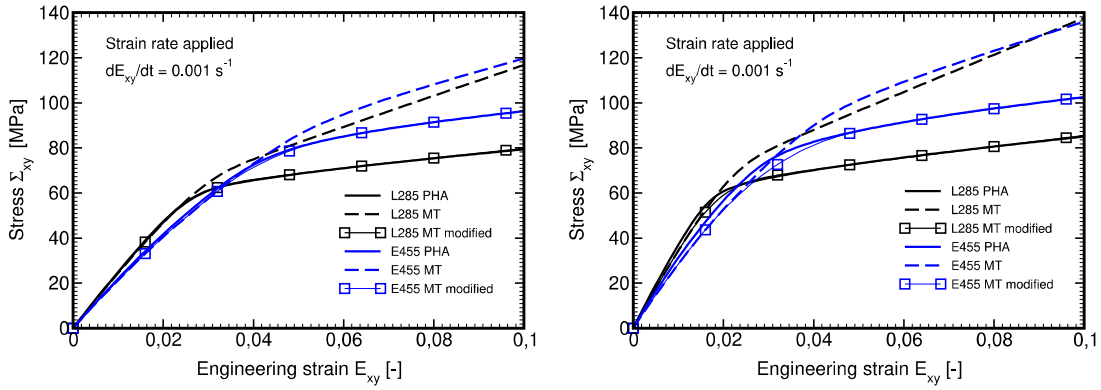

Figure 5.11: Comparing FEM, MT-original and MT-modified predictions: a) Carbon fibers, b) Basalt fibers

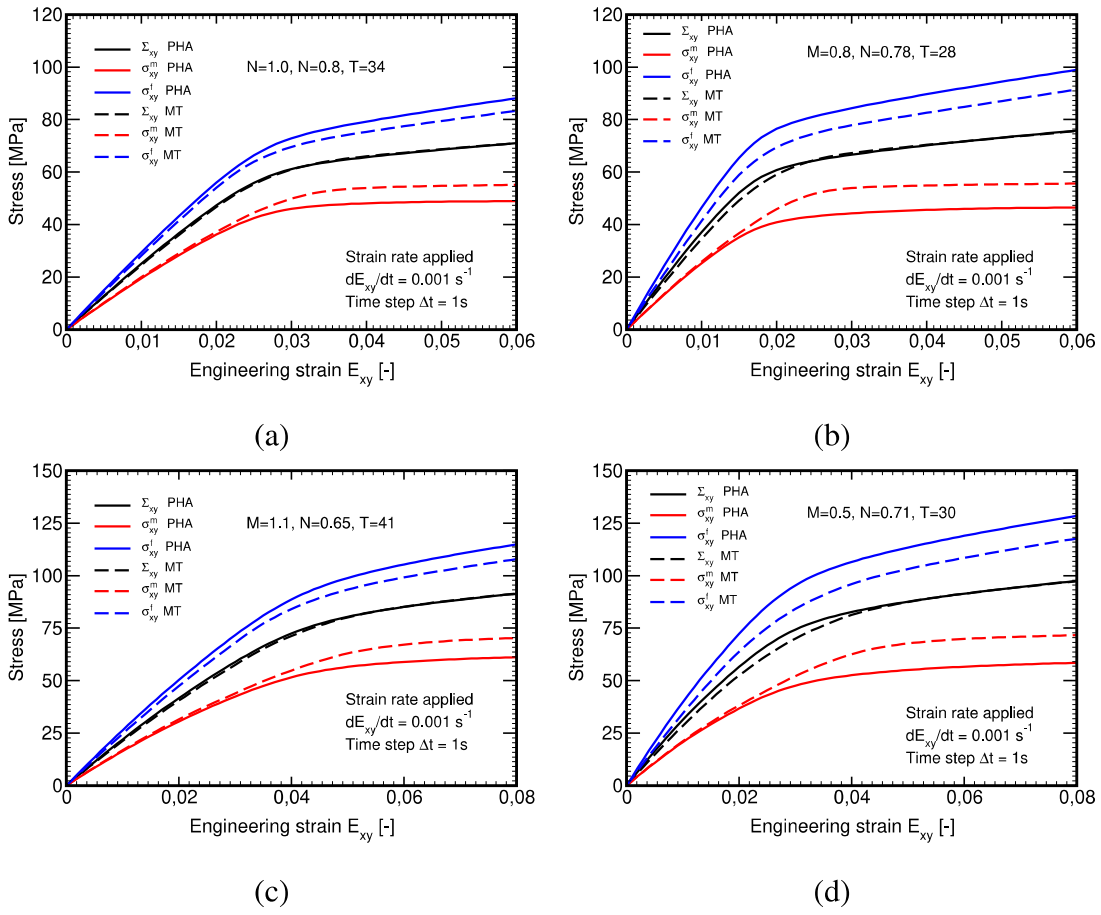

Figure 5.12: Local response (comparing FEM and modified MT method - stress-based formulation of damage model): a) L285-Carbon, b) L285-Basalt, c) E455-Carbon, d) E455-Basalt

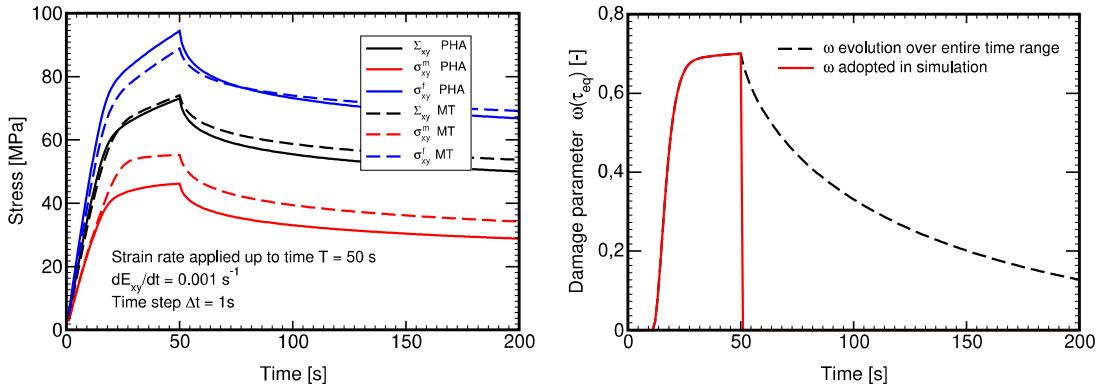

(a) (b)

Figure 5.13: Relaxation test performed on L285-Basalt composite: a) Time evolution of macroscopic strain E_{xy}, b) Time evolution of damage parameter ω

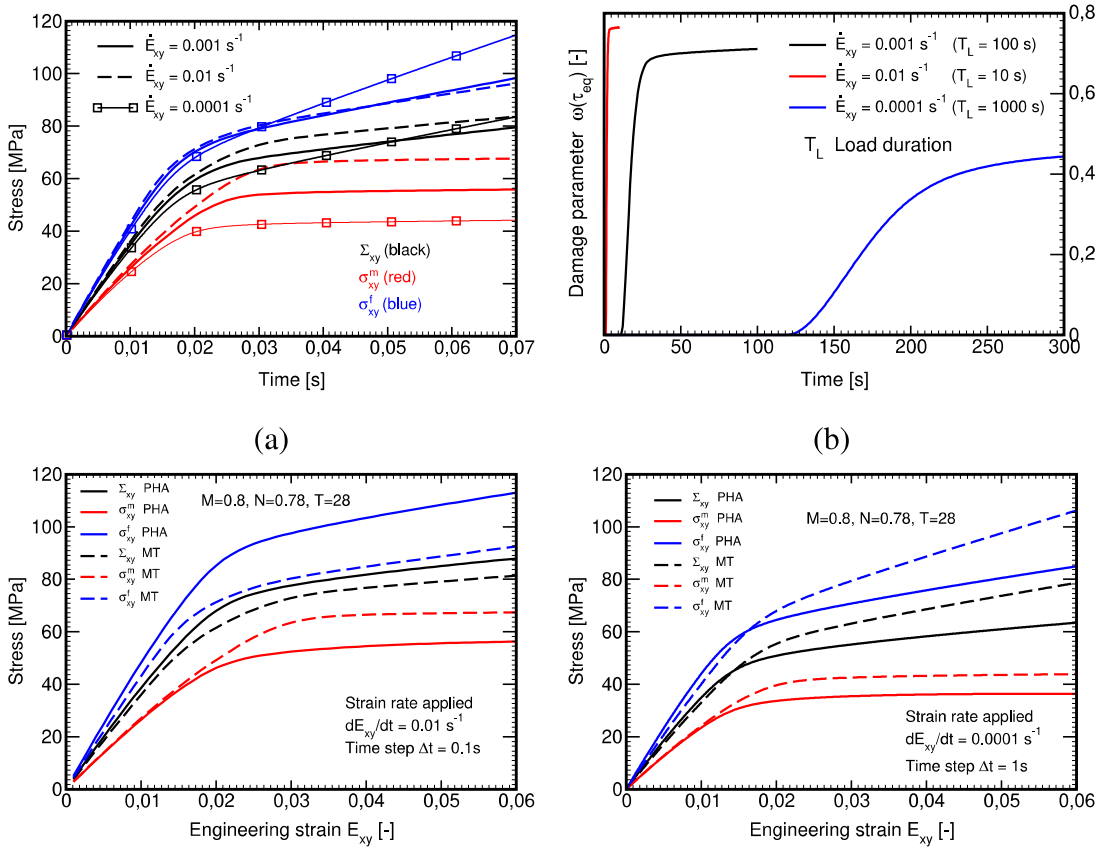

(a) (b)

(c) (d)

Figure 5.14: Strain rate effect on damage model parameters: a) Time-stress evolution for variable strain rate $\dot{E}_{xy}$ and identical set of M, N, T derived for $\dot{E}_{xy}$ =1E-3 s^{-1}, b) Evolution of ω, c) Comparison of MT and PHA predictions for $\dot{E}_{xy}$ =1E-2 s^{-1}, d) Comparison of MT and PHA predictions for $\dot{E}_{xy}$ =1E-4 s^{-4}

satisfactory for this particular case, its applicability for more complex loading conditions, e.g. cycling loading, is questionable.

Although partially expected, the strong dependence of the fitted parameters on the assumed strain rate loading is more disturbing, as evident in Fig. 5.14(a). The solid lines with no symbols correspond to the strain rate for which the model parameters M, N, T were estimated. The evolution of parameter ω in Fig. 5.14(b) is driven, together with the model parameters, by the evolution of equivalent deviatoric stress developed in the matrix phase, the red lines in Fig. 5.14(a). It now becomes clear why the stress reduction in the fiber phase is insufficient for lower strain rates, why for higher stress rates the reduction is too severe. This seen in Figs. 5.14(c,d), where the MT predictions are again compared with the FEM simulations adopting the PHA model. Recall that the results for the prescribed strain rate $\dot{E}_{xy}$ =1E-3s^{-1} (the strain rate to estimate M, N, T) are plotted in Fig. 5.12(b). This study thus suggests that a unique set of model parameters derived by matching the MT and FEM predictions for a given strain rate cannot satisfactorily remedy the original formulation of the MT method for different strain rates.

5.2.2.2 Formulation based on strain

The proposed formulation grounds on the structure of Eq. (5.9) but replaces the equivalent stress τ_{eq} with the viscoelastic equivalent deviatoric strain in the matrix $E^{ve}_{d,m} = \sqrt{2\boldsymbol{e}^{ve}_m \mathbf{Q} \boldsymbol{e}^{ve}_m}$. Considering only the viscoelastic part of the total strain allows us to simplify the model formulation as

$$\omega = N \left\{ 1 - \left[\frac{E^{ve,t}_{d,m}}{E^{0}_{d,m}} / \sinh \left(\frac{E^{ve,t}_{d,m}}{E^{0}_{d,m}} \right) \right] \right\}^{M} \tag{5.13}$$

where M, N are again the model parameters. Clearly, the former parameter T, originally introduced to delay the onset of damage, is no longer needed. The scaling parameter $E^0_{d,m}$ is written in terms of τ_0 and the elastic shear modulus G^{el}_m, recall Eq. (5.1), as

$$E^{0}_{d,m} = \frac{\tau_0}{G^{el}_m} \tag{5.14}$$

To examine this new formulation we run a similar set of numerical experiments as already presented in the previous section. The results are summarized in Figs. 5.15 and 5.16. For simplicity, attention is limited to L285-Basalt composite.

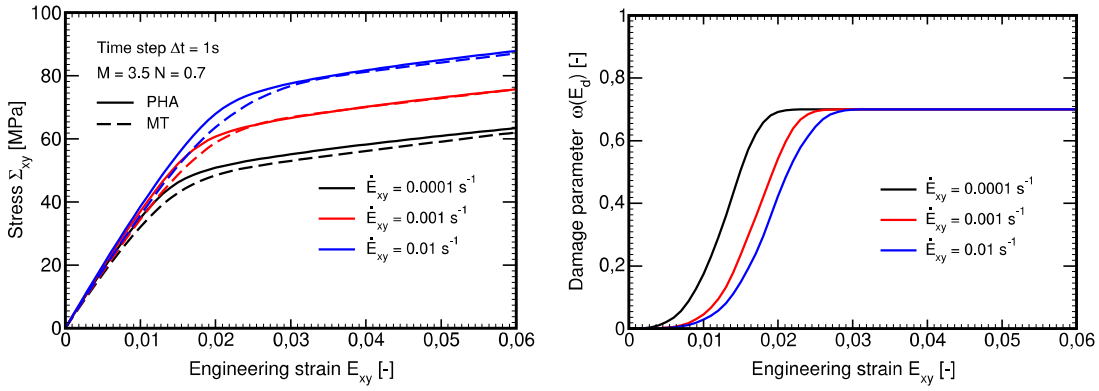

(a) (b)

Figure 5.15: a) Evolution of stress Σ_{xy} for different strain rates with model parameters fitted to $\dot{E}_{xy} = 0.001$ s^{-1}: comparison of MT and PHA predictions, b) Evolution of damage parameter ω for different strain rates

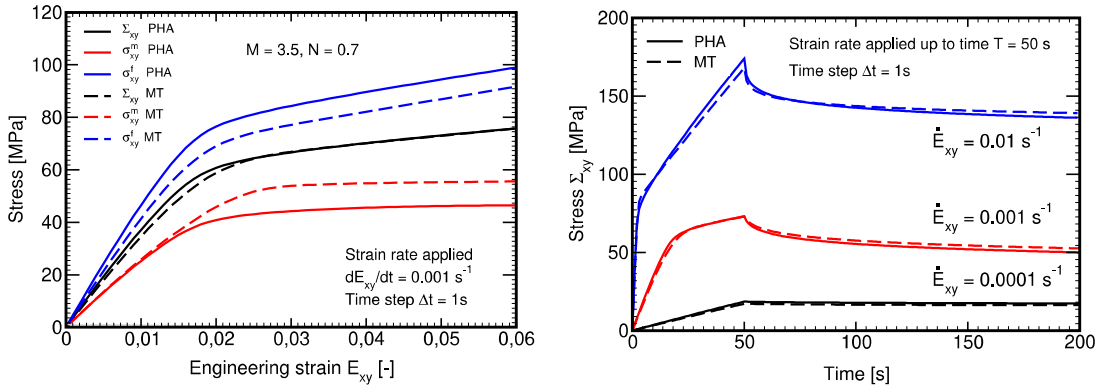

(a) (b)

Figure 5.16: a) Comparison of MT and PHA predictions for $\dot{E}_{xy}$ =1E-3 s^{-1}: evolution of stresses within individual phases, b) Relaxation test: time evolution of macroscopic strain E_{xy}

Figure 5.15(a) compares the macroscopic predictions provided by the PHA and MT models. The model parameters M, N were again fitted to shear strain $\dot{E}_{xy}$ =1E-3 s^{-1} and were kept the same for the remaining two strain rates. A considerable improvement when compared to stress based formulation is observed, recall Fig. 5.14. As seen in Fig. 5.15(b) the delay in damage initiation arises automatically with no need for an additional parameter T.

Evolution of macroscopic stresses in individual phases is demonstrated in Fig. 5.16(a) for strain rate $\dot{E}_{xy}$=1E-3 s^{-1}, compare with Fig. 5.12(b). As expected, the distribution of stress σ^m_{yx} in the matrix phase remains the same as the formulation has the influence on the fiber and overall stresses only. But even for the fiber phase the difference between the two formulations is, for a given set of model parameters, negligible. Finally, we address the effect of a variable strain rate on relaxation. As expected, the loading branch is captured satisfactorily. But the relaxation phase is identical to stress based formulation as the damage parameter needs to be turned off at the onset of relaxation.

As the model is generally isotropic it remains to check whether a single set of parameters will still be sufficient to account for other, more general, loading scenarios. In this regard, a recently proposed modeling strategy, see (Barral et al., 2020), might prove to be more robust.

5.2.3 Influence of actual microstructure of carbon and basalt fibrous composite

Despite a random distribution of fibers in the yarn cross-section, recall Fig. 5.1, we deemed the PHA model in all previous simulations as sufficient. This was supported by the expected statistical homogeneity suggested in the literature for similar types of material systems (Zeman and Šejnoha, 2001; Šejnoha and Zeman, 2013). On the contrary, it was promoted in other studies that so called Statistically Equivalent Periodic Unit Cell (SEPUC), which rigorously addressed the random nature of such composites via various statistical descriptors, seems to provide a better estimate of the homogenized response when compared to predictions based on a large RVE of the type depicted in Fig. 5.1 or the PHA model (Šejnoha and Zeman, 2002). However, the construction of SEPUC is not a trivial task and it goes beyond the present work. Nevertheless, the effect of randomness is still worth testing. In the present study, this is achieved by considering a certain test window taken randomly from a large image of a real microstructure (Tiberti and Milani, 2020; Krejčí et al., 2021).

Several examples of such RVEs (computational models) extracted from micrographs in Fig. 5.1 for both carbon and basalt fiber based composites are presented in Figs. 5.17 - 5.19. In total, twenty computational models, henceforth denoted as unit cells (UC) for convenience, were created for each material system such as to match the actual volume fraction as close as possible and to cover a sufficiently large range of cross-sectional areas. For illustration, we consider carbon fiber based composit where the smallest UC hav-

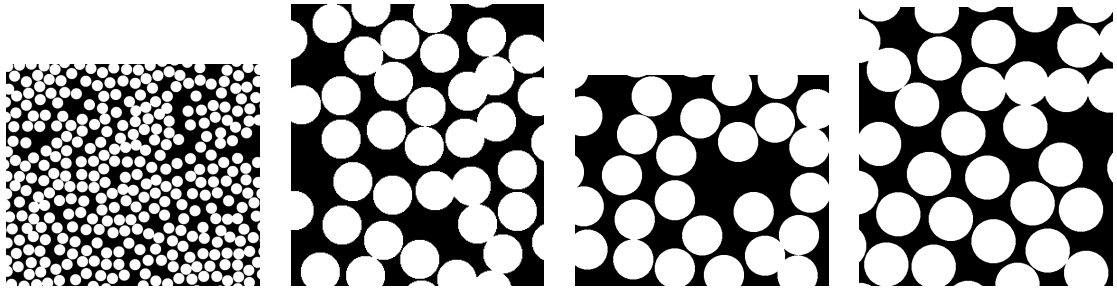

(a) (b) (c) (d)

Figure 5.17: Categorization based on volume fraction (c_f): a) Carbon $c_{f,\min}$, b) Carbon $c_{f,\max}$, c) Basalt $c_{f,\min}$, d) Basalt $c_{f,\max}$

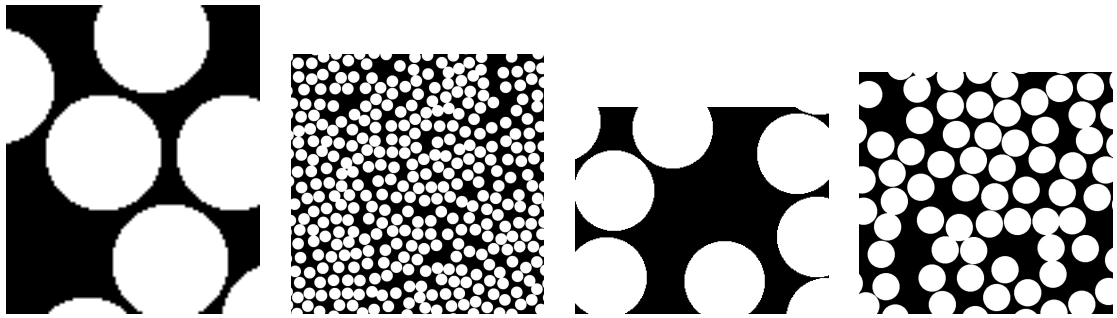

(a) (b) (c) (d)

Figure 5.18: Categorization based on area (A): a) Carbon $A_{\min}$, b) Carbon $A_{\max}$, c) Basalt $A_{\min}$, d) Basalt $A_{\max}$

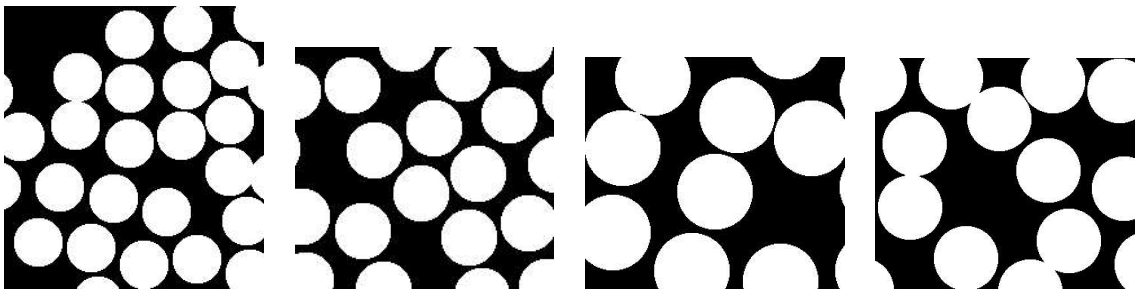

(a) (b) (c) (d)

Figure 5.19: Categorization based on stiffness (S): a) Carbon $S_{\min}$, b) Carbon $S_{\max}$, c) Basalt $S_{\min}$, d) Basalt $S_{\max}$

ing the area $A_{\min} = 228\mu$m consists of about 4 fibers while the largest UC with the area $A_{\max} = 18875\mu$m contains about 338 fibers. Point out that the number of fibers in large images in Fig. 5.1 is equal to 3200 and 880 for the carbon and basalt fiber based composites, respectively.

Table 5.6: Basic statistical parameters of unit cells for L285 matrix based composites

Composite	Carbon fiber based unit cells		Basalt fiber based unit cells	
Parameter	c_f [-]	$S \equiv G^{\mathsf{hom}}$ [GPa]	c_f [-]	$S \equiv G^{\mathsf{hom}}$ [GPa]
Mean	0.55	2.7	0.56	5.1
Std. dev	0.008	0.04	0.006	0.21
PHA	0.56	2.7	0.56	4.1
MT	0.56	2.6	0.56	3.8

Apart from volume fraction the UCs were categorized also according to their area and elastic effective shear stiffness. The basic statistical parameters are stored in Table 5.6. For comparison, the deterministic values pertinent to the PHA model and the MT method are also provided. The effective shear moduli are stored in Table 5.6.

Similar to the previous studies our attention was accorded to transverse shear loading under strain control regime. All composites were subjected to the prescribed shear strain rate $\dot{E}_{xy}$ =1E-3s^{-1}. The resulting effective response is plotted in Fig. 5.20. A comparable elastic response for the L285/Carbon composite suggested in Table 5.6 is supported by the stress-strain curves seen in Fig. 5.20(a). A similar conclusion can be drawn also for the E455/Carbon composite, see Fig. 5.20(c). Recall that for carbon fiber based composites the mismatch between in-plane shear moduli G_T of the matrix and fiber phase is relatively small. This, however, is not the case for basalt fiber based systems as already pointed out in Section 5.1.2. This might be the reason for a noticeable deviation of the elastic response predicted by the standard MT method and the PHA model when compared to UC models for the basalt fiber based composites evident in Figs. 5.20(b,d), see also Table 5.6. In this case the aforementioned general applicability of the PHA model for composites with a sufficiently high volume fraction of fibers is in question.

As for a nonlinear phase of the stress-strain curves we observe a relatively wide spread of results for all material systems. The bold lines were derived for cells with the minimum and maximum area ($A_{\min}$, $A_{\max}$), stiffness ($S_{\min}$, $S_{\max}$), and volume fraction ($c_{\min}$, $c_{\max}$), respectively, thus corresponding to computational models in Figs. 5.17 - 5.19. It is interesting to see that all simulations fall within the limits set by the models having the smallest

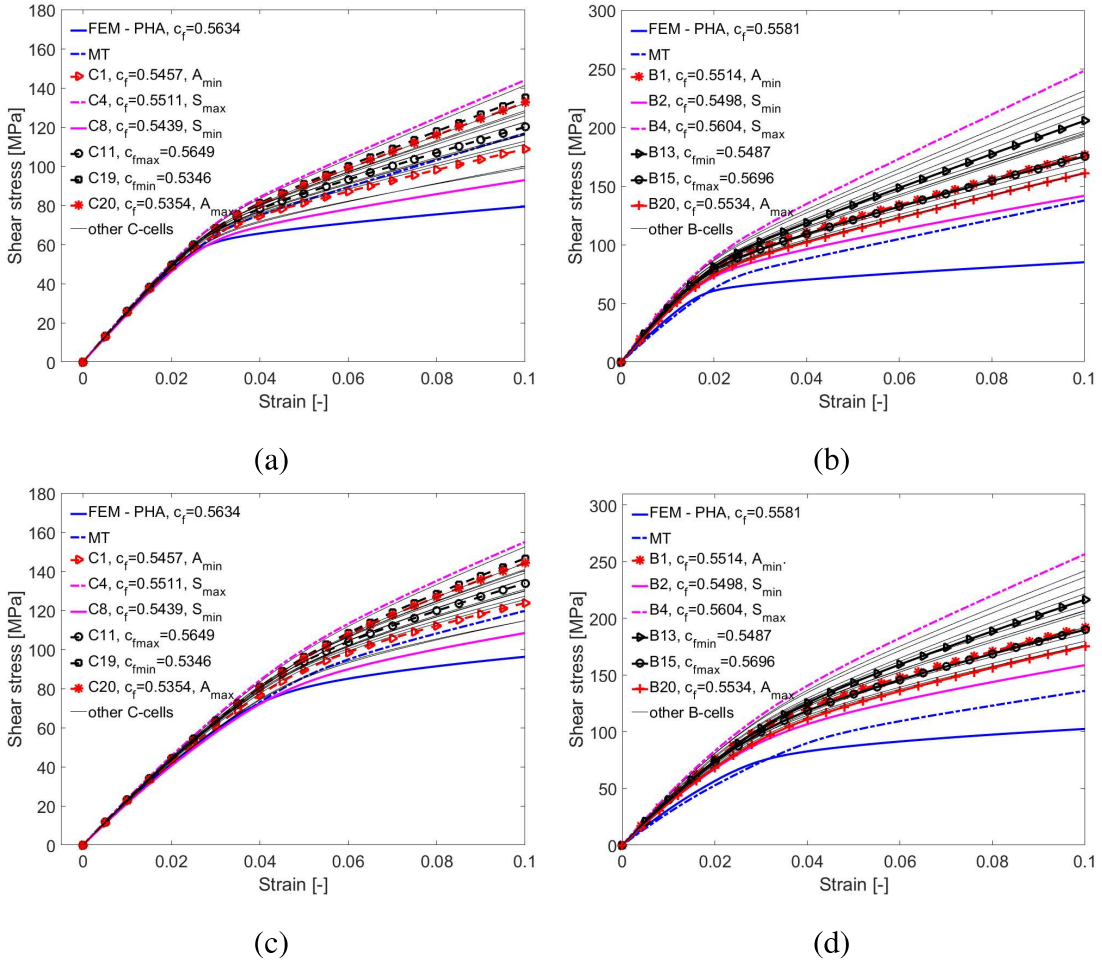

Figure 5.20: Effective shear response from all unit cells: a) L285-Carbon, b) L285-Basalt, c) E455-Carbon, d) E455-Basalt

and largest stiffness. On the other hand, no particular trend from the UC area point of view was experienced. This is rather surprising as the expected convergence with increasing size of UC, as shown for example in (Tiberti and Milani, 2020) for the nonlinear response of random masonry walls, has not been confirmed for the analyzed viscoelastic behavior. Another remark can be directed to the response predicted by the PHA model which appears more compliant when compared to all unit cells. This may suggest the need for a rigorously defined SEPUC as proposed, e.g., in (Zeman and Šejnoha, 2001). But as already mentioned, this not the subject of the present study.

Additional comparison in terms of the overall behavior of all material systems, further supporting the previous discussion, is available in Fig. 5.21. The graphs corresponding to

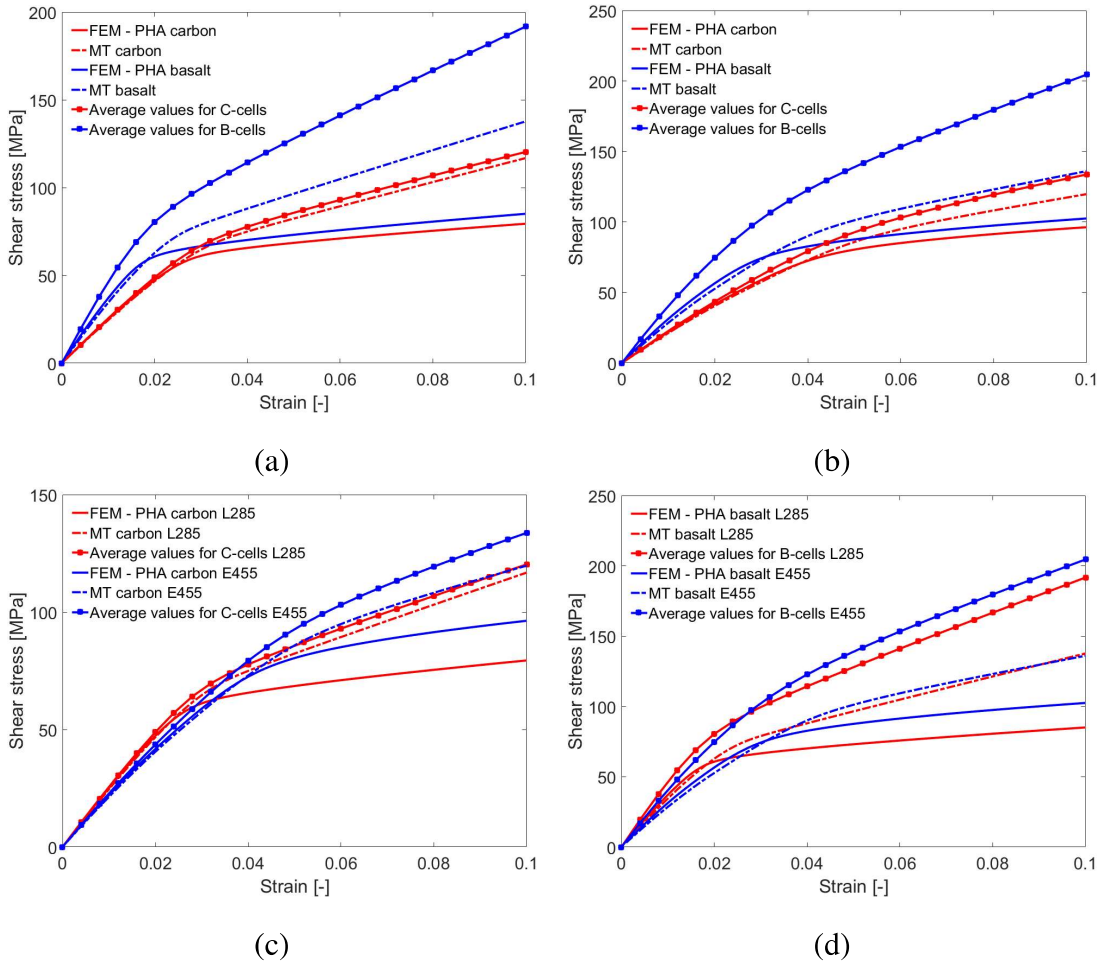

Figure 5.21: Comparing average response from random unit cells with PHA and standard MT predictions: a) L285-Carbon×Basalt, b) E455-Carbon×Basalt, c) Carbon-L285×E455, d) Basalt-L285×E455

the carbon (C-cells) and basalt (B-cells) fiber based systems represent averages obtained from all unit cells. We see that for carbon fiber based systems, unlike basalt fiber based composites, the MT method presented in its original format does not deviate much from the average response provided by random unit cells. The need for the proposed modifications for the studied random systems is again in question. This conclusion will be utilized in the next section devoted to the application of the MT method in multiscale analysis.

The evolution of local strains and stresses is finally demonstrated via surface plots in Figs. 5.22 - 5.29 for all examined material systems. Given the results in Fig. 5.20 we specifically focus on the cells with the lowest and the highest stiffness. With reference to strain

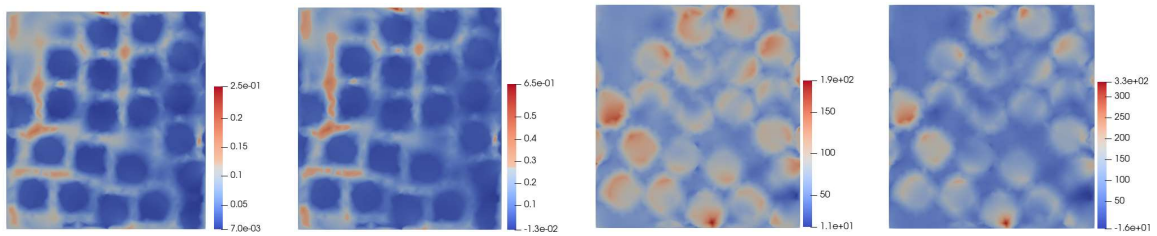

(a) (b) (c) (d)

Figure 5.22: L285-Carbon composite - RVE corresponding to **minimal** stiffness ($S_{\min}$). Surface plots of shear strains and stresses evolving in time: a) Strain at 50 s, b) Strain at 100 s, c) Stress at 100 s, d) Stress at 100 s

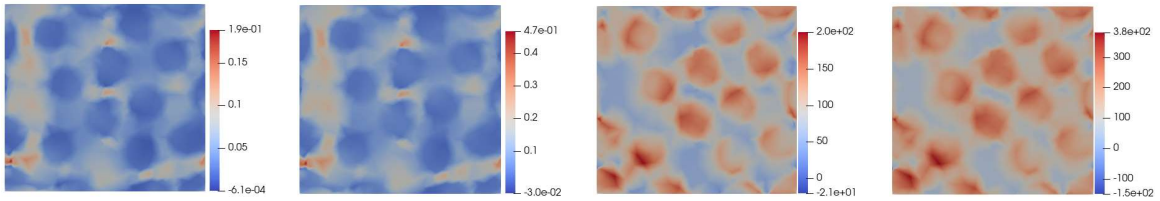

(a) (b) (c) (d)

Figure 5.23: L285-Carbon composite - RVE corresponding to **maximal** stiffness. Surface plots of shear strains and stresses evolving in time: a) Strain at 50 s, b) Strain at 100 s, c) Stress at 100 s, d) Stress at 100 s

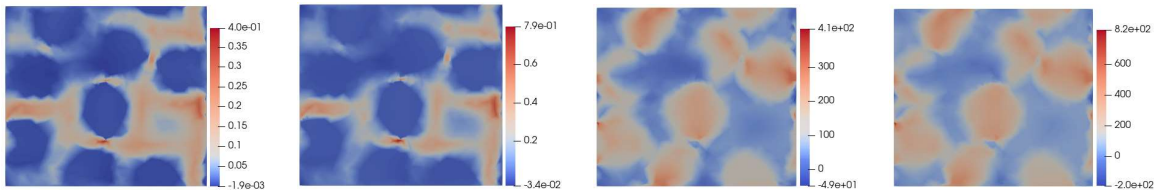

(a) (b) (c) (d)

Figure 5.24: L285-Basalt composite - RVE corresponding to **minimal** stiffness. Surface plots of shear strains and stresses evolving in time: a) Strain at 50 s, b) Strain at 100 s, c) Stress at 100 s, d) Stress at 100 s

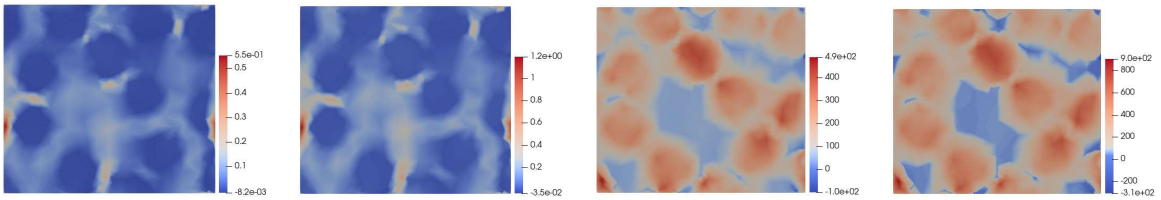

(a) (b) (c) (d)

Figure 5.25: L285-Basalt composite - RVE corresponding to **maximal** stiffness. Surface plots of shear strains and stresses evolving in time: a) Strain at 50 s, b) Strain at 100 s, c) Stress at 100 s, d) Stress at 100 s

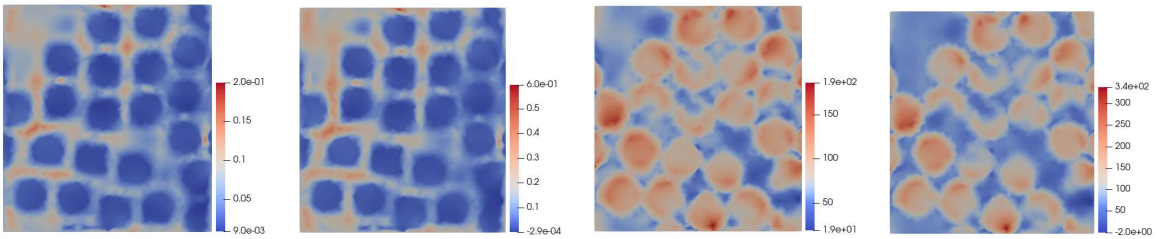

(a) (b) (c) (d)

Figure 5.26: E455-Carbon composite - RVE corresponding to **minimal** stiffness. Surface plots of shear strains and stresses evolving in time: a) Strain at 50 s, b) Strain at 100 s, c) Stress at 100 s, d) Stress at 100 s

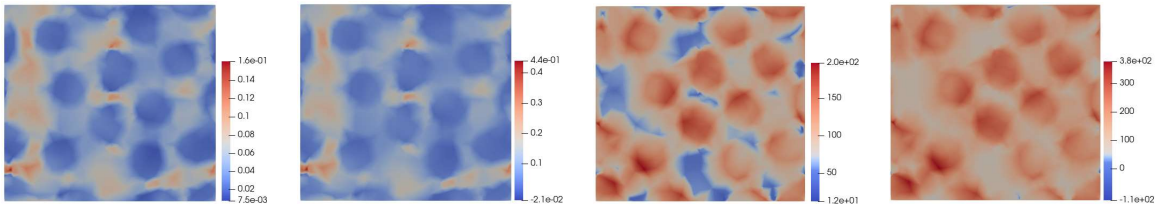

(a) (b) (c) (d)

Figure 5.27: E455-Carbon composite - RVE corresponding to **maximal** stiffness. Surface plots of shear strains and stresses evolving in time: a) Strain at 50 s, b) Strain at 100 s, c) Stress at 100 s, d) Stress at 100 s

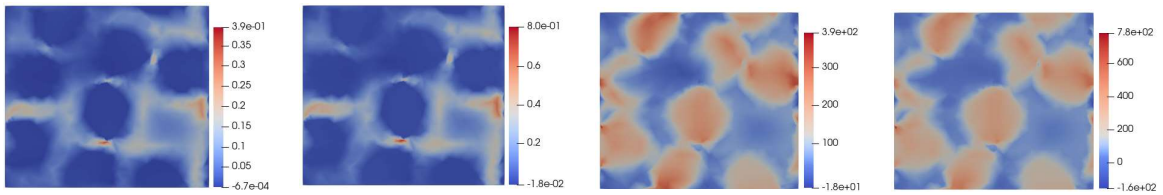

(a) (b) (c) (d)

Figure 5.28: E455-Basalt composite - RVE corresponding to **minimal** stiffness. Surface plots of shear strains and stresses evolving in time: a) Strain at 50 s, b) Strain at 100 s, c) Stress at 100 s, d) Stress at 100 s

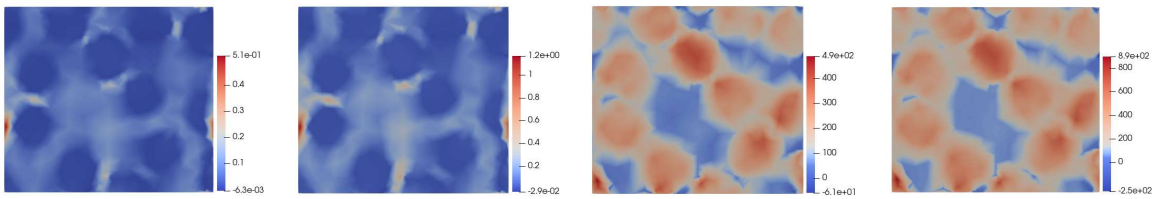

(a) (b) (c) (d)

Figure 5.29: E455-Basalt composite - RVE corresponding to **maximal** stiffness. Surface plots of shear strains and stresses evolving in time: a) Strain at 50 s, b) Strain at 100 s, c) Stress at 100 s, d) Stress at 100 s

it is evident that for the $S_{\min}$ cells, see Figs. 5.22, 5.24, 5.26 and 5.28, the matrix shear strain is more localized when compared to the $S_{\max}$ cells, see Figs. 5.23, 5.25, 5.27 and 5.29, where the corresponding distribution is more diffuse. This partially explains deviations of the macroscopic response pertinent to individual unit cells.

5.3 Two-scale simulation of textile composite combining FEM and MT method

To begin with, we point out that no experimental measurements performed directly on a textile ply as well as no numerical simulations in the framework of FE^2 multiscale analysis have been carried out for the examined material systems so far. This rules out both validation of the resulting numerical predictions and verification of the numerical implementation of the proposed two-scale computational scheme, where the MT method is selected to serve as a stress updater at the level of yarns. Therefore, we propose two simple loading scenarios enabling us to compare the performance of individual material systems and at the same time to partially check the numerical implementation. With reference to the results presented in Section 5.2.3 we limit our attention to standard MT formulation.

In particular, we compare the macroscopic response of all material systems to in-plane and out-of-plane shear and in-plane tension. To that end, we load the unit cell in Fig. 5.3 in turn by the macroscopic in-plane $\dot{E}_{xy} = 10^{-4}\text{s}^{-1}$ and out-of-plane $\dot{E}_{xz} = 10^{-4}\text{s}^{-1}$ shear strain rates and by the macroscopic tensile strain rate $\dot{E}_{xx} = 10^{-4}\text{s}^{-1}$. The same computational models were used to estimate the effective elastic properties in Section 5.1.3.2. The finite element mesh of the basalt fiber and carbon fiber based composite consisted of 51087 and 84448 constant strain tetrahedral elements, respectively. We remind the geometrical details of the two computational models given in Table 5.1.

Henceforth, the macroscopic stress-strain curve, the response at the level of textile ply, will be denoted as $\boldsymbol{\Sigma} \times \boldsymbol{E}$, while $\boldsymbol{\sigma}_m$ will denote the average stress in the matrix and $\boldsymbol{\sigma}_y$ the average stress in the yarn. Notice that $\Delta\boldsymbol{\sigma}_y = \Delta\overline{\boldsymbol{\sigma}}$ in Fig. 3.2 and is provided by the MT method for a given increment of the yarn strain $\Delta\boldsymbol{\varepsilon}_y = \Delta\overline{\boldsymbol{\varepsilon}}$. Similarly, the instantaneous yarn effective stiffness matrix $\widehat{\mathbf{L}}_y^{\mathsf{hom}}$ corresponds to $\mathbf{L}^{\mathsf{MT}}$ in Fig. 3.2. Clearly, each element of the yarn is treated as a two-phase unidirectional fibrous composite loaded by the increment of a mesoscopic strain $\Delta\boldsymbol{\varepsilon}_y$ computed in turn for a given increment of the macroscopic strain $\Delta\boldsymbol{E}$ (strain control regime) or stress $\Delta\boldsymbol{\Sigma}$ (stress control regime).

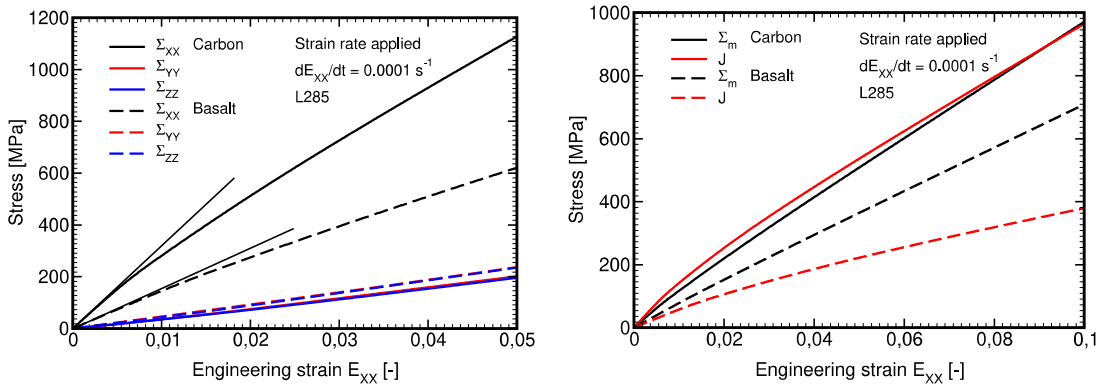

(a) (b)

Figure 5.30: L285 matrix based plain weave composite loaded in tension by prescribed macroscopic strain rate $\dot{E}_{xx}$ =1E-4s^{-1}: a) Macroscopic stress strain curves, b) Evolution of macroscopic and mean Σ_m and equivalent J stress

We begin with the tensile loading along the X direction. Point out that this is the case of a unidirectional strain where $\Delta E_{xx} \neq 0$ while all other strain components vanish. Such a constrained problem inevitably generates transverse stresses as seen in Fig. 5.30(a). Because we only wish to illustrate some specifics of the adopted constitutive model, we focus on the more compliant L285 matrix based systems. Along this direction the response is driven by the stiffness of the fiber phase where the matrix contribution is minor. This is also why the response is more or less elastic. Figure 5.30(a) also confirms a perfect symmetry in the weft and warp directions of the selected balanced plain weave composite and transverse isotropy of the yarns.

To confirm the expected elastic bulk response of the composite caused by the property of the generalized Leonov model, recall Section 4.1, we plot in Fig. 5.30(b) the evolution of the macroscopic mean stress $\Sigma_m = \frac{1}{3}\left(\Sigma_{XX} + \Sigma_{YY} + \Sigma_{ZZ}\right)$ and the macroscopic equivalent stress $J = \sqrt{\frac{1}{2} S_{ij} S_{ij}}$, $S_{ij} = \Sigma_{ij} - \delta_{ij}\Sigma_m$. The piecewise uniform evolution of these quantities in individual phases is displayed in Fig. 5.31. Clearly, in accordance with the Leonov model, the volumetric response of the matrix phase is fully elastic. A slight deviation of the macroscopic volumetric stress from linearity is caused by the nonlinearity evolving in the homogenized yarn.

The response of all material systems to the applied shear is displayed in Fig. 5.32. Unlike

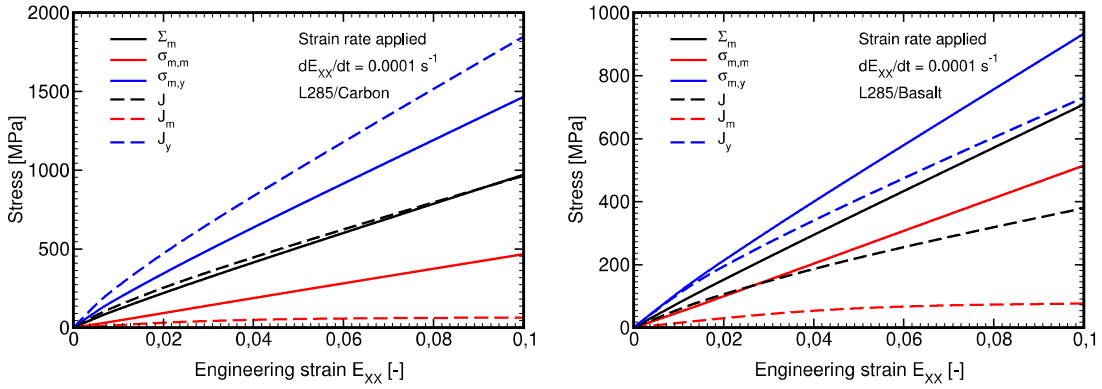

Figure 5.31: L285 matrix based plain weave composite loaded in tension by prescribed macroscopic strain rate $\dot{E}_{xx}$ =1E-4s^{-1}: a) Evolution of macroscopic and phase mean Σ_m and equivalent J stress for L285-Carbon composite, b) Evolution of macroscopic and phase mean Σ_m and equivalent J stress for L285-Basalt composite

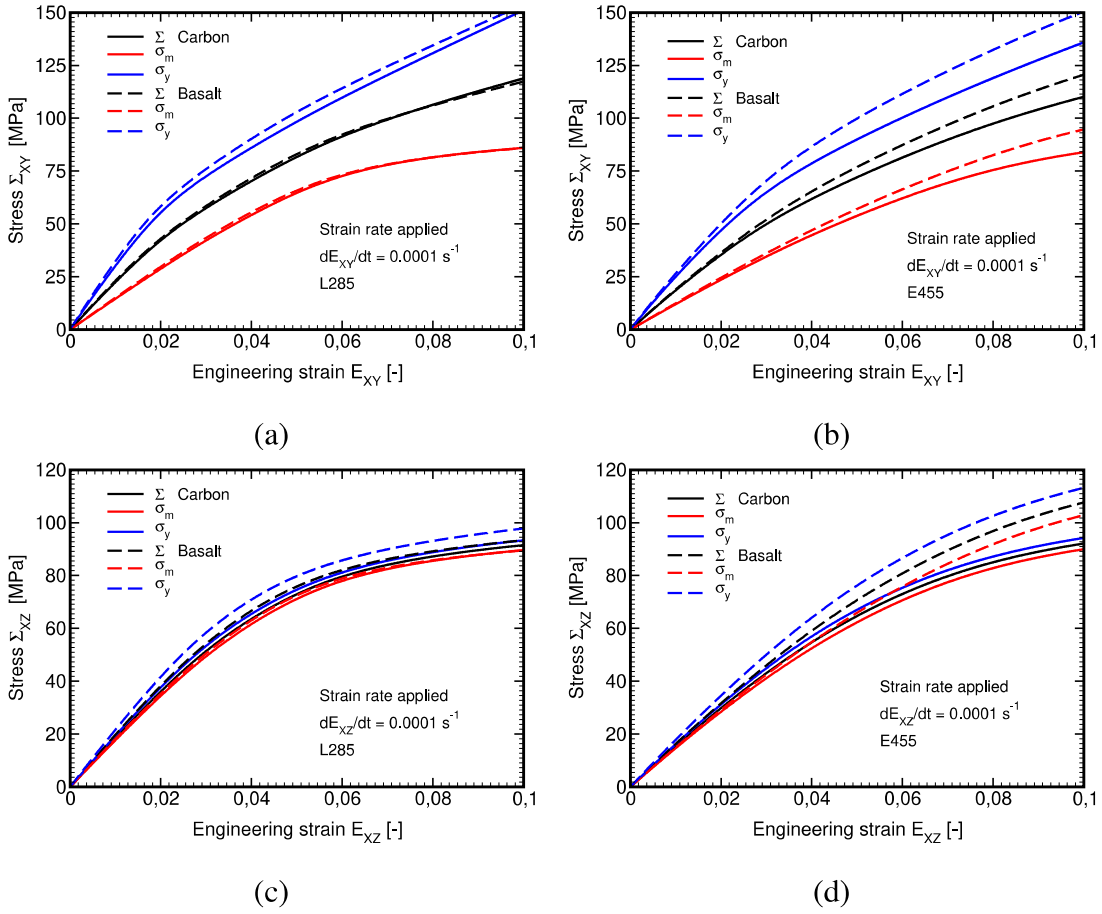

Figure 5.32: In-plane response XY ($\dot{E}_{XY}$ =1E-4s^{-1} applied) and out-of-plane XZ ($\dot{E}_{XZ}$ =1E-4s^{-1} applied) shear: a) $\Sigma_{XY} \times E_{XY}$, L285 matrix b) $\Sigma_{XY} \times E_{XY}$, E455 matrix, c) $\Sigma_{XZ} \times E_{XZ}$, L285 matrix d) $\Sigma_{XZ} \times E_{XZ}$, E455 matrix

tension, the response in shear is comparable for both types of reinforcements. A slightly stiffer response observed for the basalt fiber based systems is in accord with the predicted homogenized elastic stiffnesses stored in Table 5.5.

Chapter 6

DAMAGE MODELING OF TEXTILE PLIES

The experimental program described in Section 4.2 suggested that in a number of low technology applications the adopted matrices experience a brittle response or a transition from brittle (quasi-brittle) to viscous behavior depending on the applied strain rate. This raises the question concerning the use of the theory of damage mechanics even in the analysis of polymer matrix based material systems. This step would open the door to more complex formulation combining damage and viscoelasticity in a single constitutive equation (Bittnar and Šejnoha, 1996).

In fibrous composites the *matrix controlled failure mode* (transverse tensile or compressive matrix cracking accompanied by shear failure) must be combined with the *fiber controlled failure mode* both in tension (fiber breaking) and compression (fiber kinking combined with shear). The matrix controlled failure mode is often preceded by the fiber-matrix debonding initiating the matrix cracking both in the transverse and longitudinal direction.

Clearly, the damage processes in fibrous composites are complex and strongly dependent on the load conditions and thus on the stresses occurring at a material point. Combination of different interfaces (fiber-matrix, layers with different properties) and their mutual bond makes the mathematical description of the progressive failure difficult. This in turn may lead to an insufficient agreement between the computational predictions and experimental observations, which is further magnified by the fact that the nonlinear response of composites significantly depends on the implemented failure criteria. To arrive at reliable predictions from simulations thus immediately promotes multiscale modeling outlined in Section 5.3.

Some preliminary studies on the application of MT method in the analysis of quasi-brittle materials are already available, see e.g. (Vorel et al., 2012). Therefore, the proposed methodology combining FE and MT methods appears as a suitable method of attack. However, in the present study we adopt a certain simplification and consider the combination of damage and viscoelasticity on the mesoscale only (the level of textile ply). This allows us to fully decouple the two scales and concentrate directly on the failure modes associated with the yarn scale. Nevertheless, the multiscale modeling is not completely abandoned as we expect the homogenized material parameters driving the damage evolution in the yarn be derived from

virtual computational tests on microscale (the level of yarn) while neglecting the rheological effects.

With this simplification at hand we open this section by reviewing the most common failure criteria for fibrous composites. This is followed by the formulation of the adopted damage model including some aspects of numerical implementation. Attention is then accorded to virtual numerical tests on microscale.

It should be mentioned that this chapter describes the work in progress and should be considered as a possible extension of the studies carried out in the previous sections, which in turn represent the principal goal of this thesis. The incomplete experimental program is also the reason for not directly addressing the material systems examined so far. Instead, attention is devoted to a ceramic matrix composite where the polysiloxane matrix is reinforced by basalt fibers. The data not provided by our own experiments are taken from literature. With reference to the work published in (Valentová et al., 2017, 2018) we report only the results pertinent to the PHA model thus keeping consistency with Chapter 5. If not otherwise stated, the used coordinate system corresponds to that displayed in Fig. 5.2.

6.1 Unidirectional fibrous ply failure criteria

With reference to damage of the homogenized yarn we consider:

- Tensile or compressive strength of the yarn along the fiber direction, which depends mainly on the properties of the fiber.

- Tensile or compressive strength of the yarn in the transverse direction. Here, the matrix strength is of primary interest.

- Longitudinal and transverse shear strength of the composite, which arises primarily from the matrix shear strength and bond properties between the matrix and fiber.

The ply (yarn) strength parameters can be derived either from laboratory or virtual computational experiments, or the combination of the two. The last approach is preferable. In the present chapter, they will be denoted as[1]:

[1] Recall that z-direction is reserved in accordance with Fig. 5.2 for the fiber direction.

- T_L - tensile strength in the longitudinal direction z
- T_T - tensile strength in the transverse directions x and y
  - T_{xx} - tensile strength in the transverse direction x
  - T_{yy} - tensile strength in the transverse direction y
- C_L - compressive strength in the longitudinal direction z
- C_T - compressive strength in the transverse directions x and y
  - C_{xx} - compressive strength in the transverse direction x
  - C_{yy} - compressive strength in the transverse direction y
- S_L - longitudinal (out-of plane) shear strength in xz and yz planes
- S_T - transverse (in-plane) shear strength in xy plane

6.1.1 Selected strength failure criteria

Each of the theories bellow introduces different criteria for failure of the system. We can divide them into the two specific groups:

- Non-interactive criteria - the interaction between the components of the stress tensor in the material point is not taken into account.
- Interactive criteria - take into account the interaction between the components of the stress tensor.

The first group assumes different limit values of stress or strain in each of the three main directions of the material. They are relatively simple, which is also their main advantage. On the other hand, they provide generally less accurate results in comparison to the interactive ones, which in turn assume that the failure of the structure component in one direction can be sensitive to the loading in other directions, including shear stress. They include:

- Maximum stress criterion

- Maximum strain criterion

The interactive criteria mentioned henceforth are:

- Tsai-Wu failure criterion
- Hashin failure criteria
- Modified Hashin failure criteria
- Christensen failure criteria
- LaRC05 failure criterion for matrix dominated mode combined with fiber kinking and fiber tensile failure mode

6.1.2 Tsai-Wu failure criterion

The Tsai-Wu criterion, see (Tsai and Wu, 1971), is well known and perhaps the most often used failure criterion for unidirectional fiber reinforced composites. It is a single failure criterion which does not decompose the failure into fiber and matrix controlled mode and thus precludes its application in highly anisotropic materials. The mathematical formulation of the Tsai-Wu failure criterion for transversely isotropic materials reads

$$\left(\frac{1}{T_L}-\frac{1}{C_L}\right)\sigma_{zz}+\left(\frac{1}{T_T}-\frac{1}{C_T}\right)(\sigma_{xx}+\sigma_{yy})+\frac{\sigma_{zz}^2}{T_L C_L}+\frac{1}{T_T C_T}(\sigma_{xx}+\sigma_{yy})^2+$$
$$+F_{xz}\sigma_{zz}(\sigma_{xx}+\sigma_{yy})+\frac{1}{S_T^2}\left(\sigma_{xy}^2-\sigma_{xx}\sigma_{yy}\right)+\frac{1}{S_L^2}\left(\sigma_{xz}^2+\sigma_{yz}^2\right)\leq 1, \tag{6.1}$$

where F_{xz} is called an interaction parameter usually determined experimentally.

6.1.3 Hashin failure criteria

Hashin established the need for failure criteria that are based on failure mechanisms. He used his experimental observations of failure of tensile specimens to propose two different failure criteria, one related to the fiber failure and the other to the matrix failure. The criteria assume a quadratic interaction between the tractions acting on the plane of failure. He introduced fiber and matrix failure criteria that distinguish between tension and compression failure.

Given the difficulty in obtaining the plane of fracture for the matrix compression mode, Hashin used a quadratic interaction between stress invariants.

The Hashin criteria (Hashin, 1980) decompose into separate fiber and matrix failure modes both for the tension and compression thus distinguishing the following four modes of failure:

- Tensile fiber mode ($\sigma_{zz} > 0$)

$$\left(\frac{\sigma_{zz}}{T_L}\right)^2 + \frac{\sigma_{xz}^2 + \sigma_{yz}^2}{S_L^2} \leq 1 \tag{6.2}$$

- Compressive fiber mode ($\sigma_{zz} < 0$)

$$\left(\frac{\sigma_{zz}}{C_L}\right)^2 \leq 1 \tag{6.3}$$

- Tensile matrix mode ($\sigma_{xx} + \sigma_{yy} > 0$)

$$\frac{1}{T_T^2}\left(\sigma_{xx} + \sigma_{yy}\right)^2 + \frac{1}{S_T^2}\left(\sigma_{xy}^2 - \sigma_{xx}\sigma_{yy}\right) + \frac{1}{S_L^2}\left(\sigma_{xz}^2 + \sigma_{yz}^2\right) \leq 1 \tag{6.4}$$

- Compressive matrix mode ($\sigma_{xx} + \sigma_{yy} < 0$)

$$\frac{1}{C_T^2}\left[\left(\frac{C_T}{2S_T}\right)^2 - 1\right]\left(\sigma_{xx} + \sigma_{yy}\right) + \frac{1}{4S_T^2}\left(\sigma_{xx} + \sigma_{yy}\right)^2 + \\ + \frac{1}{S_T^2}\left(\sigma_{xy}^2 - \sigma_{xx}\sigma_{yy}\right) + \frac{1}{S_L^2}\left(\sigma_{xz}^2 + \sigma_{yz}^2\right) \leq 1 \tag{6.5}$$

One of the disadvantage of the Hashin forms is that five particular assumptions are involved to derive criteria in the forms written above with acceptable levels of the six strength properties, particularly the tensile, compressive and shear strengths in both longitudinal and transverse direction. In addition, in the case of transverse tension the fracture planes are parallel to the fiber direction and either normal or parallel to the ply (yarn) mid-plane. But for the matrix compression, the plane of fracture may not in general be aligned with the fiber direction but rotated through a certain angle. This is not reflected in the Hashin failure criterion, which thus calls for improvement.

Further to this matter, numerous studies conducted over the past decade indicate that the stress interactions proposed by Hashin do not always fit the experimental results, especially in the case of matrix or fiber compression. It is well known, for instance, that moderate

transverse compression increases the apparent shear strength of a ply, which is not well predicted by Hashin's criterion. In addition, Hashin's fiber compression criterion does not account for the effects of in-plane shear, which reduce significantly the effective compressive strength of a ply (Davila et al., 2005).

6.1.4 Modified Hashin failure criteria

Modifications to Hashin's criteria to improve their predictive capabilities have been proposed by several researchers. These are, for instance, described in (Zhou et al., 2013), where three typical damage mechanisms are coupled together in the loading process, including transverse matrix cracking, fiber-matrix shearing debond and longitudinal fiber breakage.

Varieties of the modified criteria based on Hashin's failure criteria can be classified into three categories. The first type treats the transverse matrix cracking in two transverse directions independently. The second type is identical to the first one, except using the maximum stress criterion to detect the longitudinal fiber breakage. The third one introduces the Hahn and Tsai shear nonlinearity model into the failure criteria and takes the history of the shear deformation into account.

The formal-unified 3D Hashin criteria read (Zhou et al., 2013):

- Fiber tensile failure $\sigma_{zz} > 0$

$$\left(\frac{\sigma_{zz}}{T_L}\right)^2 + \left(\frac{\frac{\sigma_{xz}^2}{2G_{xz}} + \frac{3}{4}A\sigma_{xz}^4}{\frac{S_{xz}^2}{2G_{xz}} + \frac{3}{4}AS_{xz}^4}\right) + \left(\frac{\frac{\sigma_{yz}^2}{2G_{yz}} + \frac{3}{4}A\sigma_{yz}^4}{\frac{S_{yz}^2}{2G_{yz}} + \frac{3}{4}AS_{yz}^4}\right) \leq 1 \tag{6.6}$$

- Fiber compressive failure $\sigma_{zz} < 0$

$$\left(\frac{\sigma_{zz}}{C_L}\right)^2 + \left(\frac{\frac{\sigma_{xz}^2}{2G_{xz}} + \frac{3}{4}A\sigma_{xz}^4}{\frac{S_{xz}^2}{2G_{xz}} + \frac{3}{4}AS_{xz}^4}\right) + \left(\frac{\frac{\sigma_{yz}^2}{2G_{yz}} + \frac{3}{4}A\sigma_{yz}^4}{\frac{S_{yz}^2}{2G_{yz}} + \frac{3}{4}AS_{yz}^4}\right) \leq 1 \tag{6.7}$$

- Matrix tensile failure in direction x, $\sigma_{xx} > 0$

$$\left(\frac{\sigma_{xx}}{T_{xx}}\right)^2 + \left(\frac{\frac{\sigma_{xz}^2}{2G_{xz}} + \frac{3}{4}A\sigma_{xz}^4}{\frac{S_{xz}^2}{2G_{xz}} + \frac{3}{4}AS_{xz}^4}\right) + \left(\frac{\sigma_{xy}}{S_T}\right)^2 \leq 1 \tag{6.8}$$

- Matrix compressive failure in direction x, $\sigma_{xx} < 0$

$$\left(\frac{\sigma_{xx}}{C_{xx}}\right)^2 + \left(\frac{\frac{\sigma_{xz}^2}{2G_{xz}} + \frac{3}{4}A\sigma_{xz}^4}{\frac{S_{xz}^2}{2G_{xz}} + \frac{3}{4}AS_{xz}^4}\right) + \left(\frac{\sigma_{xy}}{S_T}\right)^2 \leq 1 \tag{6.9}$$

- Matrix tensile failure in direction y, $\sigma_{yy} > 0$

$$\left(\frac{\sigma_{yy}}{T_{yy}}\right)^2 + \left(\frac{\frac{\sigma_{yz}^2}{2G_{yz}} + \frac{3}{4}A\sigma_{yz}^4}{\frac{S_{yz}^2}{2G_{yz}} + \frac{3}{4}AS_{yz}^4}\right) + \left(\frac{\sigma_{xy}}{S_T}\right)^2 \leq 1 \tag{6.10}$$

- Matrix compressive failure in direction y, $\sigma_{yy} < 0$

$$\left(\frac{\sigma_{yy}}{C_{yy}}\right)^2 + \left(\frac{\frac{\sigma_{yz}^2}{2G_{yz}} + \frac{3}{4}A\sigma_{yz}^4}{\frac{S_{yz}^2}{2G_{yz}} + \frac{3}{4}AS_{yz}^4}\right) + \left(\frac{\sigma_{xy}}{S_T}\right)^2 \leq 1 \tag{6.11}$$

where A is the shear correction factor.

For plain weave textile composites, the modified Hashin criteria, Eqs. (6.8) - (6.11), were adopted in (Zhou et al., 2013) while neglecting the shear contribution factor A. When assuming transverse isotropy ($T_{xx} = T_{yy} = T_T, C_{xx} = C_{yy} = C_T, S_{xz} = S_{yz} = S_L$) this yields

- Fiber tensile failure, $\sigma_{zz} > 0$

$$\left(\frac{\sigma_{zz}}{T_L}\right)^2 + \left(\frac{\sigma_{xz}}{S_L}\right)^2 + \left(\frac{\sigma_{yz}}{S_L}\right)^2 \leq 1 \tag{6.12}$$

- Fiber compressive failure, $\sigma_{zz} < 0$

$$\left(\frac{\sigma_{zz}}{C_L}\right)^2 \leq 1 \tag{6.13}$$

- Matrix tensile failure in direction x, $\sigma_{xx} > 0$

$$\left(\frac{\sigma_{xx}}{T_T}\right)^2 + \left(\frac{\sigma_{xz}}{S_L}\right)^2 + \left(\frac{\sigma_{xy}}{S_T}\right)^2 \leq 1 \tag{6.14}$$

- Matrix compressive failure in direction x, $\sigma_{xx} < 0$

$$\left(\frac{\sigma_{xx}}{C_T}\right)^2 + \left(\frac{\sigma_{xz}}{S_L}\right)^2 + \left(\frac{\sigma_{xy}}{S_T}\right)^2 \leq 1 \tag{6.15}$$

- Matrix tensile failure in direction y, $\sigma_{yy} > 0$

$$\left(\frac{\sigma_{yy}}{T_T}\right)^2 + \left(\frac{\sigma_{yz}}{S_L}\right)^2 + \left(\frac{\sigma_{xy}}{S_T}\right)^2 \leq 1 \tag{6.16}$$

- Matrix compressive failure in direction y, $\sigma_{yy} < 0$

$$\left(\frac{\sigma_{yy}}{C_T}\right)^2 + \left(\frac{\sigma_{yz}}{S_L}\right)^2 + \left(\frac{\sigma_{xy}}{S_T}\right)^2 \leq 1 \tag{6.17}$$

Assuming no interaction of stress components we arrive for the maximum stress criterion at

$$\left(\frac{\sigma_J}{F_J}\right)^2 \leq 1 \tag{6.18}$$

where F_J is the prescribed strength criterion which can be different for tension and compression. In particular:

$$\begin{aligned}
&\left(\frac{\sigma_{zz}}{T_L}\right)^2 \leq 1 \quad (\sigma_{zz} > 0), \qquad \left(\frac{\sigma_{zz}}{C_L}\right)^2 \leq 1 \quad (\sigma_{zz} < 0)\\
&\left(\frac{\sigma_{xx}}{T_T}\right)^2 \leq 1 \quad (\sigma_{xx} > 0), \qquad \left(\frac{\sigma_{xx}}{C_T}\right)^2 \leq 1 \quad (\sigma_{xx} < 0)\\
&\left(\frac{\sigma_{yy}}{T_T}\right)^2 \leq 1 \quad (\sigma_{yy} > 0), \qquad \left(\frac{\sigma_{yy}}{C_T}\right)^2 \leq 1 \quad (\sigma_{yy} < 0)\\
&\left(\frac{\sigma_{xz}}{S_L}\right)^2 \leq 1, \qquad \left(\frac{\sigma_{yz}}{S_L}\right)^2 \leq 1, \qquad \left(\frac{\sigma_{xy}}{S_T}\right)^2 \leq 1
\end{aligned}$$

These criteria were employed, e.g., in (Šmilauer et al., 2011).

6.1.5 Failure criteria according to Christensen

In (Christensen, 2008) the failure criteria are defined for anisotropic fiber composite materials with transversely isotropic symmetry. A further condition is a large degree of anisotropy of the system, which is consistent with high stiffness and high strength basalt fiber composites with the polymer matrix. The condition of high anisotropy also implies the fact that shear strengths are much smaller than the uniaxial tensile and compressive strengths in the fiber direction. The failure criteria are decomposed into two separate modes, fiber and matrix, and are completely guided by the strength properties in tension, compression and shear, see also (Christensen, 2013) for further details. They receive the following forms:

- Fiber controlled failure

$$\left(\frac{1}{T_L}-\frac{1}{C_L}\right)\sigma_{zz}+\frac{1}{T_L C_L}\sigma_{zz}^2\leq 1 \tag{6.19}$$

- Matrix controlled failure

$$\begin{aligned}&\left(\frac{1}{T_T}-\frac{1}{C_T}\right)(\sigma_{xx}+\sigma_{yy})+\frac{1}{T_T C_T}(\sigma_{xx}+\sigma_{yy})^2+\\&+\frac{1}{S_T^2}\left(\sigma_{xy}^2-\sigma_{xx}\sigma_{yy}\right)+\frac{1}{S_L^2}\left(\sigma_{xz}^2+\sigma_{yz}^2\right)\leq 1\end{aligned} \tag{6.20}$$

It is tempting to identify the fiber controlled failure criterion with the maximum stress criterion. The maximum stress criterion has always been considered to be a highly useful but totally empirical one. On the contrary, it is suggested in (Christensen, 2008) that the form of Eq. (6.19), with the assumption of a high degree of anisotropy, is not empirical at all, but rational result of the method.

6.1.6 LaRC05 failure criterion for matrix dominated mode combined with fiber kinking and fiber tensile failure mode

Similar to Christensen's failure criteria the formulation distinguishes between the fiber and matrix dominated failure models. In the fiber dominated mode the difference is made in the tensile breakage of fibers and the failure caused by fiber kinking. As for the matrix dominated mode the previous formulations presented in terms of stresses acting along the material principal directions are abandoned to allow for the fracture plane parallel to fiber direction to develop in an arbitrary angle measured in the transverse plane.

The model development comes from the work of (Davila et al., 2005; Pinho et al., 2006a,b) and its present format, LaRC05 version (Pinho et al., 2020), has recently been implemented into ABAQUS. Successful practical applications can be found, e.g., in (Fang et al., 2011; Wang et al., 2020; Zhang et al., 2022). Henceforth, we limit our attention to the matrix dominated mode and similar to (Zhang et al., 2022) assume the fiber dominated mode to be well represented by the maximum stress criteria both in tension and compression. To address fiber kinking in a more complex way we refer the reader to (Pinho et al., 2020).

Figure 6.1 shows the matrix fracture plane and corresponding normal σ_n, in-plane shear τ_T, and out-of-plane shear τ_L tractions obtained from standard coordinate transformation of

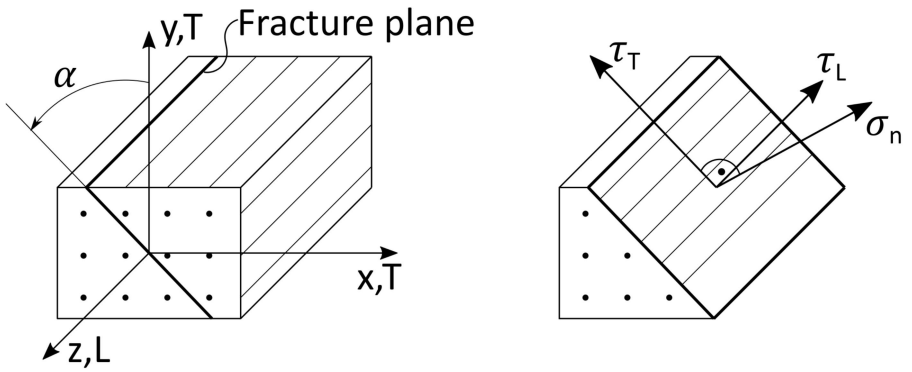

(a) (b)

Figure 6.1: Matrix fraction plane: a) Coordinate system, b) Traction components

a 2nd order tensor as

$$\sigma_n(\alpha) = \frac{\sigma_{xx}+\sigma_{yy}}{2} + \frac{\sigma_{xx}+\sigma_{yy}}{2}\cos 2\alpha + \tau_{xy}\sin 2\alpha \tag{6.21}$$

$$\tau_T(\alpha) = \frac{\sigma_{xx}-\sigma_{yy}}{2}\sin(2\alpha) + \tau_{xy}\cos(2\theta) \tag{6.22}$$

$$\tau_L(\alpha) = \tau_{xz}\cos\alpha + \tau_{yz}\sin\alpha \tag{6.23}$$

where $\alpha \in (0°, 180°)$ defines the fracture plane orientation and it is the angle that maximizes the failure function written as (Pinho et al., 2020)

$$\left(\frac{\tau_T}{S_T - \mu_T\sigma_n}\right)^2 + \left(\frac{\tau_L}{S_L - \mu_L\sigma_n}\right)^2 + \left(\frac{\langle\sigma_n\rangle^2}{T_T}\right) \leq 1 \tag{6.24}$$

Clearly, this is a variant of the Mohr-Coulomb shear failure function taking into account the pressure dependency. Note that $\langle x\rangle = (x + |x|)/2$. As suggested in (Pinho et al., 2020) the last term on the left hand side contributes to the crack opening in tension so it drops out when σ_n becomes negative. For pure transverse compression the authors introduce an angle α_0 which can be measured experimentally for a given type of composite. It provides the transverse μ_T and the longitudinal μ_L friction coefficients in the form (Pinho et al., 2020; Zhang et al., 2022)

$$\mu_T = -\frac{1}{\tan(2\alpha_0)}, \quad S_T = \frac{C_T}{2\tan(\alpha_0)}, \quad \mu_L = \mu_T\frac{S_L}{S_T} \tag{6.25}$$

6.2 Fracture energy and crack band model

We rely on well established concept of continuum damage mechanics combined with the crack band model (Bažant and Oh, 1983) to ensure objectivity of numerical simulations.

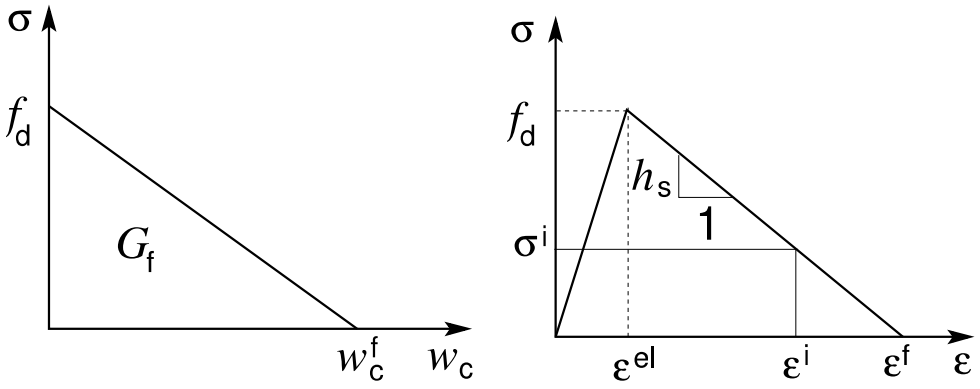

(a) (b)

Figure 6.2: Linear softening law: a) Stress-crack opening displacement diagram, b) Stress-strain diagram with softening

To briefly review this subject consider a uniaxial tensile loading. Next, recall the fracture energy (G_f [Nm^{-1}]) as the material property that corresponds to the area under the stress - crack opening displacement diagram as shown in Fig. 6.2(a)

$$G_f = \int_0^{w_c^f} \sigma \, \mathrm{d}w_c \tag{6.26}$$

Suppose that the displacement discontinuity is smeared over a certain distance L_s, which transforms the crack opening displacement into an inelastic strain ε_c. While the decohesion process is objectively described by the traction-separation law

$$\sigma = f_w(w_c) \tag{6.27}$$

the corresponding stress-strain law with softening in Fig. 6.2(b)

$$\varepsilon = \frac{\sigma}{E} + \varepsilon_c, \qquad \varepsilon_c = \frac{w_c}{L_s} \tag{6.28}$$

becomes dependent on the smearing distance L_s. For the two models to be equivalent it is thus necessary that the smearing distance (a finite band of localized strain) will correspond to

the numerically resolved localization band being depended on the underlying finite element mesh. Clearly, the softening modulus h_s in Fig. 6.2(b) is mesh dependent and cannot be considered as objective material property. This modulus is thus termed the mesh-adjusted softening modulus. Combining Eqs. (6.26) and (6.28) gives the fracture energy in the form

$$G_f = \int_0^{w_c^f} \sigma \, \mathrm{d}w_c = L_s \int_0^{f_d} (\varepsilon - \varepsilon^{el}) \, \mathrm{d}\sigma = L_s \int_0^{\varepsilon^f} \sigma \, \mathrm{d}\varepsilon \tag{6.29}$$

as the area under the stress-strain curve multiplied by the smearing-distance L_s. The smearing distance is deduced from mesh characteristics. For 3D unstructured meshes it can be defined as

$$L_s = \sqrt[3]{V_e} \tag{6.30}$$

where V_e is the element volume. It follows from Fig. 6.2(b) that

$$G_f = L_s \left(\frac{1}{2} f_d \varepsilon^f \right) \qquad \text{or} \qquad \varepsilon^f = \frac{2G_f}{L_s f_d} \tag{6.31}$$

Clearly, while the fracture energy is a material property independent of mesh, the failure strain depends on the smearing distance and thus the mesh characteristics.

For individual failure modes the damage model requires at minimum

- Fracture energy G_f
- Maximum allowable stress (strength) f_d
- Crack band width - equivalent element length L_s

The constitutive law $(6.28)_1$ can be rewritten as

$$\sigma = (1 - \omega) E \varepsilon = E(\varepsilon - \varepsilon_c), \quad \varepsilon_c = \omega \varepsilon \tag{6.32}$$

where ω is termed the damage parameter which evolves from 0 (no damage) to 1 (complete failure). Evolution of this parameter for multi-directional loading is outlined next. We present two potential approaches formulated on the basis of either orthotropic or standard isotropic damage model.

6.2.1 Orthotropic damage model

Given the orthotropic character of unidirectional composites we associate with each principal direction of the material symmetry, recall Fig. 5.2, an independent damage parameter $\omega_i, i = 1,2,3$ $(1 \equiv z, 2 \equiv x, 3 \equiv y)$

- $\omega_1 = \max(d_{1T}, d_{1C})$
- $\omega_2 = \max(d_{2T}, d_{2C})$
- $\omega_3 = \max(d_{3T}, d_{3C})$

where six damage parameters $d_{1T}, d_{1C}, d_{2T}, d_{2C}, d_{3T}, d_{3C}$ are specified to further distinguish the failure in tension (T) and compression (C). Following (Fang et al., 2009) we assume their evolution in terms of an equivalent displacement χ_{eq} in the form

$$d_J = 1 - \frac{\chi_{eq}^{Ji}(\chi_{eq}^{Jf} - \chi_{eq}^{J})}{\chi_{eq}^{J}(\chi_{eq}^{Jf} - \chi_{eq}^{Ji})}, \qquad J = 1T, 1C, 2T, 2C, 3T, 3C \tag{6.33}$$

where χ_{eq}^{J} depends on a given failure mode J. The value of equivalent displacement at the onset of damage χ_{eq}^{Ji} is estimated from the value of χ_{eq}^{J} calculated at the first load increment as

$$\chi_{eq}^{Ji} = \frac{\chi_{eq}^{J}}{\sqrt{F_J}} \tag{6.34}$$

where F_J is the J^{th} failure criterion, recall the maximum stress criteria (6.18) as one particular example. The maximum equivalent displacement χ_{eq}^{Jf} at failure associated with the failure strain ε^f follows from Eq. $(6.31)_2$ as

$$\chi_{eq}^{Jf} = \varepsilon^{Jf} L_s = \frac{2G_f^J}{\sigma_{eq}^{Ji}}, \qquad \sigma_{eq}^{Ji} = \frac{\sigma_{eq}^{J}}{\sqrt{F_J}} \tag{6.35}$$

where the equivalent stress σ_{eq}^{J} is found from the elastic energy pertinent to a given failure mode scaled by the associated equivalent displacement χ_{eq}^{J}. Both values are again defined at the first load increment. The specific forms of χ_{eq}^{J} and σ_{eq}^{J} are available in (Fang et al., 2009) and for convenience summarized also in Table 6.1.

The underlying problem is nonlinear and requires iterations of the linearized system of equations. To improve the convergence of the numerical algorithm an artificial Duvaut-Lions model is adopted in the form

$$\frac{\mathrm{d}D_i}{\mathrm{d}t} = \frac{1}{\eta}(\omega_i - D_i) \tag{6.36}$$

Table 6.1: Equivalent displacements and stresses for different failure modes

Failure mode	χ_{eq}^{J}	σ_{eq}^{J}
$J=1T, \sigma_{zz}>0$	$\chi_{eq}^{1T}=L_s\left(\langle\varepsilon_{zz}\rangle^2+A\gamma_{xz}^2+A\gamma_{yz}^2\right)^{1/2}$	$L_s\left(\langle\sigma_{zz}\rangle\langle\varepsilon_{zz}\rangle+A\sigma_{xz}\gamma_{xz}+\sigma_{yz}\gamma_{yz}\right)/\chi_{eq}^{1T}$
$J=1C, \sigma_{zz}<0$	$\chi_{eq}^{1C}=L_s\langle-\varepsilon_{zz}\rangle$	$L_s\langle-\sigma_{zz}\rangle\langle-\varepsilon_{zz}\rangle/\chi_{eq}^{1C}$
$J=2T, \sigma_{xx}>0$	$\chi_{eq}^{2T}=L_s\left(\langle\varepsilon_{xx}\rangle^2+A\gamma_{xz}^2+A\gamma_{xy}^2\right)^{1/2}$	$L_s\left(\langle\sigma_{xx}\rangle\langle\varepsilon_{xx}\rangle+A\sigma_{xz}\gamma_{xz}+\sigma_{xy}\gamma_{xy}\right)/\chi_{eq}^{2T}$
$J=2C, \sigma_{xx}<0$	$\chi_{eq}^{2C}=L_s\langle-\varepsilon_{xx}\rangle$	$L_s\langle-\sigma_{xx}\rangle\langle-\varepsilon_{xx}\rangle/\chi_{eq}^{2C}$
$J=3T, \sigma_{yy}>0$	$\chi_{eq}^{3T}=L_s\left(\langle\varepsilon_{yy}\rangle^2+A\gamma_{xy}^2+A\gamma_{yz}^2\right)^{1/2}$	$L_s\left(\langle\sigma_{yy}\rangle\langle\varepsilon_{yy}\rangle+A\sigma_{xy}\gamma_{xy}+\sigma_{yz}\gamma_{yz}\right)/\chi_{eq}^{3T}$
$J=3C, \sigma_{yy}<0$	$\chi_{eq}^{3C}=L_s\langle-\varepsilon_{yy}\rangle$	$L_s\langle-\sigma_{yy}\rangle\langle-\varepsilon_{yy}\rangle/\chi_{eq}^{3C}$

where η is the viscous parameter and D_i is the damped damage parameter. Considering a pseudo-time $t\in(0,1)$ we get

$$-\int_{D_i^k}^{D_i^{k+1}}\frac{1}{D_i-\omega_i}\,\mathrm{d}D_i=\int_{t^k}^{t^{k+1}}\frac{1}{\eta}\,\mathrm{d}t \tag{6.37}$$

so that

$$D_i^{k+1}=\omega_i-(\omega_i-D_i^k)\exp(-\Delta t/\eta) \tag{6.38}$$

The damage parameter D_i^{k+1} enters the current stiffness matrix $\mathbf{D}(D)$ at the beginning of the $k+1$ load increment. A relatively simple definition is provided in (Fang et al., 2009; Šmilauer et al., 2011) assuming a fixed crack orientation being aligned with a local material coordinate system. A more advanced formulation on the basis of the Murakami-Ohno damage model is provided, e.g., in (Fang et al., 2009; Zhou et al., 2013).

6.2.2 Isotropic damage model

Without loss of generality we briefly outline the formulation described in (Zhang et al., 2022) with reference to LaRC05 failure criterion described in Section 6.1.6. Therein, two independent damage variables are introduced for the fiber dominated ω_f and the matrix dominated ω_m modes, respectively. Unlike Eq. (6.33) the evolution of damage parameter is written directly in terms of strains (Donadon et al., 2009). For the matrix dominated mode it receives

the form

$$\omega_m = 1 - \frac{\varepsilon_m^0}{\varepsilon_{eq,m}} \left[1 + \kappa^2(2\kappa - 3)\right], \qquad \kappa = \frac{\varepsilon_{eq,m} - \varepsilon_m^0}{\varepsilon_m^f - \varepsilon_m^0} \tag{6.39}$$

where the equivalent strain $\varepsilon_{eq,m}$ is written in terms of strains $\varepsilon_n, \gamma_L, \gamma_T$ developed on the fracture plane as

$$\varepsilon_{eq,m} = \left(\langle\varepsilon_n\rangle^2 + \gamma_L^2 + \gamma_T^2\right)^{\frac{1}{2}} \tag{6.40}$$

At the onset of damage the equivalent strain is denoted as ε_m^0. The strain at complete separation ε_m^f follows for linear softening law from Eq. (6.31) where the strength f_d is replaced by an equivalent stress at the onset of failure

$$\sigma_m^0 = \left(\langle\sigma_n^0\rangle^2 + (\tau_L^0)^2 + (\tau_T^0)^2\right)^{\frac{1}{2}} \tag{6.41}$$

to get

$$\varepsilon_m^f = \frac{2G_{f,m}}{\sigma_m^0 L_s} \tag{6.42}$$

For the mixed mode failure scenario the fracture energy for the matrix dominated mode $G_{f,m}$ is provided by

$$G_{f,m} = G_{I,m}\left(\frac{\sigma_n^0}{\sigma_m^0}\right)^2 + G_{II,m}\left(\frac{(\tau_L^0)^2 + (\tau_T^0)^2}{(\sigma_m^0)^2}\right) \tag{6.43}$$

where G_I and G_{II} are the fracture energies for mode I and mode II fracture, respectively and $\sigma_n^0, \tau_L^0, \tau_T^0$ are tractions at the onset of failure, recall Section 6.1.6. Considering Eq. (6.32) the nominal tractions $\boldsymbol{t}$ are finally written in terms of effective tractions $\{\bar{t}\}^\mathsf{T} = \{\sigma_n, \tau_L, \tau_T\}$ as (Pinho et al., 2020)

$$\{\tilde{t}\}^\mathsf{T} = \left\{\left(1 - \omega_m \frac{\langle\sigma_n\rangle_+}{\sigma_n}\right)\sigma_n, (1-\omega_m)\,\tau_L, (1-\omega_m)\,\tau_T\right\} \tag{6.44}$$

For the fiber dominated mode the most simple case considers substitution of $\varepsilon_{eq,m}$ by the current strain in the fiber direction $\varepsilon_{L,T}, \varepsilon_{L,C}$ while distinguishing tension and compression. With analogy to Eq. (6.31) the strains at final failure are simply defined as

$$\varepsilon_{f,T}^f = \frac{2G_{f,T}}{T_L L_s}|\sigma_{zz} > 0, \qquad \varepsilon_{f,C}^f = \frac{2G_{f,C}}{C_L L_s}|\sigma_{zz} < 0 \tag{6.45}$$

The strains at the onset of failure correspond to the elastic threshold and are provided by

$$\varepsilon_{f,T}^0 = \frac{T_L}{E_L}|\sigma_{zz} > 0, \qquad \varepsilon_{f,C}^0 = \frac{C_L}{E_L}|\sigma_{zz} < 0 \tag{6.46}$$

where E_L is the effective longitudinal strain of the yarn.

The nominal stresses in the yarn coordinate system $\boldsymbol{\sigma}$ are finally provided by

$$\boldsymbol{\sigma} = (1 - \omega_f)\tilde{\boldsymbol{\sigma}} \tag{6.47}$$

where $\tilde{\boldsymbol{\sigma}}$ follows from Eq. (6.44) upon inverese transformation. Equation (6.47) suggests that fiber failure further contributes to damage evolution in the matrix, see (Zhang et al., 2022).

6.3 Strength properties of yarn from virtual tests

As no formulation of SEPUC for the polysiloxane matrix reinforced by basalt fibers is available we rely again on the representative volume element in terms of the PHA model. The volume fraction $c_f = 0.62$ is taken from literature (Vorel et al., 2015). The elastic stiffness properties of the fiber phase are provided in Table 5.3. The elastic properties of the ceramic matrix were again obtained from nanoindentation, recall Section 5.1.2. The corresponding results are stored in Table 6.2.

Table 6.2: Indentation results of pyrolyzed polysiloxane matrix

Position	**Red. mod.** E_r [GPa]	**Young's mod.** E [GPa]	**Hardness** H [GPa]	**Indentation depth** h_c [nm]
P127_2	67.57 ± 3.82	67.47 ± 3.61	7.29 ± 0.96	56.64 ± 4.25
P128_1	56.45 ± 3.77	55.95 ± 3.56	5.44 ± 0.44	110.65 ± 4.90
P128_2	60.20 ± 5.09	59.88 ± 4.82	6.01 ± 0.54	104.88 ± 5.21
P130_1	56.70 ± 8.53	56.22 ± 8.10	5.63 ± 1.02	109.81 ± 10.39
P130_2	58.39 ± 7.29	57.98 ± 6.91	5.68 ± 0.99	109.45 ± 11.72
P130_3	55.82 ± 5.00	55.30 ± 4.73	6.23 ± 1.08	103.85 ± 10.21
average	59.19 ± 5.58	58.83 ± 5.29	6.05 ± 0.84	99.21 ± 7.78

In the absence of our own experimental data on strength and fracture properties of individual phases we estimated the strength values from data available in literature while fracture energies where approximated using analogy with the carbon fibers. In particular, the value of the fiber tensile strength for basalt fibers manufactured by Kamenny Vec Co., Russia was reported in (Deàk and Czigány, 2009) together with elastic stiffness parameters being comparable measured by nanoindentation for the system considered in this work. The presented

value of $T_L^f = 2$GPa was, however, reduced to $T_L^f = 1$GPa owing to expected embrittlement caused by change of microstructure at elevated temperature (Černý et al., 2010) accompanied by visible flaws along the fiber direction. Point out that the stiffness properties provided in Table 5.3 correspond well to that presented in (Černý et al., 2008, 2010) for pyrolysis temperature of about 650°C. As basalt fibers are more or less amorphous we set the tensile strength in the transverse direction for both tension and compression to that in tension in the longitudinal direction. The tensile strength of the matrix $T_L^m = 1$MPa was back calculated from the strength of the composite at 650°C measured in (Černý et al., 2010) using a simple arithmetic rule of mixture. The fracture energies were estimated according to values reported in (Lu et al., 2013) for carbon fiber reinforced polymer. The fracture energy of the matrix was reduced from the proposed value of $G_f^m = 1.5$N/mm to $G_f^m = 1$N/mm as the pyrolyzed matrix becomes again more brittle during heat treatment. The fracture energy of the fiber phase equal to $G_f^f = 0.5$N/mm was approximated from that of the carbon fiber by assuming the same slope of the linear softening law. For convenience, the above mentioned values are summarized in Table 6.3.

Table 6.3: Strengths in [GPa] and fracture energy in [N/mm] of individual phases

Material	T_L	T_T	C_L	C_T	G_f
Basalt fiber	1.0	1.0	1.0	1.0	0.5
Pyrolyzed polysiloxane matrix	0.1	0.1	0.1	0.1	1

Being inspired by the results presented in (Krejčí et al., 2021) the orthotropic damage model from Section 6.2.1 is replaced at the level of individual phases by standard isotropic damage model. The local constitutive equation, recall Eq. (6.32), then read

$$\boldsymbol{\sigma}_r = (1 - \omega_r)\mathbf{L}_r\boldsymbol{\varepsilon}_r \tag{6.48}$$

where $r = f, m$ stands either for the matrix or fiber phase. Because using the SIFEL finite element code to run the numerical simulations we accept the implemented exponential traction separation law given by (Bažant and Oh, 1983)

$$\sigma = f_d \exp\left(-\frac{w_c^f}{w_c^0}\right) \tag{6.49}$$

where f_d is the tensile strength, w_c is the crack opening and w_c^0 is the parameter controlling the slope of the softening branch, see Fig. 6.3 and compare with the linear softening law in Fig. 6.2. For complex multidimensional stress/strain states, the strain ε in Eq. (6.32) may be

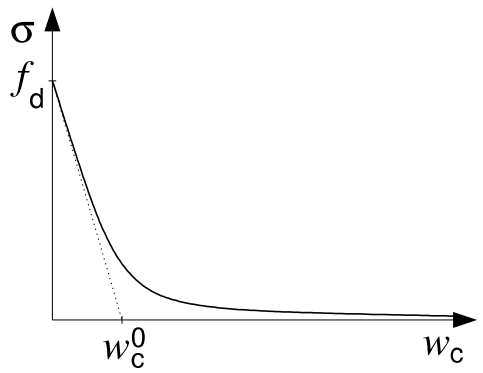

Figure 6.3: One-dimensional traction separation law

substituted by the Mazars equivalent strain κ provided by (Mazars, 1986)

$$\kappa = \sqrt{\sum_{\alpha=1}^{3} \langle \varepsilon_\alpha \rangle^2} \tag{6.50}$$

Combining Eq. (6.32) with Eqs. (6.28) and (6.49) and replacing the strain ε with the maximum equivalent strain in the loading history $\bar{\kappa}$ yields the resulting nonlinear equation to be solved for the damage parameter ω

$$(1-\omega)E\bar{\kappa} = f_d \exp\left(-\frac{\omega L_s \bar{\kappa}}{w_c^0}\right) \tag{6.51}$$

for states where $\bar{\kappa}$ exceeds the elastic threshold $\varepsilon^0 = f_d/E$, compare with Eq. (6.46). Unlike linear softening the strain at complete separation ε^f now becomes, compare with Eq. (6.31),

$$\varepsilon^f = \frac{w_c^0}{L_s} = \frac{G_f}{f_d L_s} \tag{6.52}$$

6.3.1 Numerical simulations of transverse tension

In this section we attempt to derive the fracture energy of the yarn associated with the fracture plane developed along the fiber direction. With reference to Eq. (6.43) we term this fracture energy $G_{I,m}$. For simplicity, the state of plane strain is assumed and the loading conditions

are limited to tension along the principal material directions x and y, recall Fig. 5.2. The results derived for a relatively coarse and fine finite element mesh in Fig. 6.4 are compared. The dimensions of the computational model in [mm] are $L_{\mathsf{PHA}} \times H_{\mathsf{PHA}} = 0.026 \times 0.015$. To this end, the stiffnesses and strengths are introduced in [MPa=N/mm^2] and fracture energy in [N/mm].

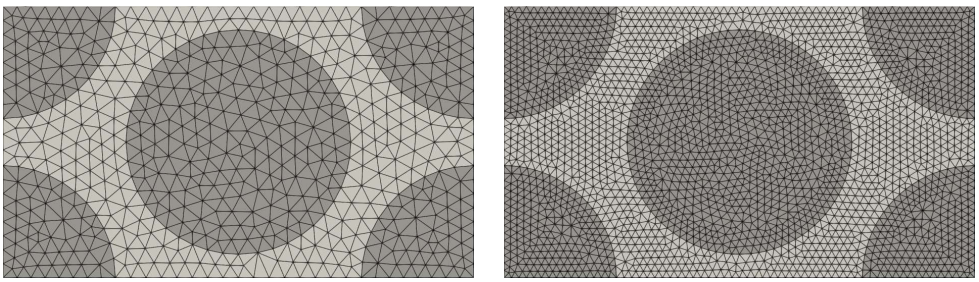

(a) (b)

Figure 6.4: Computational model: a) Coarse mesh, b) Fine mesh

Two types of loading conditions are considered. Pure strain-based loading exploited already in Chapter 5 is compared to so called mixed boundary conditions. The former case assumes that all components of the mesoscopic strain vector $\boldsymbol{E}$ are prescribed. The latter case allows for loading the composite in pure transverse tension by prescribing the selected strain and stress components of $\boldsymbol{E}$ and $\boldsymbol{\Sigma}$. For clarity, all loading scenarios are summarized in Table 6.4. Standard ordering $\boldsymbol{E}^{\mathsf{T}} = \{E_{xx}, E_{yy}, E_{xy}, 0\}$ and $\boldsymbol{\Sigma}^{\mathsf{T}} = \{\Sigma_{xx}, \Sigma_{yy}, \Sigma_{xy}, \Sigma_{zz}\}$ is adopted and $(\overline{a})$ stands for the prescribed strain or stress component.

Table 6.4: Loading conditions

Direction	Strain	Mixed
Tension along x	$\{\overline{E}_{xx}, 0, 0\}$	$\overline{E}_{xx} \neq 0, \overline{\Sigma}_{yy} = \overline{\Sigma}_{xy} = \overline{\Sigma}_{zz} = 0$
Tension along y	$\{0, \overline{E}_{yy}, 0\}$	$\overline{E}_{yy} \neq 0, \overline{\Sigma}_{xx} = \overline{\Sigma}_{xy} = \overline{\Sigma}_{zz} = 0$

The resulting values of fracture energies are presented independently for the matrix phase and the composite in Tables 6.5 and 6.6, respectively. The terms W^i and $G^i_{I,m}$ represent the energy density and fracture energy associated with the particular loading direction $i = x, y$.

While W^i represents the area under the stress-strain curves plotted in Figs. 6.5 and 6.6, the fracture energies were calculated for the homogeneous matrix as

$$G^x_{I,m} = \sqrt{A_{\mathsf{PHA}}} W^x, \qquad G^y_{I,m} = \sqrt{A_{\mathsf{PHA}}} W^y \tag{6.53}$$

where $A_{\mathsf{PHA}} = L_{\mathsf{PHA}} \times H_{\mathsf{PHA}}$, and for the composite as

$$G^x_{I,m} = L_{\mathsf{PHA}} W^x, \qquad G^y_{I,m} = H_{\mathsf{PHA}} W^y \tag{6.54}$$

thus smearing the localized damage over the size of the unit cell along the loading direction (Krejčí et al., 2021). The results are presented for two different finite element meshes, coarse and fine, to address its influence on numerical predictions.

Table 6.5: Matrix fracture energy from simulations

Loading	$\overline{E}_{xx}$				$\overline{E}_{yy}$			
type	Strain		Mixed		Strain		Mixed	
Parameter	W^x	$G^x_{I,m}$	W^x	$G^x_{I,m}$	W^y	$G^y_{I,m}$	W^y	$G^y_{I,m}$
units	[MPa]	[N/mm]	[MPa]	[N/mm]	[MPa]	[N/mm]	[MPa]	[N/mm]
Coarse mesh	65.6	1.30	93.7	1.85	114.8	2.26	130.8	2.58
Fine mesh	67.2	0	-	-	112.3	2.21	139.4	2.75

Table 6.6: Composite fracture energy from simulations

Loading	$\overline{E}_{xx}$				$\overline{E}_{yy}$			
type	Strain		Mixed		Strain		Mixed	
Parameter	W^x	$G^x_{I,m}$	W^x	$G^x_{I,m}$	W^y	$G^y_{I,m}$	W^y	$G^y_{I,m}$
units	[MPa]	[N/mm]	[MPa]	[N/mm]	[MPa]	[N/mm]	[MPa]	[N/mm]
Coarse mesh	59.9	1.56	59.9	1.56	109.5	1.64	121.3	1.82
Fine mesh	60.0	1.56	61.0	1.59	111.7	1.68	126.9	1.90

Table 6.5 stores the results for the matrix phase. Given the fact that strains and stresses are uniform over the analyzed domain one might wish to recover the constitutive model of the matrix phase. However, this expectation has not been met most probably due to mesh nonuniformity which caused the initial uniform distribution of the damage parameter ω to

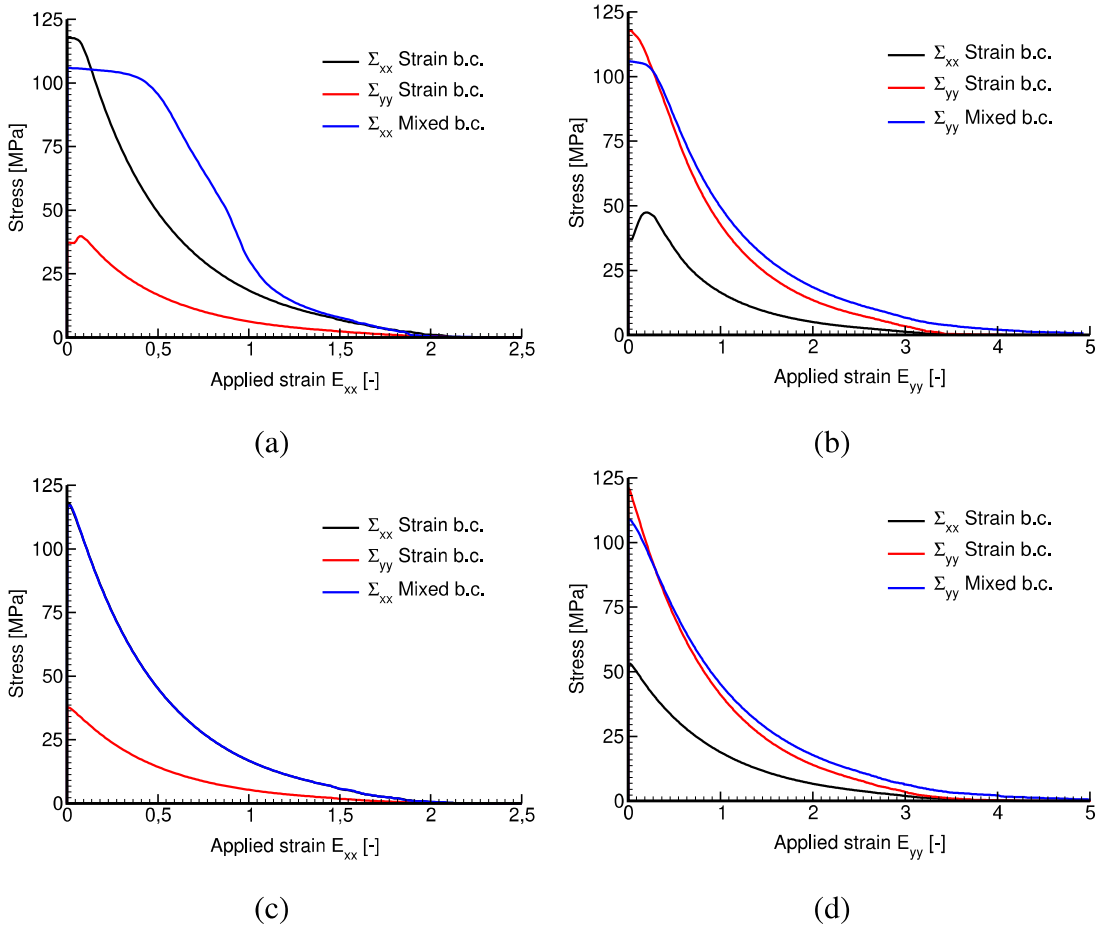

Figure 6.5: Mesoscopic stress-strain diagrams - coarse mesh: a) Homogeneous matrix $\overline{E}_{xx}$, b) Homogeneous matrix $\overline{E}_{yy}$, c) Composite $\overline{E}_{xx}$, d) Composite $\overline{E}_{yy}$

eventually localize into several narrow bands as seen in Figs. 6.7 - 6.8 for the coarse mesh and Figs. 6.11 - 6.12 for the fine mesh, respectively. As a result, both tensile strengths and fracture energies were overestimated, recall Table 6.3 and compared with the values in Table 6.5. Nevertheless, these predictions show only a mild dependency on the two selected meshes. As damage localization for the composite is more or less driven by the geometrical arrangement of fibers, we did not investigate this issue any further. However, what might seem important is the impact of boundary conditions resulting in a better estimate of the tensile strength for the Mixed type of boundary conditions seen in Figs. 6.5(a,b) and 6.6(a,b).

The results for the composite, PHA model, are summarized in Table 6.6. Given the evolution of damage parameter ω, see e.g. Figs. 6.9 and 6.10, one may suggest analogy

Table 6.7: Yarn strengths and fracture energies

Parameter	Strength [MPa]				Fracture energy [N/mm]		
notation	T_L	C_L	$T_x = C_x$	$T_y = C_y$	G_L	$G_x = G_m^x$	$G_y = G_m^y$
	1000	1000	118	107	0.5	1.59	1.90

with a running-bond masonry texture rotated by $90°$ with damage being localized into a bed joint, i.e. loading the PHA model along the x-direction, or a head joint when loading the PHA model in the y-direction. Unlike pure matrix, we observe, similar to (Krejčí et al., 2021), an insignificant influence of the applied boundary conditions, Strain or Mixed type. A noticeable difference in terms of mesoscopic stress-strain curves is evident only for the loading applied along the y-direction. Nevertheless, from the predicted values of fracture energies point of view this effect is negligible, recall Table 6.6. Furthermore, given the fiber strength being assumed $10\times$ the matrix strength, the influence of fibers appears only in their geometrical arrangement causing stronger obstacles and thus also higher values of fracture energies for loading along the y-direction. This is also evident from the evolution of localized damage in Figs. 6.9 - 6.10 for the course mesh and Figs. 6.13 - 6.14 for the fine mesh, respectively.

The resulting parameters that would enter, e.g., the orthotropic damage model of the yarn presented in Section 6.2.1 are summarized in Table 6.7. The results derived from Mixed boundary conditions are preferred. The tensile strengths are taken from the mesoscopic stress-strain curves in Figs. 6.6(c,d). It is further assumed that in the transverse direction the response in tension and compression is identical. Similar to masonry, the strength in the transverse direction is comparable to that of the matrix. The fracture energies $G_m^{x,y}$ would be used to estimate the equivalent displacement at failure χ_{eq}^{Jf} in Eq. (6.33). Finally point out that the yarn properties along the fiber direction are assumed the same as for the fiber in the longitudinal direction $L \equiv z$.

For the sake of completness we present the effective eleastic properties of the present system (basalt fibers/pyrolyzed polysiloxane matrix) derived from plane strain numerical homogenization, recall Section 3.1, in Table 6.8.

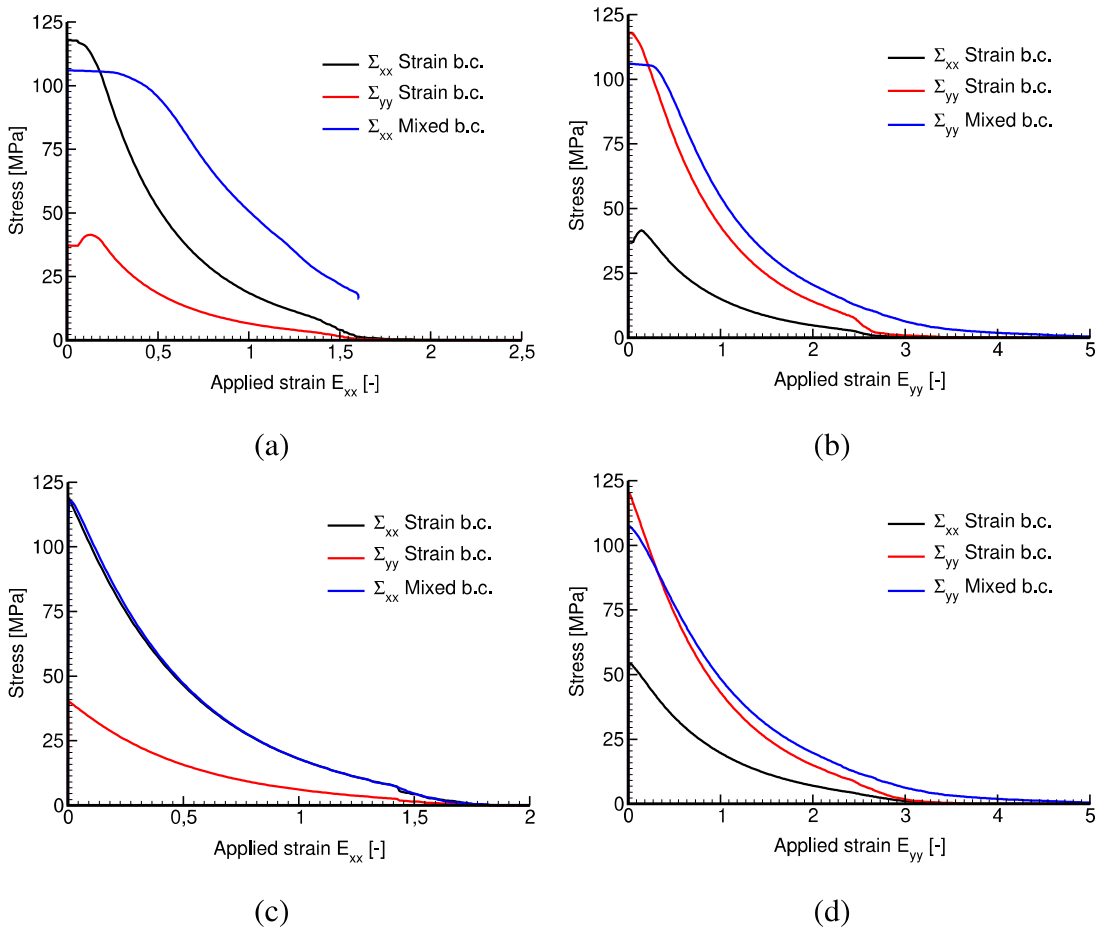

Figure 6.6: Mesoscopic stress-strain diagrams - fine mesh: a) Homogeneous matrix $\overline{E}_{xx}$, b) Homogeneous matrix $\overline{E}_{yy}$, c) Composite $\overline{E}_{xx}$, d) Composite $\overline{E}_{yy}$

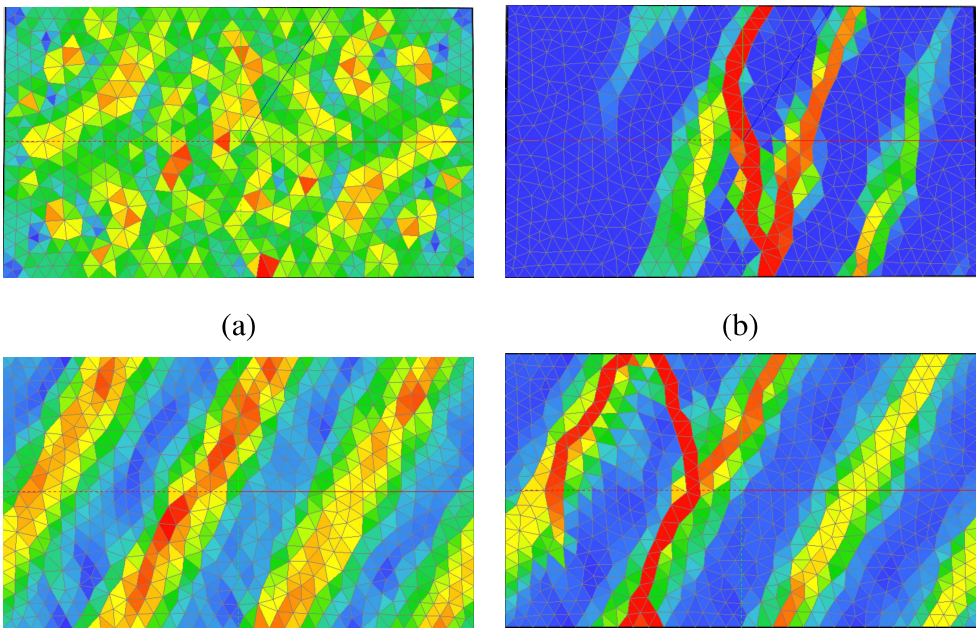

(a) (b)

(c) (d)

Figure 6.7: Evolution of ω in homogeneous matrix - coarse mesh, (a-b) Strain bc, (c-d) Mixed bc: a) $\overline{E}_{xx} = 0.003$, b) $\overline{E}_{xx} = 2.3$, c) $\overline{E}_{xx} = 0.02$, d) $\overline{E}_{xx} = 2.3$. At failure $0.992 < \omega \leq 1.0$

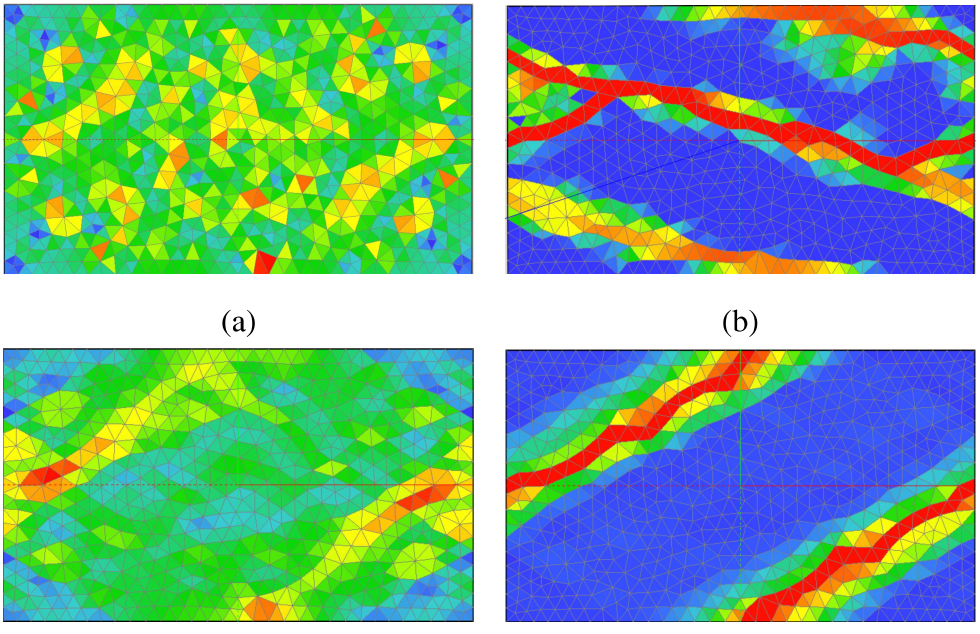

(a) (b)

(c) (d)

Figure 6.8: Evolution of ω in homogeneous matrix - coarse mesh, (a-b) Strain bc, (c-d) Mixed bc: a) $\overline{E}_{yy} = 0.002$, b) $\overline{E}_{yy} = 4.8$, c) $\overline{E}_{yy} = 0.15$, d) $\overline{E}_{yy} = 4.9$. At failure $0.989 < \omega \leq 1.0$

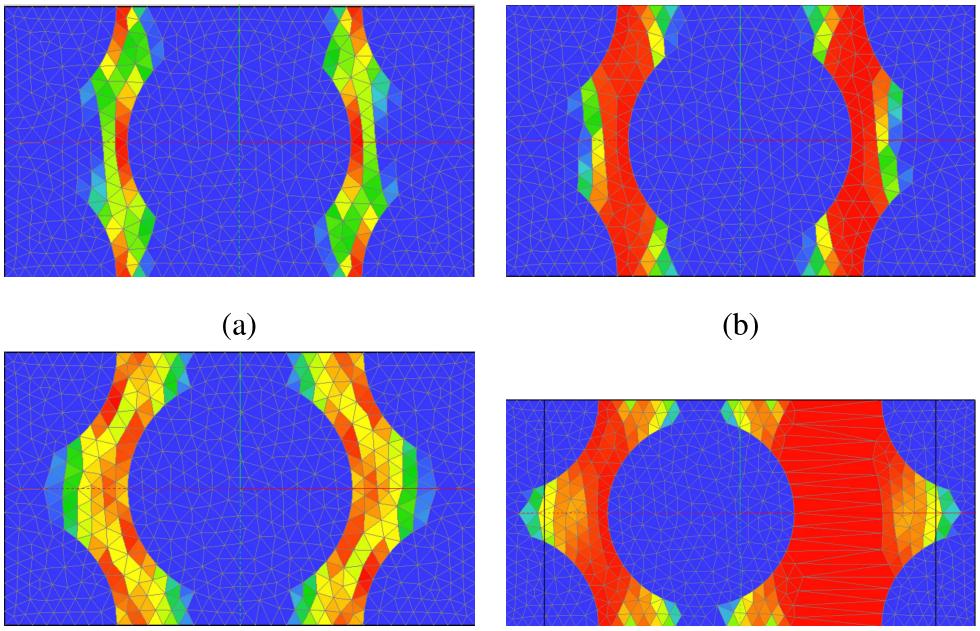

(a) (b)

(c) (d)

Figure 6.9: Evolution of ω in composite - coarse mesh, (a-b) Strain bc, (c-d) Mixed bc: a) $\overline{E}_{xx} = 0.003$, b) $\overline{E}_{xx} = 2.3$, c) $\overline{E}_{xx} = 0.002$, d) $\overline{E}_{xx} = 2.1$

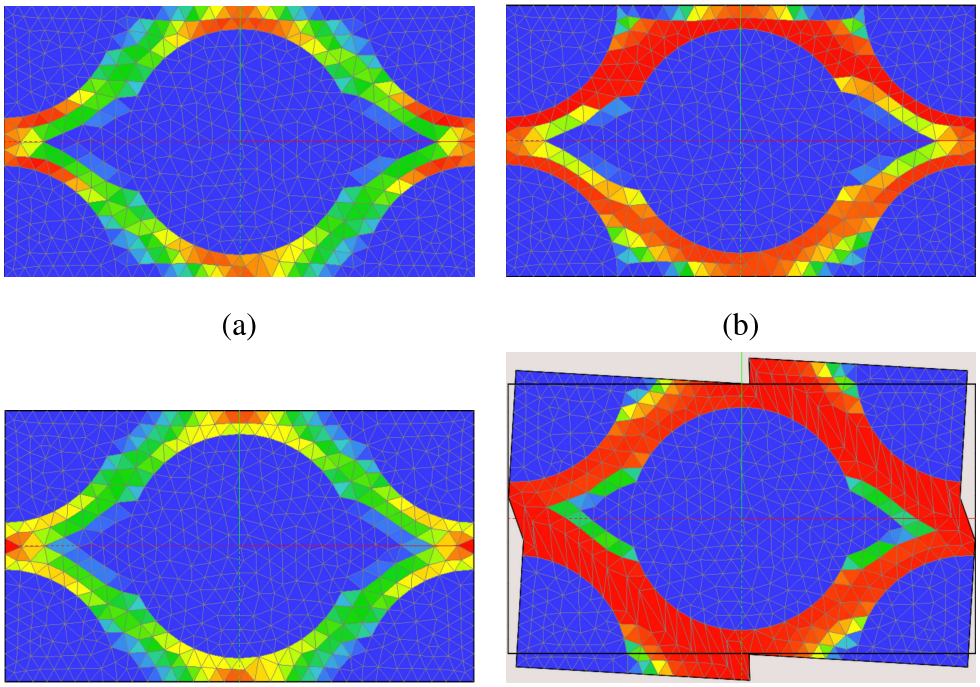

(a) (b)

(c) (d)

Figure 6.10: Evolution of ω in composite - coarse mesh, (a-b) Strain bc, (c-d) Mixed bc: a) $\overline{E}_{xx} = 0.002$, b) $\overline{E}_{xx} = 4.8$, c) $\overline{E}_{xx} = 0.002$, d) $\overline{E}_{xx} = 4.9$

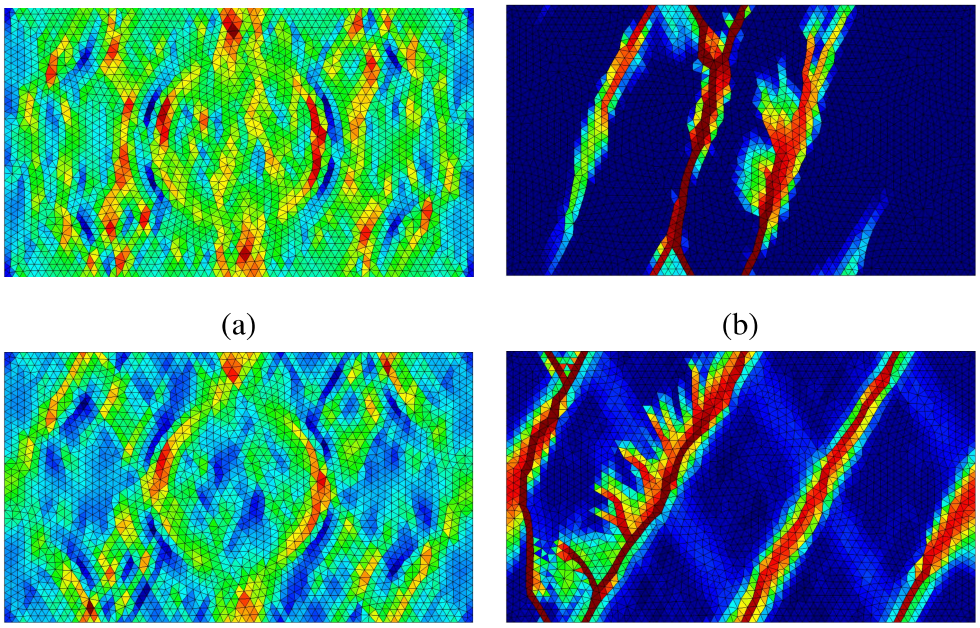

(a) (b)

(c) (d)

Figure 6.11: Evolution of ω in homogeneous matrix - fine mesh, (a-b) Strain bc, (c-d) Mixed bc: a) $\overline{E}_{xx} = 0.11$, b) $\overline{E}_{xx} = 1.7$, c) $\overline{E}_{xx} = 0.17$, d) $\overline{E}_{xx} = 1.6$. At failure $0.971 < \omega \leq 1.0$

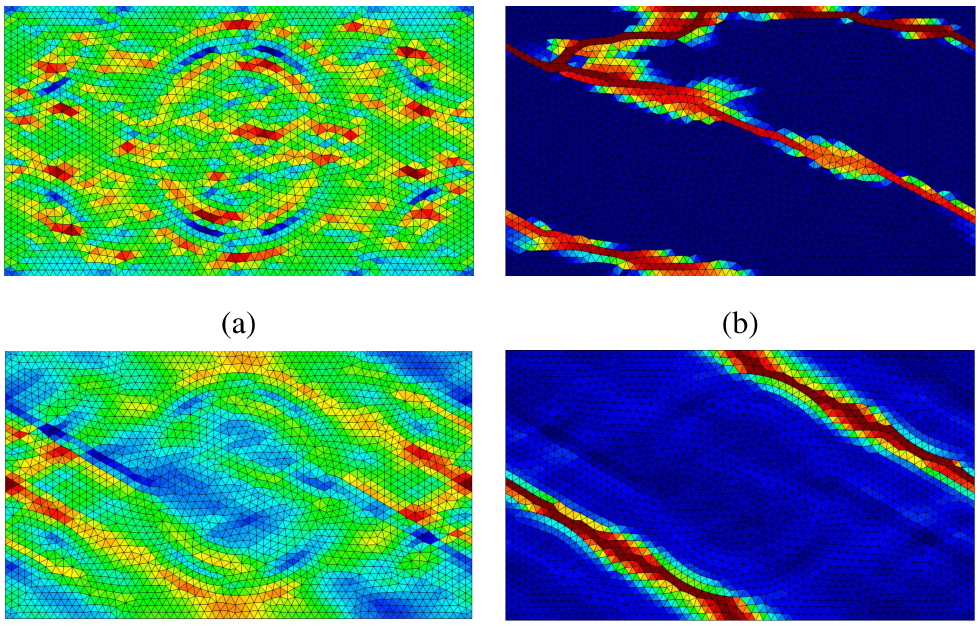

(a) (b)

(c) (d)

Figure 6.12: Evolution of ω in homogeneous matrix - fine mesh, (a-b) Strain bc, (c-d) Mixed bc: a) $\overline{E}_{yy} = 0.002$, b) $\overline{E}_{yy} = 4.8$, c) $\overline{E}_{yy} = 0.15$, d) $\overline{E}_{yy} = 4.9$. At failure $0.970 < \omega \leq 1.0$

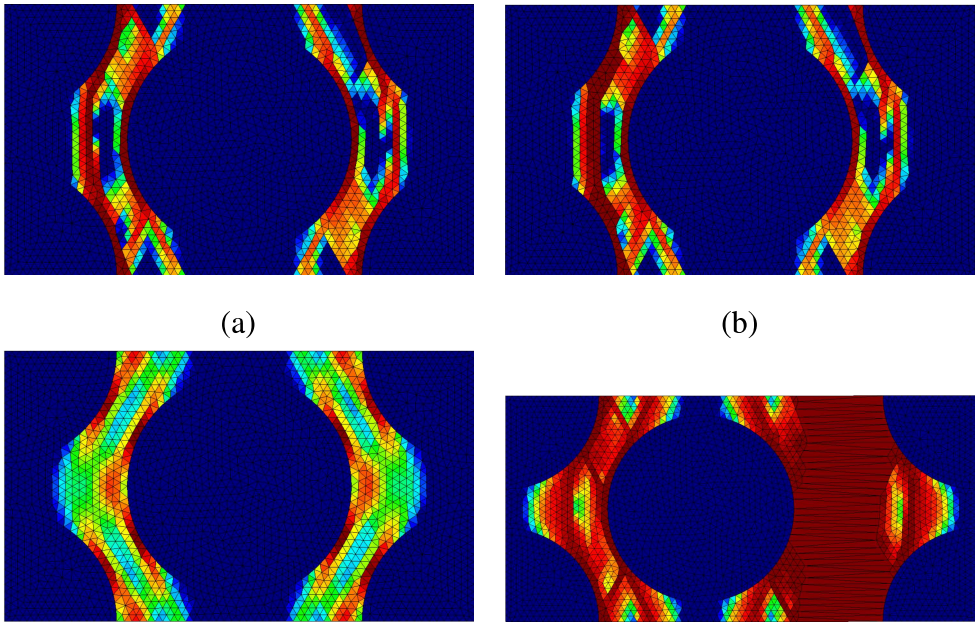

(a) (b)

(c) (d)

Figure 6.13: Evolution of ω in composite - fine mesh, (a-b) Strain bc, (c-d) Mixed bc: a) $\overline{E}_{xx} = 0.005$, b) $\overline{E}_{xx} = 1.8$, c) $\overline{E}_{xx} = 0.002$, d) $\overline{E}_{xx} = 1.9$

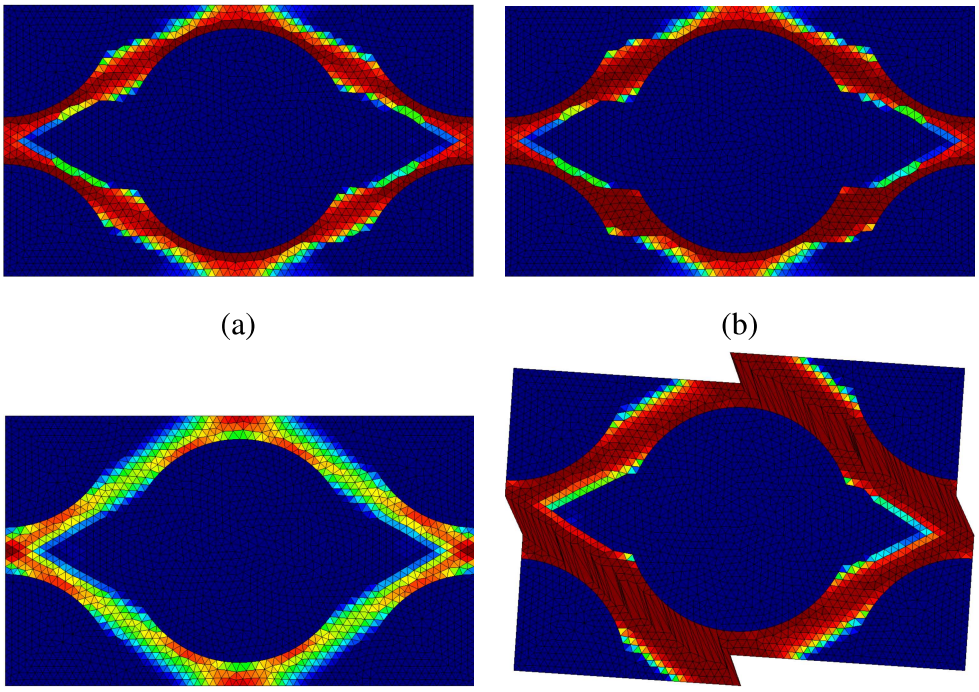

(a) (b)

(c) (d)

Figure 6.14: Evolution of ω in composite - fine mesh, (a-b) Strain bc, (c-d) Mixed bc: a) $\overline{E}_{xx} = 0.008$, b) $\overline{E}_{xx} = 3.4$, c) $\overline{E}_{xx} = 0.002$, d) $\overline{E}_{xx} = 5.1$

Table 6.8: Effective properties of unidirectional fibrous composite made of basal fibers embedded in pyrolyzed polysiloxane matrix. Elastic moduli are in [GPa]

E_L^{FEM}	E_T^{FEM}	G_T^{FEM}	ν_L^{FEM}
66.3	68.9	25.3	0.34

6.4 Numerical simulation at level of textile ply

Having derived the effective properties of the yarn, both elastic moduli (Table 6.8) and strengths and fracture energies (Table 6.7), we proceed in this section with an independent simulation at the level of textile ply. The computational model introduced already in Section 5.1, recall Fig. 5.3, is adopted. Attention is therefore limited again to balanced plain weave composites.

As this is still the work in progress, we accept several simplifications. In particular, the orthotropic damage model presented in Section 6.2.1 is adopted to describe the damage evolution in the yarn. The damage starts to propagate when one of the maximum stress criterion of the type (6.18) is exceeded. Similarly to the PHA model, the matrix response is assumed to be well represented by the isotropic damage model outlined in Section 6.3. Only the strain-based formulation is examined. Point out that this is the version being currently implemented in the SIFEL finite element code.

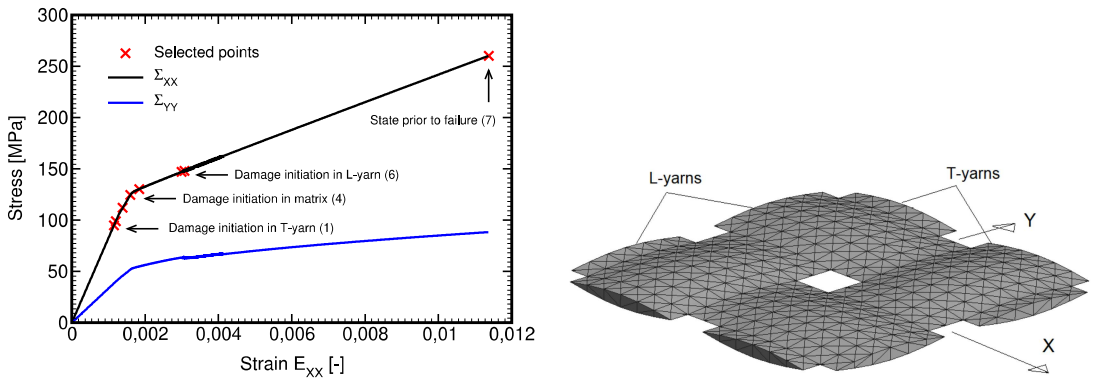

(a) (b)

Figure 6.15: a) Macroscopic stress-strain curve, b) Identification of individual yarns with respect to the ply coordinate system

For the sake of illustration the ply is loaded by the prescribed macroscopic strain E_{XX} while other strain components vanish. As plotted in Fig. 6.15(a), such constraints generate both Σ_{XX} and Σ_{YY} macroscopic stress components. Notice that because of the yarn undulation the X-axis does not fully agree, for the yarn predominantly aligned with this direction, with the longitudinal (L) direction of the straight yarn, while for the two transverse directions it is evident from Fig. 5.2 that $Y \equiv x, Z \equiv y$. On the contrary, the yarn aligned with the Y-axis is, for the prescribed loading ($E_{xx} \neq 0$), merely stressed in the transverse direction of the yarn thus having the elastic limit equal to the tensile strength T_x in Table 6.7. This becomes evident from surface plots of the current state of damage in Figs. 6.16 - 6.21. These figures can be identified with the points marked by a red cross in the macroscopic stress-strain curve 6.15(a), so a gradual evolution of damage within a textile ply can be easily monitored. All axonometric projections correspond to the schematic drawing in Fig. 6.15(b). For simplicity, the yarns aligned with the X-axis will be, henceforth, denoted as L-yarns while those aligned with the Y-axis will be denoted as T-yarns. This figure also suggests a relatively coarse mesh (14394 4-node constant strain tetrahedrons) used in simulations.

Figure 6.16 shows that damage initiates in T-yarns by reaching the transverse tensile stress T_x ($\sigma_{XX}^{\mathrm{T-yarn}} = T_x$) and gradually evolves with increasing tensile strain E_{XX}, see also Fig. 6.15(a). This is manifested by a nonzero damage parameter ω_2 which for T-yarns coincides with the local x axis, i.e. $x = X$, recall Fig. 5.2. At some specific value of E_{XX} the tensile strength in the matrix is exceeded which triggers the damage evolution in the matrix, see Figs. 6.15(a) and 6.17(b). The damage in the L-yarns is observed last caused again by transverse stresses reaching the transverse tensile strength T_x ($\sigma_{YY}^{\mathrm{L-yarn}} = T_x$), see Figs. 6.15(a) and 6.19(a). Figure 6.21 shows the state prior to collapse. As indicated in Fig. 6.22(a) this is the state when the tensile stress in the L-yarns approaches in majority of elements the longitudinal tensile strength T_L ($\sigma_{XX}^{\mathrm{L-yarn}} \to T_L$), i.e. the principal stress $\sigma_1^{\mathrm{L-yarn}} = T_L$. However, the program failed to provide an evolution of damage parameter ω_1 passing this state. This is attributed to relatively large elements which in combination with large tensile strength $T_L = 1000$ MPa and small fracture energy $G_L = 0.5$ N/mm would lead to snap-back. Thus to proceed with the analysis would require much finer mesh. On the contrary, given the parameters of basalt fibers an essentially brittle failure can be expected, so the maximum achieved tensile stress $\Sigma_{XX} \approx 250$ MPa can be identified with the tensile strength

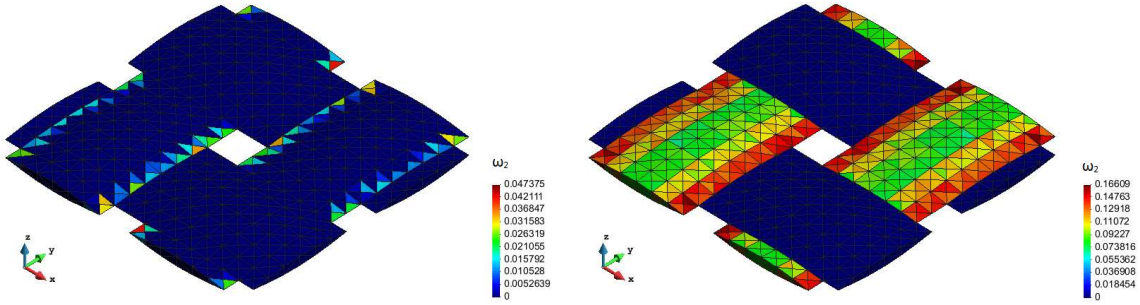

(a) (b)

Figure 6.16: Initiation of damage in T-yarns - distribution of ω_2 corresponding to points 2 and 3 in Fig. 6.15(a): a) Point 2 b) Point 3

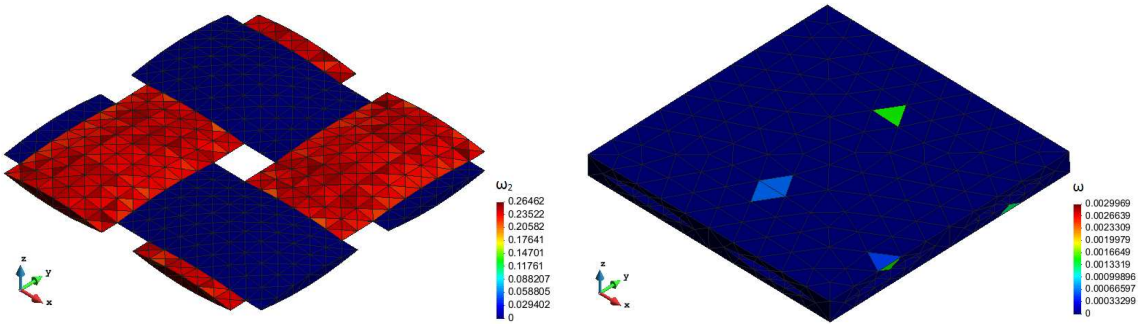

(a) (b)

Figure 6.17: Initiation of damage in matrix, point 4 in Fig. 6.15(a): a) Distribution of ω_2 in yarns, b) Distribution of ω in matrix

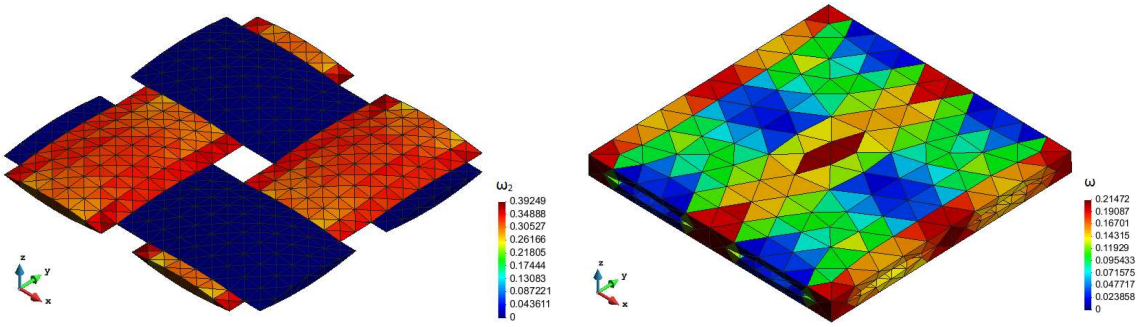

(a) (b)

Figure 6.18: Point 5 in Fig. 6.15(a): a) Distribution of ω_2 in yarns, b) Distribution of ω in matrix

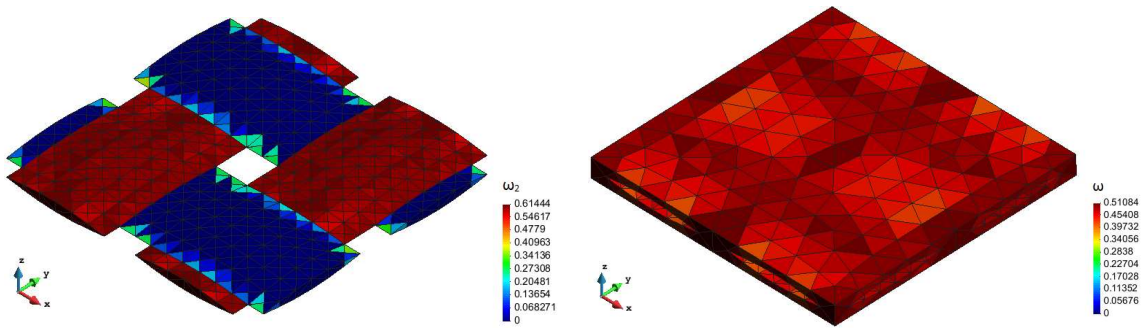

(a) (b)

Figure 6.19: Initiation of damage in L-yarns, point 6 in Fig. 6.15(a): a) Distribution of ω_2 in yarns, b) Distribution of ω in matrix

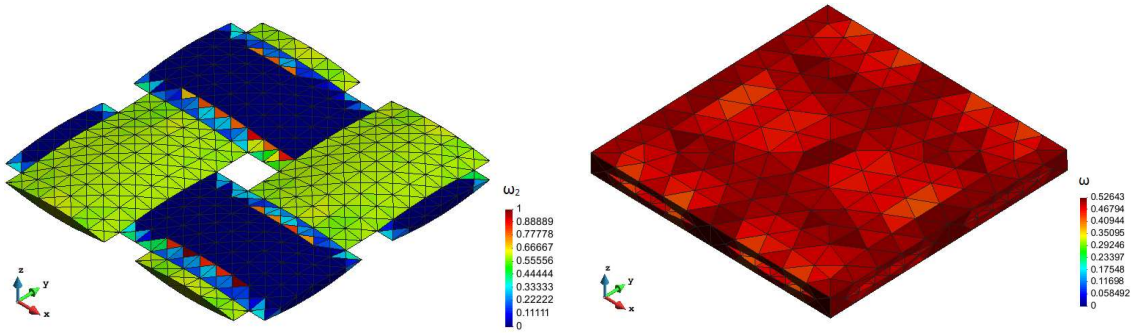

(a) (b)

Figure 6.20: Point 7 in Fig. 6.15(a): a) Distribution of ω_2 in yarns, b) Distribution of ω in matrix

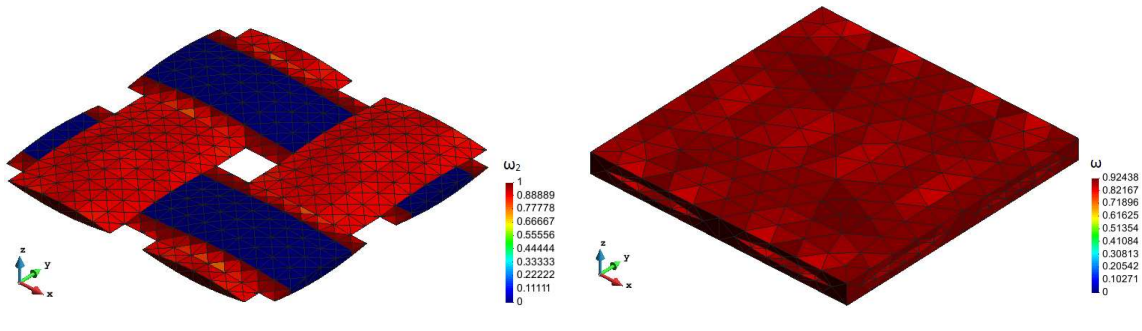

(a) (b)

Figure 6.21: State prior to collapse, point 8 in Fig. 6.15(a): a) Distribution of ω_2 in yarns, b) Distribution of ω in matrix

of a given textile ply. Unfortunately, no experimental data are currently available to validate this numerical prediction. So at minimum, an independent verification against other type of numerical implementation, e.g. based on the damage model described in Section 6.2.2, is needed.

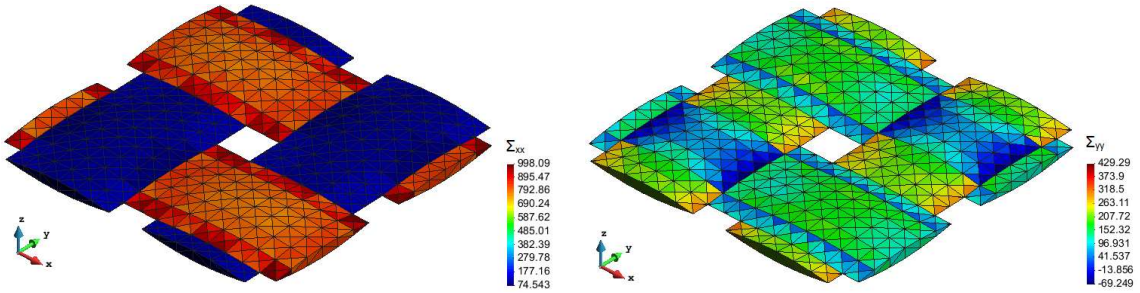

(a) (b)

Figure 6.22: State prior to collapse, distribution of macroscopic stresses in [MPa]: a) Stress Σ_{XX}, b) Stress Σ_{YY}

To show that the implemented orthotropic damage model is capable of tracking the descending branch of the macroscopic stress-strain curve we run the same numerical experiment with adjusted longitudinal parameters $T_L = 150$ MPa and $G_L = 1.5$ N/m, thus being closer to those used for the transverse directions. The resulting macroscopic stress-strain curves are plotted in Fig. 6.23 for illustration.

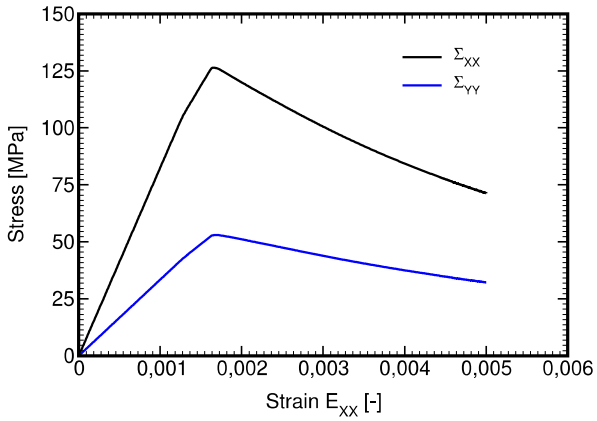

Figure 6.23: Macroscopic stress-strain curve with modified longitudinal tensile strength $T_L = 150$MPa and fracture energy of basalt fibers $G_L = 1.5$ N/mm

Point out that similarly to scalar damage parameter ω the formulation of orthotropic damage parameters ω_i is local so some mesh dependency can be expected. But this goes beyond the scope of the present thesis.

Chapter 7

CONCLUSIONS

Two distinct approaches to the modeling of polymer matrix based plain weave textile composites are proposed and thoroughly discussed. A considerable effort is devoted to the modeling of rate dependent nonlinear viscoelastic response of the selected polymer matrices. Both advanced and ordinary epoxy resins are examined to address a relatively wide range of applications of the composites reinforced by either carbon or basalt textile fabrics. Because transition from a viscous to a brittle behavior can be encountered depending on the rate of loading, a suitable constitutive model that allows for a gradual evolution of failure in the framework of continuum damage mechanics is also studied. While the latter approach builds exclusively on the application of the finite element method (FEM) within the first order homogenization theory, the former approach attempts to replace the often tedious finite element simulations by considerably more efficient Mori-Tanaka (MT) method based micromechanical model combined with the transformation field analysis to account for viscous effects.

The nonlinear rate dependent response of polymer matrices observed experimentally is presented in light of the generalized Leonov model. A complex experimental program combining both standard tensile tests performed at different strain rates and creep tests carried out at different stress levels was executed to provide data for model calibration as well as for validation of its numerical implementation. A suitable optimization procedure was proposed to calibrate the model purely on the bases of creep tests. The calibrated model was finally tested by comparing the experimental data with the results obtained computationally. While for advanced L285 epoxy resin the application of the Leonov model appears satisfactory, it seems less suitable for the description of the ordinary E455 epoxy resin. This, however, might be caused by the deficiency of the obtained experimental results. Therefore, another set of experiments is currently under way to shed a light on the applicability of the Leonov model to E455 polymer matrix.

The performance of the two matrices as a bonding phase in unidirectional fibrous composite was examined only computationally. In this regard, attention was accorded mainly to the application of the Mori-Tanaka method. To appreciate the viscous effects the loading

conditions were limited to in-plane shear. This also enabled a direct comparison with the result provided by finite element simulations derived under plane strain conditions to reduce the computational burden. Implementation of the Mori-Tanaka method into finite element code was, however, first verified for a homogeneous matrix showing a perfect agreement with FEM simulations. On the contrary, a considerable difference between MT and FEM predictions was observed for a composite identifying the main drawback of the two-point averaging MT method that assumes piecewise uniform strain and stress fields in the two phases, which in turn does not enable to address a potential localization of inelastic strains in the matrix. It should be mentioned that the major difference was encountered when representing the actual random microstructure with the periodic hexagonal array (PHA) model (Teplý and Dvorak, 1988). Such a representation of statistically uniform microstructure is often the choice when the volume fraction of fibers is sufficiently large as was also the case in the present study. Proceeding in the footsteps of (Valenta, 2011) we introduced a damage like model reducing the stresses in the fiber phase. The original formulation was slightly modified but the dependency of the damage parameter ω on the current value of the equivalent deviatoric stress τ_{eq} was preserved. Such a simple modification to the standard MT method allowed us to arrive at reasonable agreement with the FEM predictions particularly in terms of the homogenized response. Its applicability is, however, limited to particular loading conditions and fails when loading the composite at a strain rate differing from that used in the model calibration. To this end, a new formulation was proposed where the damage parameter ω was assumed to evolve with strain. For pure shear loading, this step considerably eliminated the strain rate dependency. However, whether this model will successfully cover other loading scenarios is still an opened issue.

Being inspired by (Tiberti and Milani, 2020) the influence of random microstructure was further explored. The study grounded on an ensemble of representative volume elements (RVE) of variable complexity extracted directly from a large image of actual microstructure. Although not periodic in terms of microstructure the periodic boundary conditions were adopted when running the FEM simulations. Interestingly, no convergence with increasing size of the computational model was identified. Instead, all predictions were bounded by the results corresponding to the computational models experiencing the lowest and the largest elastic stiffness. Surprisingly, the predictions derived from the application of the PHA model

to all material systems were found well below the results provided by irregular RVEs. In light of this the MT method with on adjustments appears quite satisfactory especially for carbon fibers. Whether to completely abandon the PHA model and concentrate instead on more complex, potentially, also more reliable statistically equivalent periodic unit cells as proposed, e.g., in (Zeman and Šejnoha, 2001) is, however, an opened issue which goes beyond the scope of the present work.

With the above results in mind the multiscale analysis at the level of textile ply was performed assuming standard setting of the MT method. Unfortunately, there are no experimental results available for the analyzed systems. The present work is therefore only computational. The reliability of the implementation of the MT method in the context of a fully coupled multiscale analysis is therefore jugged only on the bases of the predicted macroscopic response with reference to the property of the generalized Leonov model.

Seemingly unrelated with the previous discussion is the last topic addressed in this work. Nevertheless, the ultimate goal is to combine the damage model with viscoelasticity. However, this must be preceded by assuring a correct implementation of the damage model itself. As this is a work in progress, we admit only time independent effects. Two approaches based either on an orthotropic damage model or an isotropic damage model for the description of the yarn response are subjected to investigation, where the former one has already been implemented into SIFEL finite element code and is being currently tested. Its use requires, apart from effective elastic stiffnesses, the knowledge of effective strengths and fracture energies. We expect these quantities to be derived from an independent computational homogenization step, a virtual experiment, performed at the level of yarn. To be consistent with most of the previous calculations, we adopted again the PHA model. With reference to (Krejčí et al., 2021) the isotropic damage model was used for both phases although the fiber phase, given its considerably higher strength in comparison to the matrix, remained elastic throughout the analysis and thus influenced the damage localization only. The influence of mesh refinement was tested resulting in negligible differences in the predicted macroscopic properties thus promoting even a local implementation of the model. What might seem more important is the application of particular loading conditions. To that end, both strain based and mixed loading conditions were examined. Although for a given geometry a noticeable difference was identified for loading along the Y direction only, we prefer the mixed loading condi-

tions as they better represent what we would expect experimentally. The final simulations performed at the level of textile ply proved applicability of the model to properly address the damage processes taken place in individual phases. Further validation against some experimental data or at least verification against other formulations available in literature is, however, still needed. This research effort is being currently pursued.

It is seen from above that there is still a number of open issues even for this specific class of material systems. It can therefore be expected that the field of composites will remain an active field of research in many years to come.

BIBLIOGRAPHY

Artemenko, S. (2003). Polymer composite materials made from carbon, basalt, and glass fibres. structure and properties. *Fibre Chemistry*, 35:226–229.

Barral, M., Chatzigeorgiou, G., Meraghni, F., and Léon, R. (2020). Homogenization using modified Mori-Tanaka and TFA framework for elastoplastic-viscoelastic-viscoplastic composites: Theory and numerical validation. *International Journal of Plasticity*, 127:102632.

Bažant, Z. P. and Oh, B. H. (1983). Crack band theory for fracture of concrete. *Materials and Structures*, 16:155–177.

Benveniste, Y. (1987). A new approach to the application of Mori-Tanaka theory in composite materials. *Mechanics of Materials*, 6:147–157.

Bittnar, Z. and Šejnoha, J. (1996). *Numerical methods in structural engineering*. ASCE Press.

Černý, M., Glogar, P., Goliáš, V., Hruška, J., Jakeš, P., Sucharda, Z., and Vávrová, I. (2007). Comparison of mechanical properties and structural changes of continuous basalt and glass fibres at elevated temperatures. *Ceramics-Silikáty*, 51(2):82–88.

Chairman, C. A. and Kumaresh Babu, S. P. (2013). Mechanical and abrasive wear behavior of glass and basalt fabric-reinforced epoxy composites. *Journal of Applied Polymer Science*, 130(1):120–130.

Chand, S. (2000). Carbon fibers for composites. *Journal of Materials Science*, 35:1303–1313.

Cherif, C. (2016). *Textile Materials for Lightweight Constructions*. Springer-Verlag, Berlin.

Christensen, R. M. (2008). *Failure theory for materials science and engineering*. http://www.failurecriteria.com.

Christensen, R. M. (2013). *The theory of materials failure*. Oxford University Press.

Chua, C. Y. X., Liu, H.-C., Di Trani, N., Susnjar, A., Ho, J., Scorrano, G., Rhudy, J., Sizovs, A., Lolli, G., Hernandez, N., Nucci, M. C., Cicalo, R., Ferrari, M., and Grattoni, A. (2021). Carbon fiber reinforced polymers for implantable medical devices. *Biomaterials*, 271:120719.

Czigány, T., Vad, J., and Pölöskei, K. (2005). Basalt fiber as a reinforcement of polymer composites. *Periodica Polytechnica Mechanical Engineering*, 49(1):3–14.

Dalinkevich, A. A., Gumargalieva, K. Z., Marakhovsky, S. S., and Soukhanov, A. V. (2009). Modern basalt fibrous materials and basalt fiber-based polymeric composites. *Journal of Natural Fibers*, pages 248–271.

Das, S. (2011). Life cycle assessment of carbon fiber-reinforced polymer composites. *The International Journal of Life Cycle Assessment*, 16:268–282.

Davila, C. G., Camanho, P. P., and Rose, C. A. (2005). Failure criteria for frp laminates. *Journal of Composite Materials*, 39(4):323–345.

de la Rosa García, P., Escamilla, A. C., and Nieves González García, M. (2013). Bending reinforcement of timber beams with composite carbon fiber and basalt fiber materials. *Composites Part B: Engineering*, 55:528–536.

Deàk, T. and Czigány, T. (2009). Chemical Composition and Mechanical Properties of Basalt and Glass Fibers: A Comparison. *Textile Research Journal*, 79(7):645–651.

Dhand, V., Mittal, G., Rhee, K. Y., Park, S.-J., and Hui, D. (2015). A short review on basalt fiber reinforced polymer composites. *Composites: Part B*, 73:166–180.

Donadon, A., de Almeida, S., Arbelo, M., and de Faria, A. (2009). A three-dimensional ply failure model for composite structures. *International Journal of Aerospace Engineering*, 2009:486063.

Donnet, J.-B. and Bansal, R. C. (1998). *Carbon fibers*. Crc Press.

Dorigato, A. and Pegoretti, A. (2012). Fatigue resistance of basalt fibers-reinforced laminates. *Journal of Composite Materials*, 46(15):1773–1785.

Dvorak, G. (2013). *Micromechanics of composite materials*. Springer Dordrecht Heidelberg New York London.

Dvorak, G. J. and Benveniste, Y. (1992). On transformation strains and uniform fields in multiphase elastic media. *Proceedings of the Royal Society of London Series A - Mathematical, Physical and Engineering Sciences*, 437(1900):291–310.

Eshelby, J. D. (1957). The determination of the elastic field of an ellipsoidal inclusion and related problems. *Proceeding of Royal Society, Series A*, 241:376–396.

Fang, G., Jun, L., Lu, Q., Wang, B., and Y., W. (2011). Investigation on the compressive properties of the three dimensional four-directional braided composites. *Computers and Structures*, 93:392–405.

Fang, G., Jun, L., and Wang, B. (2009). Progressive damage and nonlinear analysis of 3D four-directional braided composite under unidirectional tension. *Computers and Structures*, 89:126–133.

Fiore, V., Scalici, T., Di Bella, G., and Valenza, A. (2015). A review on basalt fibre and its composites. *Composites Part B: Engineering*, 74:74–94.

Frank, E., Steudle, L. M., Ingildeev, D., Spörl, J. M., and Buchmeiser, M. R. (2014). Carbon fibers: Precursor systems, processing, structure, and properties. *Angewandte Chemie - International Edition, 53(21)*.

Grégr, J. (2004). Povrchové vlastnosti uhlíkových vláken.

Hao, L. and Yu, W. (2011). Comparison of thermal protective performance of aluminized fabrics of basalt fiber and glass fiber. *Fire and materials*, 35(8):553–560.

Hao, L. C. and Yu, W. D. (2010). Evaluation of thermal protective performance of basalt fiber nonwoven fabrics. *Journal of Thermal Analysis and Calorimetry*, 100:551–555.

Hashin, Z. (1980). Failure criteria for unidirectional fiber composites. *Journal of Applied Mechanics*, 46:329–334.

Hertz, H. (1882). On the contact of rigid elastic solids, (original: Über die berührung fester elastischer körper), chap. 6. *Ch. 6: Miscellaneous Papers*, pages 156–171.

Hill, R. (1963). Elastic properties of reinforced solids: some theoretical principles. *Journal of the Mechanics and Physics of Solids*, 11(5):357–372.

Hu, Y. and Liu, Y. (2010). 11 - high modulus, high tenacity yarns. In Alagirusamy, R. and Das, A., editors, *Technical Textile Yarns*, pages 329–386. Woodhead Publishing.

Huang, X. (2009). Fabrication and properties of carbon fibers. *Materials*, 2:2369–2403.

Hudec, J. (2013). Observing of properties of nanocomposite materials (sledování vlastností nanokompozitních materiálů. Master's thesis, Technical University in Brno.

Kořínek, Z. (2022). Kompozity. Available at `https://kompozity.webnode.cz/`.

Krejčí, T., Koudelka, T., Bernardo, V., and Šejnoha, M. (2021). Effective elastic and fracture properties of regular and irregular masonry from nonlinear homogenization. *Computers and Structures*, 254:106580.

Kunc, K. (2013). Implementace elasto-plastického modelu s degradací materiálových parametrů pro textilní kompozity do komerčního MKP softwaru. Master's thesis, University of West Bohemia, Faculty of Applied Science.

Leonov, A. I. (1976). Non-equilibrium thermodynamics and rheology of viscoelastic polymer media. *Rheol. Acta*, 15:85–98.

Lomov, S. V., Verpoest, I., Peeters, T., Roose, D., and Zako, M. (2003). Nesting in textile laminates: Geometrical modelling of the laminate. *Composites Science and Technology*, 63(7):993–1007.

Long, A. (2005). *Design and Manufacture of Textile Composites*. Woodhead Publishing Series in Textiles, Cambridge.

Lopresto, V., Leone, C., and De Iorio, I. (2011). Mechanical characterisation of basalt fibre reinforced plastic. *Composites Part B: Engineering*, 42(4):717–723.

Lu, Z., Xia, B., and Yang, Z. (2013). Investigation on the tensile properties of three-dimensional full five-directional braided composites. *Computational Material Science*, 77:445–455.

Lund, M. D. and Yue, Y.-Z. (2008). Influences of chemical aging on the surface morphology and crystallization behavior of basaltic glass fibers. *Journal of non-crystalline solids*, 354(12-13):1151–1154.

Mazars, J. (1986). A description of micro and macroscale damage of concrete structures. *International Journal of Fracture*, 25:729–737.

Michel, J. C., Moulinec, H., and Suquet, P. (1999). Effective properties of composite materials with periodic microstructure: A computational approach. *Computer Methods in Applied Mechanics and Engineering*, 172:109–143.

Minus, M. L. and Kumar, S. (2005). The processing, properties and structure of carbon fibers. *The Journal of The Minerals, Metals and Materials Society*, 57:52–58.

Molnár, J. (2017). Vliv vazby tkaniny na její komfortní vlastnosti. Master's thesis, Technical University of Liberec, Faculty of Textile Engineering.

Mori, T. and Tanaka, K. (1973). Average stress in matrix and average elastic energy of elastic materials with misfitting inclusions. *Acta Metallurgica*, 21:571.

Morova, N. (2013). Investigation of usability of basalt fibers in hot mix asphalt concrete. *Construction and Building Materials*, 47:175–180.

Nasir, V., Karimipour, H., Taheri-Behrooz, F., and Shokrieh, M. (2012). Corrosion behaviour and crack formation mechanism of basalt fibre in sulphuric acid. *Corrosion Science*, 64:1–7.

Novotná, J. (2021). Dielektrické vlastnosti epoxidových kompozitů plněných recyklovanými uhlíkovými vlákny. Master's thesis, Technical University of Liberec, Faculty of Textile Engineering, Czech Republic.

Oliver, W. and Phar, G. (2004). Measurement of hardness and elastic modulus by instrumented indentation: Advances in understanding and refinements to methodology. *Journal of Material Research*, 19(1):3–20.

Peijs, T., Kirschbaum, R., and Lemstra, P. J. (2022). A critical review of carbon fiber and related products from an industrial perspective. *Advanced Industrial and Engineering Polymer Research*.

Petersen, R. (2016). Carbon fiber biocompatibility for implants. *Fibers*, 4(1).

Pinho, S., Darvizeh, R., Robinson, P., Schuecker, C., and Camanho, P. (2020). Material and structural response of polymer-matrix fibre-reinforced composites. *Journal of composite materials*, 46(19-20):2313–2341.

Pinho, S., Iannucci, L., and Robinson, P. (2006a). Physically-based failure models and criteria for laminated fibre-reinforced composites with emphasis on fibre kinking: Part I: Development. *Composites Part A: Applied Science and Manufacturing*, 37(1):63–73.

Pinho, S., Iannucci, L., and Robinson, P. (2006b). Physically based failure models and criteria for laminated fibre-reinforced composites with emphasis on fibre kinking. Part II: FE implementation. *Composites Part A: Applied Science and Manufacturing*, 37(5):766–777.

Pohánková, I. (2010). Čedičová vlákna pro technické aplikace. Master's thesis, Technical University of Liberec.

Ramachandran, B., Velpari, V., and Balasubramanian, N. (1981). Chemical durability studies on basalt fibres. *Journal of Materials Science*, 16:3393–3397.

Saito, N., Aoki, K., Usui, Y., Shimizu, M., Hara, K., Narita, N., Ogihara, N., Nakamura, K., Ishigaki, N., Kato, H., Haniu, H., Taruta, S., and Endo, M. (2011). Application of carbon fibers to biomaterials: A new era of nano-level control of carbon fibers after 30-years of development. *Chemical Society reviews*, 40:3824–34.

Sim, J., Park, C., and Moon, D. Y. (2005). Characteristics of basalt fiber as a strengthening material for concrete structures. *Composites Part B: Engineering*, 36(6):504–512.

Strugala, G., Landowski, M., Zaremba, M., Turowski, J., and Szkodo, M. (2018). Impact resistance of plain and twill fabric in GFRP measured by active thermography. *Composites and Advanced Materials*, 27:176–184.

Teplý, J. L. and Dvorak, G. J. (1988). Bound on overall instantaneous properties of elastic-plastic composites. *Journal of the Mechanics and Physics of Solids*, 36(1):29–58.

Tervoort, T. A. (1996). Constitutive modeling of polymer glasses: Finite, nonlinear viscoelastic behaviour of polycarbonate. Master's thesis, Eindhoven University of Technology, Eindhoven.

Tiberti, S. and Milani, G. (2020). 3D homogenized limit analysis of non-periodic multi-leaf masonry walls. *Computers and Structures*, 234:106253.

Tomková, B., Novotná, J., and Pechočiaková, M. (2018). Limits of carbon micro/nano particles utilization to improve properties of polymer matrices in fibre reinforced composites. *IOP Conference Series: Materials Science and Engineering*, 459:012024.

Tsai, S. W. and Wu, E. M. (1971). A general theory of strength for anisotropic materials. *Journal of Composite Materials*, 5:58–80.

Valenta, R. (2003). Numerical modeling of polymers. Master's thesis, Faculty of Civil Engineering, Czech Technical University in Prague.

Valenta, R. (2011). Micromechanical modeling of asphalt mixtures. Master's thesis, Czech Technical University in Prague, Faculty of Civil Engineering.

Valenta, R., Šejnoha, J., and Šejnoha, M. (2003). Transformace funkce dotvarování na relaxační funkci. *Stavební obzor*, 12(4):116–121.

Valenta, R. and Šejnoha, M. (2004). Epoxy resin as a bonding agent in polymer matrix composites: material properties and numerical implementation. Presented at ICCES'04 Madeira, Portugal, July 26-29.

Valenta, R. and Šejnoha, M. (2012). Hierarchical modeling of mastic asphalt in layered road structures based on the Mori-Tanaka method. *Acta Polytechnica*, 52(6):48–58.

Valenta, R., Šejnoha, M., and Zeman, J. (2010). Macroscopic constitutive law for mastic asphalt mixtures from multiscale modeling. *International Journal for Multiscale Computational Engineering*, 8(1):131–149.

Valentová, S., Hrbek, V., Vorel, J., and Šejnoha, M. (2018). Strength of composite yarn under biaxial loading. *Acta Polytechnica CTU Proceedings*, 15:131–136.

Valentová, S., Hrbek, V., and Šejnoha, M. (2017). Evaluation of effective properties of basalt textile reinforced ceramic matrix composites. *Acta Polytechnica CTU Proceedings*, 13:142–147.

Valentová, S., Šejnoha, M., and Vorel, J. (2020). Comparing Mori-Tanaka method and first-order homogenization scheme in the viscoelastic modeling of unidirectional fibrous composites. *Acta Polytechnica CTU Proceedings*, 26:133–138.

Valentová, S., Šejnoha, M., Vorel, J., and Prošek, Z. (2022). Influence of microstructure on rate-dependent response of unidirectional fibrous composites. *Acta Polytechnica CTU Proceedings*, 0:0–0.

Valentová, S., Šejnoha, M., Vorel, J., Sedláček, R., and Padevět, P. (2021). Application of the Mori-Tanaka method to describe the rate-dependent behavior of unidirectional fibrous composites. *Acta Polytechnica CTU Proceedings*, 30:114–120.

Černý, M., Glogar, P., Sucharda, Z., Chlup, Z., and Kotek, J. (2009). Partially pyrolyzed composites with basalt fibres–mechanical properties at laboratory and elevated temperatures. *Composites Part A: Applied Science and Manufacturing*, 40(10):1650–1659.

Černý, M., Sucharda, Z., and Glogar, P. (2008). Mechanical behavior of polysiloxane matrix-based composite reinforced with basalt fibers at elevated temperatures. *Acta Geodynamica et Geomaterialia*, 5(4(152)):399–406.

Černý, M., Sucharda, Z., Glogar, P., Strachota, A., Chlup, Z., and Glogar, P. (2010). Influence of the organic/inorganic pyrolysis convresion level on mechanical properties of composites with E-glass or Basalt fibre reinforcement. *Ceramics-Silikáty*, 54(4):345–351.

Veselý, P. and Bezkočka, K. (2008). Pojiva na bázi polysiloxanů pro tepelně odolné nátěrové hmoty. In Kalendová, A., editor, *39th International Conference on Coatings Technology*. University of Pardubice, Faculty of Chemical Technology, Faculty of Chemical Technology.

Vorel, J., Grippon, E., and Šejnoha, M. (2015). Effective thermoelastic properties of polysiloxane matrix based plain weave textile composites. *International Journal for Multiscale Computational Engineering*, 13(3):181–200.

Vorel, J., Šmilauer, V., and Bittnar, Z. (2012). Multiscale simulations of concrete mechanical tests. *Journal of Computational and Applied Mathematics*, 236(18):4882–4892.

Vorel, J., Urbanová, S., Grippon, E., Jandejsek, I., Maršálková, M., and Šejnoha, M. (2013). Multi-scale modeling of textile reinforced ceramic composites. *Developments in Strategic Materials and Computational Design IV*, pages 233–245.

Vorel, J. and Šejnoha, M. (2009). Evaluation of homogenized thermal conductivities of imperfect carbon-carbon textile composites using the Mori-Tanaka method. *Structural Engineering and Mechanics*, 33(4):429–446.

Šejnoha, M., Valenta, R., and Zeman, J. (2004). Nonlinear viscoelastic analysis of statistically homogeneous random composites. *International Journal for Multiscale Computational Engineering*, 2(4):645–673.

Šejnoha, M. and Zeman, J. (2002). Overall viscoelastic response of random fibrous composites with statistically quasi uniform distribution of reinforcements. *Computer Methods in Applied Mechanics and Engineering*, 191(44):5027–5044.

Šejnoha, M. and Zeman, J. (2008). Micromechanical modeling of imperfect textile composites. *International Journal of Engineering Science*, 46:513–526.

Šejnoha, M. and Zeman, J. (2013). *Micromechanics in Practice*. WIT Press, Southampton, Boston.

Šmilauer, V., Hoover, C. G., Bažant, Z. P., Caner, F. C., Waas, A. M., and Shahwan, K. W. (2011). Multiscale simulation of fracture of braided composites via repetitive unit cells. *Engineering Fracture Mechanics*, 78:901–918.

Walpole, J. L. (1969). On the overall elastic moduli of composite materials. *Journal of the Mechanics and Physics of Solids*, 17:289–301.

Wang, X., Guan, Z., , Du, S., , Han, G., and Li, Z. (2020). An accurate and easy to implement method for predicting matrix crack and plasticity of composites with an efficient search algorithm for LaRC05 criterion. *Composites Part A*, 131:105808.

Zeman, J. (2003). Analysis of composite materials with random microstructure. Master's thesis, Citeseer, Czech Technical University in Prague.

Zeman, J. and Šejnoha, M. (2001). Numerical evaluation of effective properties of graphite fiber tow impregnated by polymer matrix. *Journal of the Mechanics and Physics of Solids*, 49(1):69–90.

Zeman, J. and Šejnoha, M. (2007). From random microstructures to representative volume elements. *Modelling and Simulation in Materials Science and Engineering*, 15(4):S325–S335.

Zhang, J., Chen, X., Tian, A., and Yin Fan, Y. (2022). Tests and numerical study of single-lap thermoplastic compo-site joints bolted by countersunk. *Materials*, 0:0–0.

Zhou, Y., Lu, Z., and Yang, Z. (2013). Progressive damage analysis and strength prediction of 2D plain weave composites. *Composites Part B: Engineering*, 47:220–229.

LIST OF AUTHOR'S PUBLICATIONS

ARTICLES IN CONFERENCE PROCEEDINGS

Maršálková, M., Urbanová, S., Salačová, J., et al. (2012). Effective mechanical and transport properties of polysiloxane matrix based composites. *High Performance Structures and Materials VI*, 124:185.

Šejnoha, M., Valentová, S., Vorel, J., Padevět, P., Sedláček, R., Tomková, B., and Novotná, J. (2020). Modeling of viscoelastic response of unidirectional fibrous composites made of basalt and carbon fibers. *High Performance and Optimum Design of Structures and Materials IV*, 196:19.

Urbanová, S., Šejnoha, M., and Vorel, J. (2013). Structural and material analysis of ceramic matrix composites. *Engineering Mechanics 2013*, pages 633–641.

Urbanová, S., Vorel, J., and Šejnoha, M. (2014). The influence of different implementation of periodic boundary conditions into FEM software. *20 th International Conference Engineering Mechanics 2014*, pages 672–675.

Valentová, S., Hrbek, V., and Šejnoha, M. (2017a). Evaluation of effective properties of basalt textile reinforced ceramic matrix composites. *Acta Polytechnica CTU Proceedings*, 13:142–147.

Valentová, S., Hrbek, V., Vorel, J., and Šejnoha, M. (2018). Strength of composite yarn under biaxial loading. *Acta Polytechnica CTU Proceedings*, 15:131–136.

Valentová, S., Šejnoha, M., and Vorel, J. (2020). Comparing Mori-Tanaka method and first-order homogenization scheme in the viscoelastic modeling of unidirectional fibrous composites. *Acta Polytechnica CTU Proceedings*, 26:133–138.

Valentová, S., Šejnoha, M., Vorel, J., and Prošek, Z. (2022). Influence of microstructure on rate-dependent response of unidirectional fibrous composites. *Acta Polytechnica CTU Proceedings*, 34:127–132.

Valentová, S., Šejnoha, M., Vorel, J., Sedláček, R., and Padevět, P. (2021). Application of the Mori-Tanaka method to describe the rate-dependent behavior of unidirectional fibrous composites. *Acta Polytechnica CTU Proceedings*, 30:114–120.

Valentová, S., Vorel, J., and Šejnoha, M. (2017b). Effective elastic and strength properties of unidirectional fibrous ceramic composites. *Engineering Mechanics 2017*, pages 1010–1013.

Vorel, J., Sýkora, J., Urbanová, S., and Šejnoha, M. (2015). From CT scans of wood to finite element meshes. *Proceedings of the Fifteenth International Conference on Civil, Structural and Environmental Engineering Computing*, pages 1–13.

Vorel, J., Urbanová, S., Grippon, E., Jandejsek, I., Maršálková, M., and Šejnoha, M. (2013). Multi-scale modeling of textile reinforced ceramic composites. *Developments in Strategic Materials and Computational Design IV*, pages 233–245.

ARTICLES IN JOURNALS

Šejnoha, M., Vorel, J., Valentová, S., and Marseglia, G. (2021). Multiscale viscoelastic analysis of plain weave textile composites. *International Journal of Computational Methods and Experimental Measurements*, 9(3):189–200.

Appendix A

TECHNICAL SHEETS OF STUDIED EPOXY RESINS AND HARDENERS

The following technical sheets of individual laminating epoxy resins and hardeners used in this work are presented for the sake of completness:

1. Lamination resin L285 with Hardener H500
2. Lamination resin L285 with Hardeners 285, 286, 287
3. Hardener H508
4. Lamination resin E455
5. Lamination resin E520
6. Hardener H492

Laminating resin L 285
Hardener 500

Résine L 285
Durcisseur 500

Characteristics

Caractéristiques

Approval:	--
Application:	Production of composite structures Boat and shipbuildung Sports equipment Model airplanes Moulds and tools
Operational temperature:	-60°C –> +50 - 60°C (-75°F –>+120 - 140°F) without heat treatment
Processing:	At temperatures between 10°C and 40°C (50-105°F) All usual processing methods
Special properties:	Extremely good physiological compatibility Good mechanical properties Very short curing times even at low temperatures
Special modifications:	L 285 T: Thixotropic L 285 W: White

Homologation:	*--*
Domaines d'application:	*Fixations et encollages lors de la fabrication de composants en matériaux composites* *Construction de bateaux, équipements sportifs, aéromodélisme* *Construction de moules, de gabarits et de montures*
Température d'application:	*-60°C à +50 - 60°C* *sans traitement thermique*
Mise en oeuvre:	*A des températures* *entre 10°C et 40°C* *Tous les procédés de traitement d'usage*
Particularités:	*Excellent caractère physiologique* *Bonnes propriétés mécaniques* *Durcissement très rapide, même à basses températures*
Adaptations spéciales:	*L 285 T: thixotropique* *L 285 W: teinture blanche*

Laminating resin L 285
Hardener 500

Résine L 285
Durcisseur 500

Application

Low-viscosity laminating resin system not containing solvents or fillers, intended for processing and curing at room temperature. Suitable for production of parts with glass, carbon and aramide fiber reinforcements featuring high static and dynamic loadability.
The pot live is approx. 10 - 15 min. Laminating resin L 285 combined with hardener 500 is distinguished by very short curing times even at low temperatures (good curing is assured at temperatures starting at +10 °C). Non-tacky, high-gloss surfaces are obtained even with unfavorable curing conditions, such as lower temperatures or high relative humidity.

The mixing viscosities have been adjusted such that the resin will not run out of wide-meshed fabrics on vertical surfaces.

Thanks to their excellent adhesive properties, this system can also be used as adhesives for wood, metal, glass, concrete and numerous plastics. The thixotropic modification (e.g. laminating resin L 285 T) is to be preferred for thicker adhesive joints and vertical surfaces. Fillers (e.g. metal powder, talcum, cotton flakes, etc.) may be admixed to obtain special system properties.
Due to the elongation of 4-7%, which is advantageous for use as a laminating resin, the shear strength and peel resistance are somewhat lower than those of our special adhesive resins:
Adhesive resin L 135 / K2 and
Adhesive resin A 10 / A 20.

As a general rule applicable to all adhesives, thorough preparation of the intended adhesion surface is a fundamental prerequisite for good adhesion. Parting agent residue and contamination, such as dust, grease or water residue, will prevent effective bonding.

Application

Système de résine pour stratifié, de faible viscosité et exempts de solvants et d'additifs, pour la mise en œuvre et le durcissement à température ambiante. Ce système permet de produire des composants, avec renforcement à fibres de carbone et d'aramide, possédant une charge statique et dynamique élevée.
Le temp d'utilisation se situe env. entre 10 et 15 minutes. La résine L 285 avec le durcisseur 500 se distingue par des temps de durcissement très rapides, même à des basses températures (très bon durcissement à partir de + 10 °C). Même dans des conditions de durcissement désavantageuses (basses températures ou humidité de l'air élevée), on obtient des surfaces polies et non adhérentes.

Les viscosités de mélange ont été choisies de manière à empêcher, de manière sûre, toute fuite de résine lors de l'utilisation de tissus à larges mailles sur des surfaces verticales.

Grâce aux bonnes propriétés d'adhésion, ce système peut également être utilisés comme adhésif pour des matériaux tels que le bois, le métal, le verre, le béton et de nombreuses matières synthétiques. La formule thixotropique (par ex. résine L 285 T) convient en particulier pour des larges fentes de collage et sur des surfaces verticales. L'utilisateur peut lui-même ajouter des additifs afin d'attribuer au système des propriétés spéciales (poudre métallique, talc, flocons de coton, etc.).
Les élongations avantageuses de 4 à 7% de l'application d'une résine pour stratifiés présentent cependant des résistances au cisaillement et au décollement légèrement inférieures à celles de nos
résines adhésives spéciales - type L 135/K2 et A 10 / A 20.

Comme c'est le cas pour toutes les colles, le traitement préliminaire de la surface d'encollage est une condition primordiale pour assurer une bonne adhésion. Les résidus d'agent de démoulage ainsi que des souillures telles que poussière, graisse ou eau empêchent une bonne adhésion.

Laminating resin L 285
Hardener 500

Résine L 285
Durcisseur 500

Specifications

Spécifications

		Laminating resin L 285 *Résine L 285*
Density *Densité*	lbs/gal / 77°F g/cm³ / 25°C	9.85 - 10.26 1,18 - 1,23
Viscosity *Viscosité*	cps / 77°F mPas / 25°C	600 - 900
Epoxide equivalent *Equivalent époxy*	–	165 - 170
Epoxide value *Valeur EP*	–	0,59 - 0,65
Colour *Coloration selon*	Gardner	max 3

		Hardener 500 *Durcisseur 500*
Density *Densité*	lbs/gal / 77°F g/cm³ / 25°C	8.34 - 8.84 1,00 - 1,06
Viscosity *Viscosité*	cps / 77°F mPas / 25°C	200 - 350
Amine value *Indice d'amine*	mg KOH / g	350 - 400
Colour *Coloration selon*	Gardner	max 5

Laminating resin L 285
Hardener 500

Résine L 285
Durcisseur 500

Processing details

Caractéristiques de mise en oeuvre

	Laminating resin L 285 *Résine L 285*	Hardener 500 *Durcisseur 500*
Average EP -Value *Valeur moyenne EP*	0,63	–
Average amine equivalent *Equivalent moyen d'amine*	–	62

Storage *Stockage*	>12 months in original containers *>12 mois dansl'emballage d'origine*
Processing temperature *Température d'application*	50 - 120°F 10 - 50°C
Temperature rise *Montèe de température*	see diagram *voir diagramme*
Setting *Durcissement*	Curing at room temperature or curing in the mold at high temperaturtes *Durcissement à température ambiante ou durcissement à chaud dans le moule*
Heat treatment *Traitement thermique*	Not required- possible at 50°C (120°F) ->150°C (300°F) *Non requis-au besoin entre 50°C –> 150°C*

Storage

Stockage

The resins and hardeners can be stored for at least 12 months in their carefully sealed original containers. The resins and hardeners may crystallize at temperatures below +15°C(60°F). The crystallization is visible as a clouding or solidification of the contents of the container. Before processing, the crystallization must be removed by warming up. Slow warming up to approx. 50 - 60°C (120-140°F) in a water bath or oven and stirring or shaking will clarify the contents of the container without any loss of quality. Use only completely transparent products. Before warming up, open containers slightly to permit equalization of pressure. Caution during warm-up! Do not warm up over an open flame! While stirring up use safety equipment (gloves, eyeglasses, respirator).

Les résines et durcisseurs peuvent être stockés dans leur emballage d'origine, bien fermé, pendant une durée minimale de 12 mois. Les résines et durcisseurs peuvent cristalliser à des températures inférieures à +15°C, reconnaissable à une consistance trouble ou une solidification du contenu du récipient. Avant la mise en oeuvre, il faut éliminer la cristallisation par réchauffement. La cristallisation est éliminée, sans perte de qualité, en réchauffant lentement le produit à env. 50-60°C dans un bain marie ou un four et en agitant ou ballottant la substance. Traiter uniquement des produits entièrement transparents ! Attention lors du réchauffement ! Avant son réchauffement, ouvrir un peu le récipient afin de compenser la pression. Ne jamais réchauffer le récipient sur feu nu ! Porter des équipements de protection (lunettes et gants de protection, masque respiratoire) pendant l'agitation des produits réchauffés.

Laminating resin L 285
Hardener 500

Résine L 285
Durcisseur 500

Temperature rise
Quantity: 100 g/20°C (70°F)

Montée en température
Quantité: (100 g/20 °C)

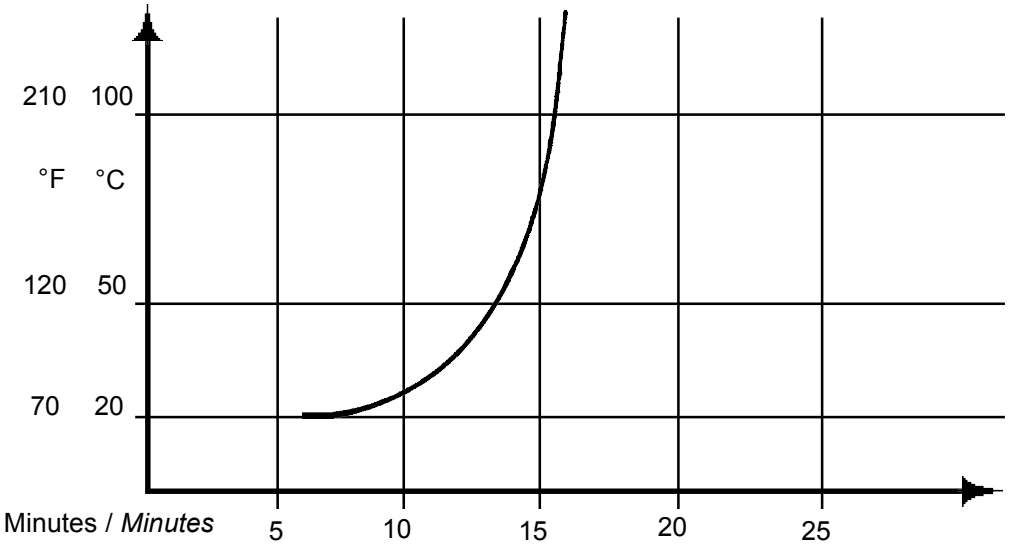

The optimal processing temperature is in the range between 20 and 25°C (70-80°F). Higher processing temperatures are possible, but will shorten pot life. A rise in temperature of 10 °C (20°F) will halve the pot life. Water (for example very high humidity or contained in fillers) causes an acceleration of the resin/hardener reaction. Different temperatures and humidities during processing have no significant effect on the strength of the cured product.
Do not mix large quantities, especially from this highly reactive system. The heat flow from the mixing container is very low, so the contents will be warmed up very fast because of the reaction heat (exothermic resin-hardener reaction). This can cause temperatures >200°C (400°F) which may cause smoke intensive burning of the resin-hardener mixture.

La température de mise en oeuvre optimale se situe entre 20 et 25 °C. Des températures supérieures sont possibles, mais elles réduisent le temps d'utilisation. Une augmentation de la température de mise en oeuvre de 10 °C réduit le temps d'utilisation de moitié. L'eau (p. ex. une humidité de l'air très élevée ou des additifs humides) agit comme accélérateur pour la réaction résine/durcisseur. Cependant, des variations de température et de l'humidité de l'air pendant la mise en oeuvre n'ont pratiquement aucun effet sur la résistance du produit durci.
Avec des températures de mise en oeuvre supérieures, surtout pour des systèmes hautement réactifs, il est recommandé de ne pas mélanger de grandes quantités. La dissipation de chaleur hors du récipient de mélange étant très faible, la chaleur de réaction (réaction exothermique de résine/durcisseur) entraîne un réchauffement rapide du contenu du récipient. Les températures à l'intérieur du récipient peuvent dépasser 200 °C et entraîner la carbonisation de la masse de résine avec une forte émission de fumée.

Gel time
Film thickness
1 mm
at different
temperatures

70 - 80°F 20 - 25°C	app. 45 - 60 min. env. 45 - 60 min.
105-115°F 40 - 45°C	app. 20 - 30 min. env. 20 - 30 min.

Temps de gélification
Epaisseur de couche 1 mm à différentes températures

Laminating resin L 285
Hardener 500

Résine L 285
Durcisseur 500

Mixture ratio

Rapports de mélange

	Resin L 285 : Hardener 500 *Résines L 285 : Durcisseur 500*
Parts by weight ***Parts de poids***	**100 : 40 +/-2**
Parts by volume ***Parts de volume***	**100 : 50 +/-2**

The specified mixing ratios must be observed as exactly as possible. Adding more or less hardener will not effect a faster or slower reaction - only incomplete curing which cannot be corrected in any way.
The mixture of resin and hardener must be mixed very thoroughly. Mix until no clouding is visible in the mixing container. Pay special attention to the walls and the bottom of the mixing container.

Les rapports de mélange indiqués doivent être observés. L'augmentation ou la réduction des parts de durcisseur n'entraîne en aucun cas une réaction plus rapide ou plus lente, mais uniquement un durcissement partiel du produit qui ne se laisse plus corriger, même par un post-traitement.
La résine et le durcisseur doivent être mélangés avec grande précaution. Dans le récipient, le mélange doit être exempt de stries. Prêter une attention particulière aux zones dans le fond et sur les parois du récipient de mélange.

Mixing ratio <–> glass transition temperature

Rapport de mélange <–> Température de transition vitreuse

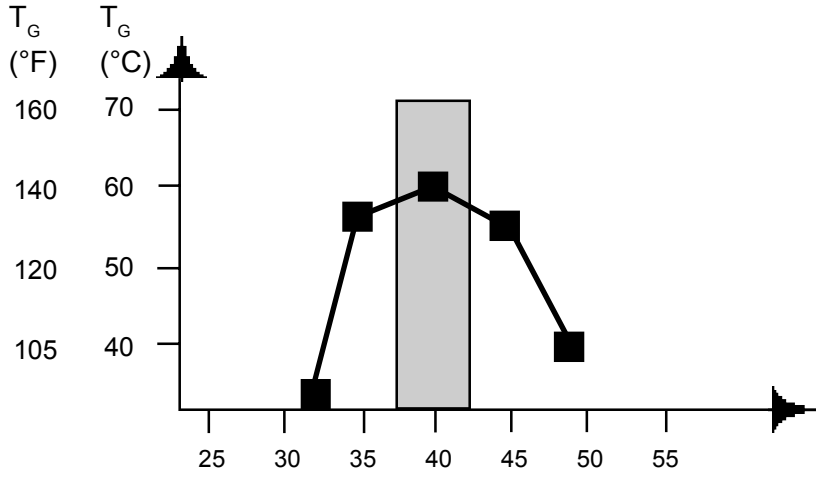

.....Parts by weight of hardener 500 to
100 parts by weight of laminating resin L 285
Curing: 14 days at 25°C (80°F)

.....Parts de poids du durcisseur 500 sur
100 parts de poids de résine L 285
Durcissement 14 jours à 25°C

Laminating resin L 285
Hardener 500

Résine L 285
Durcisseur 500

Laminating resin L 285 - Hardener 500 ***Résin L 285 - Durcisseur 500***	
Max T_G for curing at 18°C (65°F) *Max T_G à 18°C durcissement*	100 - 110°F 40 - 45°C
Max T_G for curing at 25°C (80°F) *Max T_G à 25°C durcissement*	120 - 150°F 50 - 60°C
Max T_G for heat treatment at 50°C (120°F) *Max T_G à 50°C traitement thermique*	140 - 150°F 60 - 65°C

DSC DIN 51007

DSC DIN 51007

Modulus of rigidity DIN 53445

Module d'élasticité DIN 53445

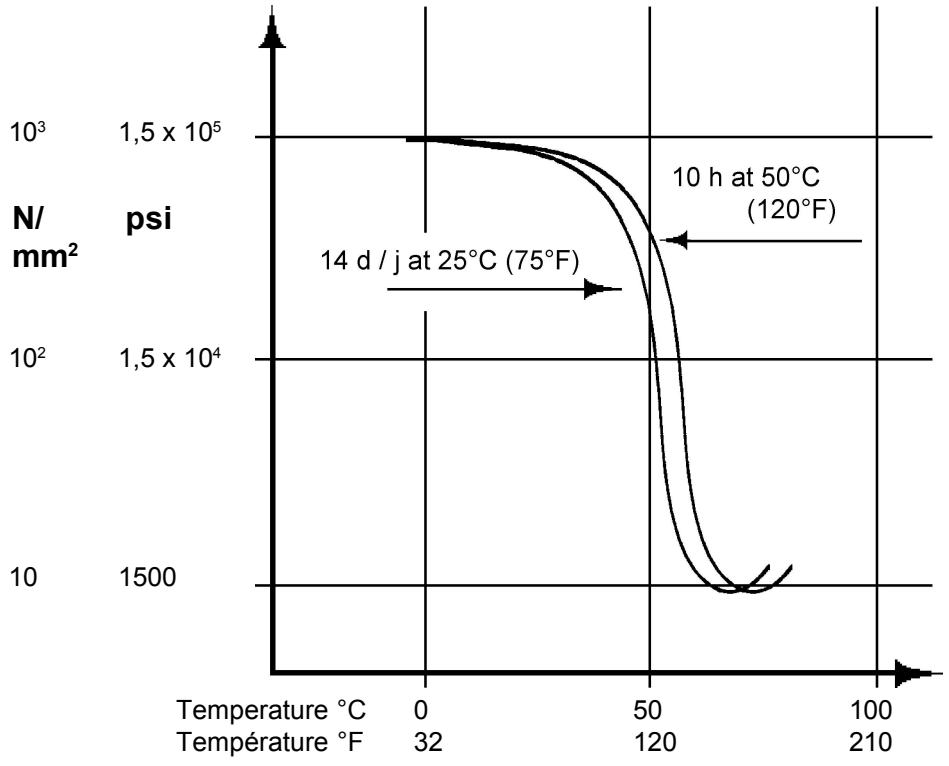

Laminating resin L 285
Hardener 500

Résine L 285
Durcisseur 500

Mechanical data of unreinforced resin

Données mécaniques de la masse de résine non renforcée

Density *Densité*	lbs/gal g/cm³	9.8 – 10 1,18 - 1,20
Flexural strength *Résistance à la flexion*	psi x 10^3 N/mm²	17 - 20 120 - 140
Modulus of elasticity *Module d'élasticité en flexion*	psi x 10^5 kN/mm²	4.8 - 5.1 3,3 - 3,5
Tensile strength *Résistance à la traction*	psi x 10^3 N/mm²	10 - 11.5 70 - 80
Compressive strength *Résistance à la pression (Dureté)*	psi x 10^3 N/mm²	18 - 20 120 - 140
Elongation *Allongement*	%	5 - 6,5
Impact strength *Résistance aux chocs*	Nmm/mm²	40 - 50
Shore hardness *Dureté / Shore*	D	86 - 90
Water absorption % *Absorption d'eau %*	24 h 23°C (75°F) 7 d/23°C (75°F)	0,10 - 0,20 0,20 - 0,50
Fatigue strength under reversed bending stresses acc. to DLR Brunsw. *Tenue à la flexion alternée selon DLR Braunschweig*	10% 90%	exp. 2 X 10^6 exp. 2 X 10^6
Curing: **24 h at 23°C (75°F)** **+ 15 h at 60°C (140°F)** ***Durcissement:*** ***24 h à 23°C*** ***+ 15 h à 60°C.***		
Representative data according to **WL 5.3203 Parts 1 and 2** of the German Aviation Materials Manual.		***Données représentatives*** *établies d'après les régulations* ***WL 5.3203 parts 1 et 2*** *prises du manual sur les matières de l'aviation allemande*

Laminating resin L 285
Hardener 500

Résine L 285
Durcisseur 500

Tensile shear strength

Test sample: Double overlapping sample acc. to LBA

Résistances d'adhésion
Résistance à la traction et au cisaillement

Eprouvette: éprouvettes bicouche selon la directive LBA

Different wood types

Différents types de bois

Boat plywood *Contreplaqué pour bateaux*	Pine wood *Pin*	Teak wood *Bois de tec*	Mahogany wood *Acajou*
6 - 7 N/mm² 0.8-1.0 psi x 10^3	7 - 8 N/mm² 1.0-1.2 psi x 10^3	6 - 7 N/mm² 0.8-1.0 psi x 10^3	7 - 8 N/mm² 1.0-1.2 psi x 10^3

Rise of tensile shear strength at 25°C (80°F)

Test sample: Pine wood

Augmentation de la résistance à la traction et au cisaillement à 25°C

Eprouvette: pin

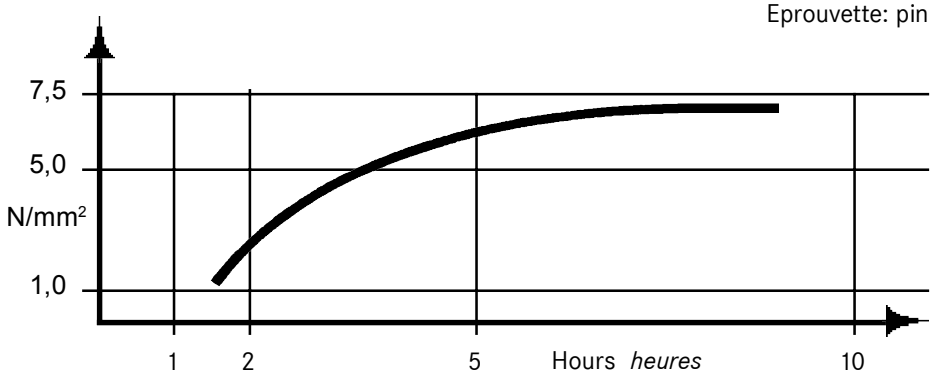

Temperature <–> tensile shear strength

Résistance thermique de l'encollage

Test sample: Pine wood
Eprouvette: pin

Heat treatment:
traitement thermique:

15h 50°C/120°F

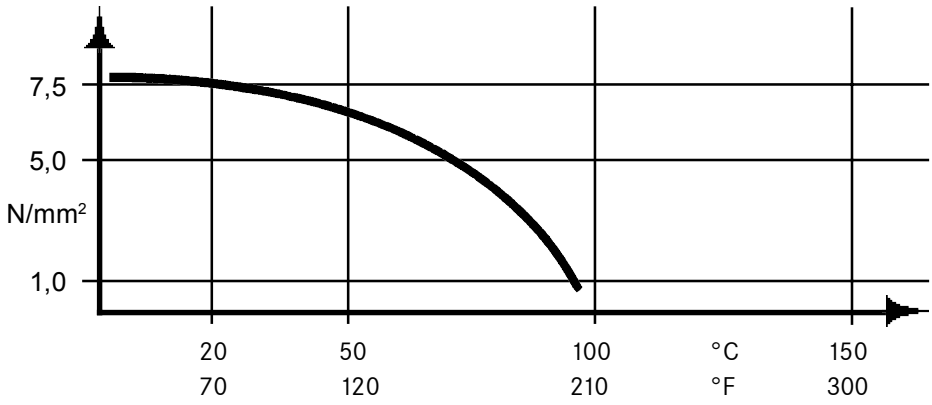

L A M I N A Č N Í P R Y S K Y Ř I C E L 285
T U Ž I D L A 285, 286, 287

Návod k použití, technické listy

Charakteristika

Schválení:	Německý federální úřad pro letectví
Použití:	výroba kluzáků, motorových kluzáků a motorových letadel, lodě a stavba lodí, sportovní nářadí, letecké modely, formy a nástroje
Teplotní odolnost výrobků bez výrazných změn jejich parametrů:	- 60 °C - □ + 50-60 °C za temperování - 60 °C - □ + 80-+ 100 °C po temperování
Zpracování:	Při teplotách mezi 10 °C a 50 °C Všechny běžné metody zpracování
Zvláštní vlastnosti:	Extrémně dobrá fyziologická kompatibilita Dobré mechanické a tepelné vlastnosti Doba zpracovatelnosti (tzv. pot life) od přibližně 45 minut do asi 5 hodin (závisí na použitém tužidle)
Zvláštní úpravy:	L 285 T: tixotropní L 285 K2: tixotropní tepelná úprava L 285 W: bílá

Použití

Systém laminační pryskyřice, schválený německým federálním úřadem pro letectví, má rozdílné doby zpracovatelnosti (v závislosti na použitém tužidle) pro výrobu s použitím skelných, uhlíkových a kevlarových vláken a vyznačuje se vysokými statickými a dynamickými vlastnostmi.

Po tepelném vytvrzení při 50 - 55 °C systém splňuje standard pro větroně a motorové větroně (pracovní teplota - 60 °C až + 54 °C. Pro splnění požadavků motorových letadel (pracovní teploty - 60 °C až + 72 °C) je nezbytné tepelné vytvrzení při 80 °C.

Rozmezí doby zpracovatelnosti (tzv. pot life) je mezi přibližně 45 min. a 5 h v závislosti na druhu tužidla. Tužidla mají stejný poměr míchání a mohou být míchány mezi sebou v jakémkoli poměru. Toto dovoluje výběr optimálního systému pro všechny metody zpracování. Po počátečním vytvrzení při pokojové teplotě jsou vyrobené komponenty opracovatelné a lze je vytáhnout z formy. Získáte vysoce se lesknoucí a nelepivé povrchy, a to dokonce i při nepříznivých podmínkách při vytvrzování, tj. nižší teploty nebo vysoká vlhkost.

Viskozita směsi zaručuje rychlé a dokonalé prosycení vláken, nicméně, pryskyřice se nerozlije na tkanině na vertikálním povrchu. Za účelem získání zvláštních vlastností je rovněž možné přidat ke směsi pryskyřice/tužidlo nejrůznější plniva, např. aerosil, mikrobalony, bavlněné vločky, kovový prášek apod.
Pokud se nevyžaduje vysoká tepelná odolnost či letecké schválení, dá se tužidlo 285 použít bez následného temperování. Nicméně, uvedené vlastnosti získá pouze po tepelném vytvrzení při teplotách nad 50 °C.

Použití
Laminační systém má hydrofilní charakter (vyšší absorpce vlhkosti, nižší odpor rozptylu páry). Proto neočekáváme žádné problémy kompatibility při jeho kombinaci s polyesterovými gelcoaty, rozmanitými barvami (např. na bázi PUR) atd. Bohužel však nemáme k dispozici testy těchto kombinací.

Od svého schválení v roce 1985 byl laminační systém L 285 používán téměř všemi výrobci letadel a kluzáků a - zvláště kvůli své extrémně dobré fyziologické kompatibilitě - je nejvíce užívaným systémem dnešního leteckého průmyslu. Často se stává, že pracovníci, kteří zaznamenali problémy s některými epoxidy (alergie či podráždění pokožky), jsou schopni zpracovávat laminační pryskyřici L 285.

Je nutno dodržovat příslušná bezpečností pokyny pro manipulaci s epoxidovými pryskyřicemi a tužidlo a naše instrukce pro bezpečné zpracování.

Specifikace

		Laminační pryskyřice L 285
Hustota °C	g/cm 3 / 25	1,18 - 1,23
Viskozita °C	mPas / 25	600 - 900
Ekvivalent epoxidu	-	165 - 170
Hodnota epoxidu	-	0,59 - 0,65
Barva Gardner		max 3

		Tužidlo 285	Tužidlo 286	Tužidlo 287
Hustota °C	g/cm3 / 25	0,94 - 0,97	0,94 - 0,97	0,93 - 0,96
Viskozita °C	mPas / 25	50 - 100	60 - 100	80 - 100
Aminové číslo G	mg KOH /	480 - 550	450 - 500	450 - 500
Barva Gardner		max 3 (*)	max 3 (*)	max 3 (*)

(*) Vztahuje se pouze k průsvitnému tužidlu - tužidla mají průsvitně modrou barvu

HAVEL COMPOSITES CZ s.r.o.
Svésedlice 67
783 54 Přáslavice
tel.: +420 585 129 011
fax: +420 585 129 040
info@havel-composites.cz
www.havel-composites.com
IČ: 25907379
DIČ: CZ25907379

TECHNICKÝ LIST

Tužidlo H 508

Charakteristika: je kapalné tvrdidlo pro epoxidové pryskyřice. Tvrdidlo je na bázi cykloaliaftického polyaminu, hlavní složka Izoforon di-amin. Neobsahuje nonylphenol.

Fyzikální parametry:

Viskozita při 25°C	m Pa.s.	7 - 11
Vodíkový ekvivalent	g	51
Hustota při 20 °C	kg/m 3	930- 960
Barva (Gardner)		nad 2

Použití: Tužidlo H 508 je tvrdidlo pro epoxidové pryskyřice. Je vhodné ke všem typům laminací při teplotách nad 15°C.
Vyšší tepelnou odolnost vytvrzené pryskyřice lze dosáhnout dotvrzením systému při zvýšené teplotě 50- 60 °C.
Doba zpracovatelnosti cca 60 minut.

Balení/Skladování: Tento produkt je dodáván v sudech 180kg 30kg, 5kg, 1kg

Transport: Produkt musí být dopravován pouze v uzavřených obalech. Skladovací teploty by se měly pohybovat v rozmezí teplot 10-30°C. Skladované místo by mělo být suché, a bez přímého slunečního světla. V případě správného skladování je životnost 12 měsíců.

Bezpečnostní doporučení: Tužidlo H 508 je označen jako „C“ Žíravý a X_n zdraví škodlivý podléhá tedy platným zásadám vyplývajícím ze zásad manipulace s nebezpečnými chemickými látkami.

CHS-EPOXY 455 / Epoxy 1505

Epoxidová pryskyřice pro lepení

POUŽITÍ: K zalévání, odlévání, přípravě tmelů, stěrkových hmot, polymermaltových a polymerbetonových kompozic apod. v různých odvětvích průmyslu. K výrobě a opravám sportovních laminátových potřeb. Vytvrzuje se vhodnými tvrdidly při normální nebo mírně zvýšené teplotě (30-60 °C). Po vytvrzení zůstává pryskyřice transparentní. V případě potřeby lze probarvovat pigmentovými pastami **EPROTINT**. Pryskyřice ani natužená směs se před aplikací nesmí ředit přídavkem žádného rozpouštědla ani ředidla.

PŘÍPRAVA POVRCHU:
Povrch musí být suchý, čistý, odmaštěný a zbavený mechanických nečistot (prach po broušení atd.), nejlépe zdrsněný. Doporučená teplota podkladu je +15 až +25 °C při max. 60 % relativní vlhkosti vzduchu. Nevytvrzenou kompozici lze z povrchu nářadí umýt Ředidlem **SINEPOX S 6300** nebo **Lignofix S 6300** případně acetonem.

NÁVOD K POUŽITÍ: Balení setu 770 g **CHS-EPOXY 455 / EPOXY 1505** je připraveno v přesném poměru pryskyřice (složka A) a tužidla (složka B) pro jednoduchou přípravu. Před aplikací menšího množství, důkladně promíchejte ve správném poměru složku A se složkou B. Nanášení kompozice zahajte cca 10 minut po dokonalém smíchání obou složek. Zpracovatelnost natužené směsi s dodávanou složkou B je cca 40 minut při +20 °C. Optimální teplota složek před zpracováním je +15 až +20 °C. Lepené plochy fixujte cca 2 až 4 hodiny.

VLASTNOSTI:
Vzhled: čirá, nažloutlá viskózní kapalina
Hustota (při +20 °C): > 1,16 g.cm^{-3}
Viskozita (při +25 °C): > 20 mPa.s
Obsah epoxidových skupin (mol.kg^{-1}): 4,3–4,8
Epoxidový hm. ekvivalent (g.mol^{-1}): 208–232
Neobsahuje VOC.

TUŽENÍ:	**poměr hmotnostní**	**poměr objemový**
CHS-Epoxy 455 : Tvrdidlo P 11	100 : 10	100 : 12,2
CHS-Epoxy 455 : Tvrdidlo T 0492	100 : 22	100 : 27
CHS-Epoxy 455 : Tvrdidlo T 0503	100 : 43	100 : 50
CHS-Epoxy 455 : Tvrdidlo AN 2609	100 : 34	100 : 37
CHS-Epoxy 455 : Tvrdidlo AN 2712	100 : 43	100 : 50

ZPRACOVÁNÍ: Tvrdidlo P 11 je rychlé tvrdidlo s kratší dobou zpracovatelnosti. Vyznačuje se povrchovým dolepem po vytvrzeni. Dolep lze odstranit omytím vodou nebo 3 % roztokem kyseliny citronové. Vytvrzená kompozice zůstává transparentní. Doporučená teplota obou složek před zpracováním je +15 až +20 °C.
Doba želatinace: 20–30 min. při +20 °C (dle připraveného množství).
Vytvrzení: 24 hodin při teplotě +20 °C pro manipulaci
Plné vytvrzení: 7 dní při teplotě +20 °C
1–2 dny při +20 °C a dotvrzeni 3 dny při +50 až +60 °C (infrazářiče)
uzavřené nádoby: po 7 dnech vytvrzování se dotvrzuje při teplotě +20 °C
naplněním nádoby vlažnou vodou, jejíž teplota se postupně zvýší až na +60 °C a udržuje se 2–3 dny.

CHS-EPOXY 455 / Epoxy 1505

Epoxidová pryskyřice pro lepení

Tvrdidlo T 0492 snižuje vývin tepla při reakci, proto je vhodné pro prodloužení doby zpracování.
Kompozit je transparentní a bez dolepu.
Doba želatinace: 50–80 minut při +20 °C (dle připraveného množství)
Vytvrzení: 24 hodin při teplotě +20 °C
Plné vytvrzení: 7 dni při teplotě +20 °C
Tvrdidlo T 0503 snižuje vývin tepla při reakci, proto je vhodné ke zpracování většího množství pryskyřice.
Vytvrzena kompozice je zabarvena do žluta a bez dolepu.
Doba želatinace: 45-70 min při +20 °C (dle připraveného množství)
Vytvrzení: 24 hodin při teplotě +20 °C
Plné vytvrzení: 7 dni při teplotě +20 °C
Tvrdidlo AN 2609 je rychlé tvrdidlo vhodné k vytvrzovaní za snížené teploty (do 5 °C). Vzhledem ke zvýšené reaktivitě není vhodné pro vytvrzování čistých pryskyřic ve větším množství. Pryskyřici je potřeba vrstvit.
Vytvrzena kompozice je transparentní a bez dolepu.
Doba želatinace: 25–35 minut. při +20 °C (dle připraveného množství)
Vytvrzení: 24 hodin při teplotě +20 °C
Plné vytvrzení: 5 dni při teplotě +20 °C
Tvrdidlo AN 2712 je rychlé tvrdidlo vhodné k vytvrzování za snížené teploty (do 5 °C). Vzhledem ke zvýšené reaktivitě není vhodné pro vytvrzováni čistých pryskyřic ve větším množství. Pryskyřici je potřeba vrstvit.
Vytvrzena kompozice je nažloutlá, čirá a bez dolepu.
Doba želatinace: 15–25 minut při +20 °C (dle připraveného množství)
Vytvrzení: 24 hodin při teplotě +20 °C
Plné vytvrzení: 5 dni při teplotě +20 °C

UPOZORNĚNÍ: Při aplikaci je třeba zajistit takové teplotní podmínky, aby nedošlo k vysrážení vlhkosti na povrchu opravovaného předmětu (rosný bod). Větráním je nutné omezit případný výskyt kyselých plynů a par (např.: CO2), které reagují s tužidlem a znemožňuji dokonale vytvrzeni materiálu. Natužením velkého množství pryskyřice dochází k vyvinu tepla a tím ke zkrácení doby zpracovatelnosti!
! **Výška odlitku** nesmí přesáhnout **20 mm**! Větší odlitky je nutno zhotovovat po vrstvách. Odvod tepla je možno zlepšit přídavkem vhodného plniva, např. suchého křemenného písku.
Nevytvrzenou kompozici lze z povrchu nářadí umýt acetonem. Vytvrzená kompozice lze odstranit pouze mechanicky. Pro zvýšení vytvrzovací teploty nepoužívejte naftové nebo propanbutanové hořáky. Doporučuje se použití infrazářiče.

UŽITNÉ VLASTNOSTI:

Přídržnost k podkladu (dle ČSN EN ISO 4624):	> 1,5 MPa
Pevnost v tlaku (dle ČSN EN ISO 604):	> 60 MPa
Pevnost v tahu (dle ČSN EN ISO 527-1):	> 30 MPa
Tažnost (dle ČSN EN ISO 527-2):	> 1,5 %
Nasákavost (dle ČSN EN ISO 62):	max. 1,5 %
Rázová houževnatost (dle ČSN EN ISO 179-1):	> 5 kJ/m^2
Zdravotní a hygienická nezávadnost:	kladné hodnocení
Lineární smrštění při vytvrzování:	max. 0,5 %
Tvarová stálost dle Martense:	min. 50 °C

CHS-EPOXY 520 / Epoxy 15

Epoxidová pryskyřice pro lití, lepení, laminace

POUŽITÍ: K impregnaci, zalévání, odlévání a lepení v různých odvětvích průmyslu.
Pro výrobu a opravy sportovních laminátových potřeb. K přípravě laminátů a k výrobě modifikovaných pryskyřic. Je vhodná pro výrobu tmelů, lepidel a stěrkových hmot.
Pryskyřice ani natužená směs se před aplikací nesmí ředit přídavkem žádného rozpouštědla ani ředidla.

PŘÍPRAVA POVRCHU:
Povrch musí být suchý, čistý, odmaštěný a zbavený mechanických nečistot (prach po broušení atd.), nejlépe zdrsněný. Doporučená teplota podkladu je +15 až +25 °C při max. 60 % relativní vlhkosti vzduchu.
Nevytvrzenou kompozici lze z povrchu nářadí umýt Ředidlem **SINEPOX S 6300** nebo **Lignofix S 6300** případně acetonem.

NÁVOD K POUŽITÍ: Balení setu **CHS-EPOXY 520 / EPOXY 15** 1,11 kg **s tvrdidlem P 11** je připraveno v přesném poměru pryskyřice (složka A) a tužidla (složka B) pro jednoduchou přípravu. Před aplikací menšího množství, důkladně promíchejte ve správném poměru složku A se složkou B. Nanášení kompozice zahajte cca 10 minut po dokonalém smíchání obou složek. Zpracovatelnost natužené směsi s dodávanou složkou B je cca 40 minut při +20 °C. Optimální teplota složek před zpracováním je +15 až +20 °C. Lepené plochy fixujte cca 2 až 4 hodiny.

VLASTNOSTI:
Vzhled: nažloutlá čirá viskózní kapalina
Hustota (+20 °C): > 1,16 g.cm^{-3}
Viskozita (25 °C): > 12,0 Pa.s
Obsah epoxidových skupin (mol.kg^{-1}): 5,2–5,5
Epoxidový hm. ekvivalent (g.mol^{-1}): 182–192
Neobsahuje VOC.

TUŽENÍ:	**poměr hmotnostní**	**poměr objemový**
CHS-Epoxy 520 : Tvrdidlo P 11	100 : 11	100 : 13,5
CHS-Epoxy 520 : Tvrdidlo T 0492	100 : 26	100 : 32
CHS-Epoxy 520 : Tvrdidlo T 0503	100 : 50	100 : 58
CHS-Epoxy 520 : Tvrdidlo AN 2609	100 : 40	100 : 44
CHS-Epoxy 520 : Tvrdidlo AN 2712	100 : 50	100 : 58

ZPRACOVÁNÍ: Tvrdidlo P 11 je rychlé tvrdidlo s kratší dobou zpracovatelnosti. Vyznačuje se povrchovým dolepem po vytvrzeni. Dolep lze odstranit omytím vodou nebo 3 % roztokem kyseliny citronové. Vytvrzená kompozice zůstává transparentní. Doporučená teplota obou složek před zpracováním je +15 až +20 °C.
Doba želatinace: 20–30 min. při +20 °C (dle připraveného množství).
Vytvrzení: 24 hodin při teplotě +20 °C pro manipulaci
Plné vytvrzení: 7 dní při teplotě +20 °C
1–2 dny při +20 °C a dotvrzeni 3 dny při +50 až +60 °C (infrazářiče)
uzavřené nádoby: po 7 dnech vytvrzování se dotvrzuje při teplotě +20 °C
naplněním nádoby vlažnou vodou, jejíž teplota se postupně zvýší až na +60 °C a udržuje se 2–3 dny.

CHS-EPOXY 520 / Epoxy 15

Epoxidová pryskyřice pro lití, lepení, laminace

Tvrdidlo T 0492 snižuje vývin tepla při reakci, proto je vhodné pro prodloužení doby zpracování.
Kompozit je transparentní a bez dolepu.
Doba želatinace: 50–80 minut při +20 °C (dle připraveného množství)
Vytvrzení: 24 hodin při teplotě +20 °C
Plné vytvrzení: 7 dni při teplotě +20 °C

Tvrdidlo T 0503 snižuje vývin tepla při reakci, proto je vhodné ke zpracování většího množství pryskyřice.
Vytvrzena kompozice je zabarvena do žluta a bez dolepu.
Doba želatinace: 45-70 min při +20 °C (dle připraveného množství)
Vytvrzení: 24 hodin při teplotě +20 °C
Plné vytvrzení: 7 dni při teplotě +20 °C

Tvrdidlo AN 2609 je rychlé tvrdidlo vhodné k vytvrzovaní za snížené teploty (do 5 °C). Vzhledem ke zvýšené reaktivitě není vhodné pro vytvrzování čistých pryskyřic ve větším množství. Pryskyřici je potřeba vrstvit.
Vytvrzena kompozice je transparentní a bez dolepu.
Doba želatinace: 20–35 minut. při +20 °C (dle připraveného množství)
Vytvrzení: 24 hodin při teplotě +20 °C
Plné vytvrzení: 5 dni při teplotě +20 °C

Tvrdidlo AN 2712 je rychlé tvrdidlo vhodné k vytvrzování za snížené teploty (do 5 °C). Vzhledem ke zvýšené reaktivitě není vhodné pro vytvrzováni čistých pryskyřic ve větším množství. Pryskyřici je potřeba vrstvit.
Vytvrzena kompozice je nažloutlá, čirá a bez dolepu.
Doba želatinace: 15–25 minut při +20 °C (dle připraveného množství)
Vytvrzení: 24 hodin při teplotě +20 °C
Plné vytvrzení: 5 dni při teplotě +20 °C

UPOZORNĚNÍ: Při aplikaci je třeba zajistit takové teplotní podmínky, aby nedošlo k vysrážení vlhkosti na povrchu opravovaného předmětu (rosný bod). Větráním je nutné omezit případný výskyt kyselých plynů a par (např.: CO2), které reagují s tužidlem a znemožňuji dokonale vytvrzeni materiálu. Natužením velkého množství pryskyřice dochází k vyvinu tepla a tím ke zkrácení doby zpracovatelnosti!
! **Výška odlitku** nesmí přesáhnout **20 mm**! Větší odlitky je nutno zhotovovat po vrstvách. Odvod tepla je možno zlepšit přídavkem vhodného plniva, např. suchého křemenného písku.
Nevytvrzenou kompozici lze z povrchu nářadí umýt acetonem. Vytvrzená kompozice lze odstranit pouze mechanicky. Pro zvýšení vytvrzovací teploty nepoužívejte naftové nebo propanbutanové hořáky. Doporučuje se použití infrazářiče.

UŽITNÉ VLASTNOSTI:

Mez pevnosti v tahu:	> 40 MPa
Mez pevnosti v ohybu:	> 90 MPa
Rázová houževnatost:	> 10 kJ/m^2
El. průrazná pevnost (23 °C):	> 10 kV/mm
Měrný vnitřní odpor (23 °C):	> 10^{14} Ohm.cm

Tvrdidlo T 0492

Tvrdidlo pro epoxidové pryskyřice a bezrozpouštědlové epoxidové nátěrové hmoty

POPIS: Roztok aminu v benzylalkoholu.

POUŽITÍ: pro vytvrzování epoxidových pryskyřic, především při výrobě kompozitů, dále pro oblast stavebnictví a pro výrobu lepidel. Vytvrzená kompozice dává velmi dobré mechanické vlastnosti a výbornou **houževnatost**. Zlepšuje smáčení povrchu výztuží i plniv, vyznačuje se **střední dobou zpracovatelnosti** natužené směsi (cca 1-2 hodiny) a **nižším vývinem tepla** při vytvrzování. Vytvrzuje za pokojové teploty (rozmezí od +15 °C do +30 °C). Zachovává **transparentnost a čirost** pryskyřice po vytvrzení povrch kompozice je **bez dolepu.**

TUŽENÍ:

Tabulka tužících poměrů		
Tvrdidlo - pryskyřice	**Hmotnostní poměr**	**Objemový poměr**
T 0492 – CHS-EPOXY 324	16:100	19,5:100
T 0492– CHS-EPOXY 531	27:100	33:100
T 0492– CHS-EPOXY 520	26:100	32:100
T 0492– CHS-EPOXY 521	22:100	26:100
T 0492– CHS-EPOXY 455	22:100	27:100
T 0492– CHS-EPOXY 510	26:100	32:100
T 0492– CHS-EPOXY 474	23:100	26,5:100

ZPRACOVÁNÍ: Odvažte pryskyřici a tvrdidlo v předepsaném poměru a důkladně promíchejte. Při mísení nevmíchejte vzduch do hmoty. Pro větší objemy používejte el. míchadlo s vřetenovým nástavcem s otáčkami do 300 ot./min.

VLASTNOSTI: Vzhled: transparentní kapalina s typickým zápachem po aminech

Hustota: (25 °C): > 0,93 g.cm^{-3}
Viskozita: (25 °C): > 15 mPa.s
Bod vzplanutí: > 150 °C
Vodíkový ekvivalent: 49 g/ekv.